

**Designed Functional Defects in Colloidal
Photonic Crystals: Switching, Biomonitoring
and Modified Photoluminescence**

Dissertation

Zur Erlangung des Grades

“Doktor der Naturwissenschaften”

am Fachbereich Chemie, Pharmazie und Geowissenschaften

der Johannes Gutenberg-Universität in Mainz

von

Friederike Yasmin Fleischhaker

geboren am 03. November 1980 in Wiesbaden

Mainz 2007

Die vorliegende Arbeit wurde in der Zeit von Oktober 2004 bis März 2007 im Fach Makromolekulare Chemie an der Johannes Gutenberg-Universität, Mainz (Oktober 2004 bis Dezember 2004 und April 2006 bis März 2007) und der University of Toronto, Kanada (Januar 2005 bis März 2006) unter der Betreuung von Herrn Prof. Dr. Rudolf Zentel und Herrn Prof. Dr. Geoffrey A. Ozin angefertigt.

Tag der mündlichen Prüfung: 09.05.2007

Abstract

Two complementary bottom-up approaches are presented for the controlled incorporation of "smart" planar defects into self-assembled colloidal photonic crystals (CPCs). The defect layer is based on a functional nanometer scaled thin film that is either prepared by layer-by-layer self-assembly and microcontact transfer printing or by spin-coating and sacrificial CPC infiltration. The developed methods allow for the integration of designed defect thin films from a huge variety of chemically diverse materials and can be employed at low-cost and large-scale. Optical spectra show a sharp transmission state within the photonic stop band, induced by the defect. The position of the defect wavelength is dependent on the optical thickness of the defect layer.

Active tuning of the intragap defect state is performed by preparing defect layers from macromolecules responsive to external stimuli such as light, temperature, redox-cycling and mechanical pressure. The studies are supported by independently performed ellipsometry measurements and theoretical scalar wave approximation calculations.

In addition, CPCs with functional biomolecular planar defects are presented. Through shifts of the defect mode, DNA conformational changes, the enantioselective intercalation of a chiral anti-cancer drug and enzyme activities are optically monitored.

Incorporation of fluorescent dyes and quantum dots into defect CPCs leads to a clear modification of the photoluminescence (PL) spectra by photonic stopband and defect state. Switchable PL modification is detected when employing addressable defect CPCs.

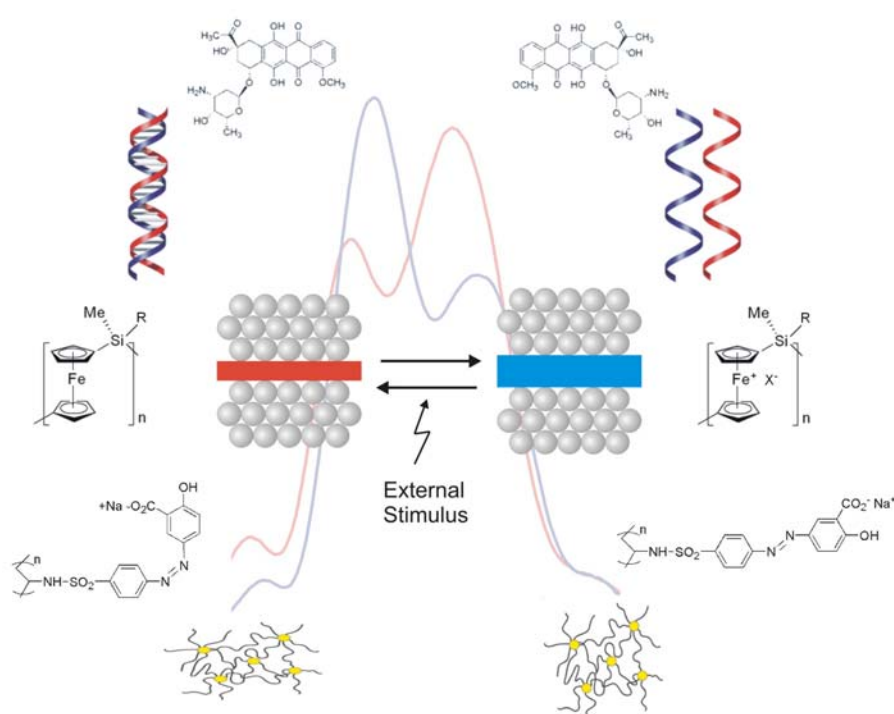


Table of Contents

Abstract	III
Table of Contents	IV
Chapter 1 – Introduction and Background	8
1.1 Preamble	8
1.2 Photonic Crystals	9
1.2.1 Description and Theoretical Background	9
1.2.2 Photonic Crystal Types and Preparation Techniques	12
1.2.2.1 Colloidal Photonic Crystals (Opals)	15
1.2.3 Defects in Photonic Crystals	18
1.2.4 Calculation Methods	19
1.2.4.1 Planar Wave Method (PWM)	19
1.2.4.1.1 Full vector calculation	19
1.2.4.1.2 Scalar wave approximation (SWA)	20
1.3 Thin Films	21
1.3.1 Preparation Methods	21
1.3.1.1 Layer-by-Layer (LbL) self-assembly	22
1.3.2 Characterization Methods	24
1.3.2.1 Ellipsometry	25
1.4 Motivation, Goals and Research Plan	27
1.5 Outline of Thesis	28
1.6 References	29
Chapter 2 – Synthesis and Characterization of Functional Defects in Colloidal Photonic Crystals	34
2.1 Preamble	34
2.2 Introduction	34
2.3 Colloidal Photonic Crystal Synthesis	35
2.3.1 Monodisperse Spheres	35
2.3.1.1 Silica Spheres	35
2.3.1.2 Polymer Spheres	35

2.3.2 Crystallization	37
2.3.3 Mechanical Stabilization	38
2.4 Defect Incorporation	39
2.4.1 Method 1 (LbL self-assembly)	39
2.4.2 Method 2 (Spin-coating)	40
2.5 Scanning Electron Microscopy Characterization	42
2.6 Optical Characterization	44
2.7 SWA-Simulations	49
2.8 Conclusion	51
2.9 References	52
Chapter 3 – Switching of Functional Defects in Colloidal Photonic Crystals	54
3.1 Preamble	54
3.2 UV-Switching	54
3.3 Thermal-Switching	58
3.4 Redox-Switching	59
3.5 Mechanical-Switching	63
3.6 Conclusion	64
3.7 References	65
Chapter 4 – Monitoring Biochemistry with Defect Colloidal Photonic Crystals	66
4.1 Preamble	66
4.2 Introduction	66
4.3 Monitoring DNA Conformational Changes	68
4.4 Chiral Recognition of an Anti-Cancer Drug	70
4.5 Monitoring Enzyme Reactions	73
4.6 Conclusion	77
4.7 References	78
Chapter 5 – Light Emitters in Defect Colloidal Photonic Crystals	80
5.1 Preamble	80
5.2 Introduction	80
5.3 Luminescent Defect Colloidal Photonic Crystals	80
5.3.1 Rhodamine 6G Doped Defect CPC	81

5.3.2 PbS Quantum Dot Doped Defect CPC and Thermal Switching	83
5.4 Colloidal Photonic Crystals with Exclusively Luminescent Defect Layer	86
5.5 Conclusion	88
5.6 References	89
Chapter 6 – Future Work and First Results	91
6.1 Preamble	91
6.2 Multiple Defect Colloidal Photonic Crystals – Photonic "Big Macs"	91
Chapter 7 – Experimental Part	95
7.1 Colloidal Photonic Crystal Synthesis	95
7.1.1 Sphere Synthesis	95
7.1.1.1 Silica Spheres	95
7.1.1.2 Polymer Spheres	96
7.1.2 Crystallization	97
7.1.2.1 Silica Sphere Crystallization	97
7.1.2.2 Polymer Sphere Crystallization	97
7.1.3 Mechanical Stabilization	98
7.1.3.1 Silica CPCs	98
7.1.3.2 PMMA/PGlyMA CPCs	98
7.2 Defect Formation	98
7.2.1 Method 1 (LbL self-assembly/ Microcontact transfer printing)	98
7.2.2 Method 2 (Sacrificial ribose infiltration/ Spin-coating)	99
7.3 PbS Quantum Dot Synthesis	100
7.4 PFS-Polyelectrolyte Synthesis	100
7.5 Instruments	101
7.5.1 Transmission/Reflection Spectroscopy	101
7.5.2 Photoluminescence (PL) Spectroscopy	101
7.5.3 Ellipsometry	102
7.5.4 Scanning Electron Microscopy (SEM)	102
7.5.5 Photography	102
7.5.6 Thermal Gravimetric Analysis (TGA)	102
7.5.7 Heating and Cooling Stage	102
7.5.8 LbL Self-assembly	102

7.5.9 Spin-coating	102
7.5.10 SWA-Simulations	102
7.6 References	103
List of Abbreviations	104
List of Figures	106
List of Tables	111
Acknowledgements	112
Curriculum Vitae	115

Chapter 1

1. Introduction and Background

1.1 Preamble

“There is plenty of room at the bottom” –

with his groundbreaking talk in 1959, the physicist Richard Feynman was creating the roots of a new interdisciplinary field of applied science: Nanotechnology.¹ Nano-, a prefix denoting a factor of 10^{-9} has its origin in the Greek word “nanos”, meaning dwarf. The ability to design, synthesize, characterize and control materials and devices on the scale of one-billionth of a meter has led to amazing achievements in many areas, including materials science, machines, electronics, optics, medicine, biotechnology, energy and aerospace. Portable high capacity laptop-computers, mad-cow disease indicator tests, self-cleaning surfaces or highly breathable and waterproof jackets are but a few examples. The impact of nanoscience is on the one hand the enormous reduction in size but on the other hand also the discovery and understanding of new or changed properties in nanomaterials compared to the macroscopic equivalent (e.g. quantum size effects).

There are two main preparation approaches: The “top-down” engineering of nano-scaled structures into larger entities and the “bottom-up” self-assembly of molecular structures or building blocks into the desired material. Solid-state physics engineering methods have dominated in the latter half of the 20th century but are gradually supplanted by molecular-chemistry and biomimetic methodologies, such as self-assembly. Self-assembly techniques are generally inexpensive, easy to handle and the final structures can approach the complexity in shape and function of that observed in nature. In addition, the chemical diversity, that can be incorporated within the building blocks used in a bottom-up self-assembly approach, largely increases function and utility of the final product.²

In the present work I show how bottom-up chemistry approaches can be used to incorporate “smart” designed defect structures into colloidal photonic crystals. Methods and concepts of Macromolecular Chemistry, Materials Science, Physics and Biochemistry are unconventionally combined and extended leading to new functional materials with various applications.

An introduction into the basics of photonic crystals as well as the preparation and characterization techniques of thin films, which represent the defect building blocks in the photonic crystal composites, is given in this chapter.

1.2 Photonic Crystals

1.2.1 Description and Theoretical Background

Photonic crystals are described as materials with a spatially periodic dielectric constant modulation. Such structures possess the characteristic feature that they can affect the propagation of electromagnetic radiation at wavelengths on a length scale comparable to the lattice constant of the periodic modulation.^{3,4} This attribute has made them promising candidates for a variety of optoelectronic devices intended for telecommunication systems, displays, sensors, resonator cavities or even optical computers.⁵⁻⁸

A basic theoretical concept of photonic crystals was first proposed independently from each other by the researchers S. John and E. Yablonovitch in two simultaneous publications in 1987.^{3,4} Maxwell equations, the fundamentals of electrodynamics, present the necessary tools for a suitable theoretical description of photonic crystals and their influence on electromagnetic waves entering or travelling through the material:⁹

$$\nabla \cdot \mathbf{D} = \rho \qquad \nabla \times \mathbf{E} = -\frac{\partial \mathbf{B}}{\partial t} \qquad (1.1a, 1.1b)$$

Gauss's law for
electricity

Faraday's law of induction

$$\nabla \cdot \mathbf{B} = 0 \qquad \nabla \times \mathbf{H} = \frac{\partial \mathbf{D}}{\partial t} + \mathbf{j} \qquad (1.1c, 1.1d)$$

Gauss's law
for magnetism

Ampère's law

\mathbf{E} (electric field), \mathbf{D} (electric displacement), \mathbf{H} (magnetic field),

\mathbf{B} (magnetic induction), ρ (charge density), \mathbf{j} (current density)

As there are no free charges or currents within the photonic crystal, we can set $\mathbf{j} = \rho = 0$.

Furthermore, some assumptions, that are in good agreement with many dielectric materials, can be made to facilitate the solution of above equations:

- i. The system has a linear response to electromagnetic radiation.
- ii. The materials composing the photonic crystal are isotropic and macroscopic.
- iii. The frequency dependence of the dielectric function is neglected. Its value is assumed to be constant for the frequency range where results are required.
- iv. The magnetic permeability μ is assumed to be unity.

From i and ii we obtain $\mathbf{D} = \varepsilon_0 \varepsilon(\mathbf{r}, \omega) \mathbf{E}$, from iii $\varepsilon(\mathbf{r}, \omega) = \varepsilon(\mathbf{r})$. iv leads to $\mathbf{B} = \mu_0 \mathbf{H}$.

Expanding $\mathbf{H}(\mathbf{r}, t)$ and $\mathbf{E}(\mathbf{r}, t)$ into harmonic wave functions

$$\mathbf{H}(\mathbf{r}, t) = \mathbf{H}(\mathbf{r}) e^{i\omega t} \text{ and}$$

$$\mathbf{E}(\mathbf{r}, t) = \mathbf{E}(\mathbf{r}) e^{i\omega t}$$

and considering $c = 1/(\varepsilon_0 \mu_0)^{1/2}$ for electromagnetic waves, we can drop the time dependency from Maxwell equations and combining equations (1.1b) and (1.1d) leads to the following space dependent eigenvalue equation:

$$\underbrace{\nabla \times \left(\frac{1}{\varepsilon(\mathbf{r})} \nabla \times \mathbf{H}(\mathbf{r}) \right)}_{\text{operator}} = \underbrace{\left(\frac{\omega}{c} \right)^2}_{\text{eigenvalue}} \mathbf{H}(\mathbf{r}) \quad (1.2)$$

Equations (1.1a) und (1.1c) simply lead to $\nabla \cdot \mathbf{B} = \nabla \cdot \mathbf{D} = 0$, which is consistent with transversal waves.

The solutions of the eigenvalue equation are wave vector \mathbf{k} dependent values of ω and are generally plotted in bandstructure diagrams (photonic dispersion relation). Details about calculation methods are provided in section 1.2.4 of this chapter.

Figure 1.1a shows an exemplary bandstructure diagram. The normalized frequencies $\omega a/2\pi c$ with a , the lattice constant, are plotted versus the wave vectors of the reciprocal unit cell, the so-called Brillouin zone. From the photonic dispersion relation $\omega(\mathbf{k})$ we can calculate the frequency dependent density of states (DOS), by forming the integral over all

allowed states for a certain frequency ω (Figure 1.1b).¹⁰ If the photonic DOS is depleted for a certain frequency range (red bar in diagrams of Figure 1.1), we refer to it as a photonic band gap. The propagation of electromagnetic waves of those frequencies is completely suppressed for all directions within the photonic crystal. Incident radiation with band gap frequencies is not allowed to travel through the photonic crystal structure and is reflected at the crystal surface. The bands at the upper and lower edge of the band gap are called air and dielectric bands, respectively, referring to where the power of the electromagnetic mode lies - in the high or in the low dielectric (often air) regions of the material.

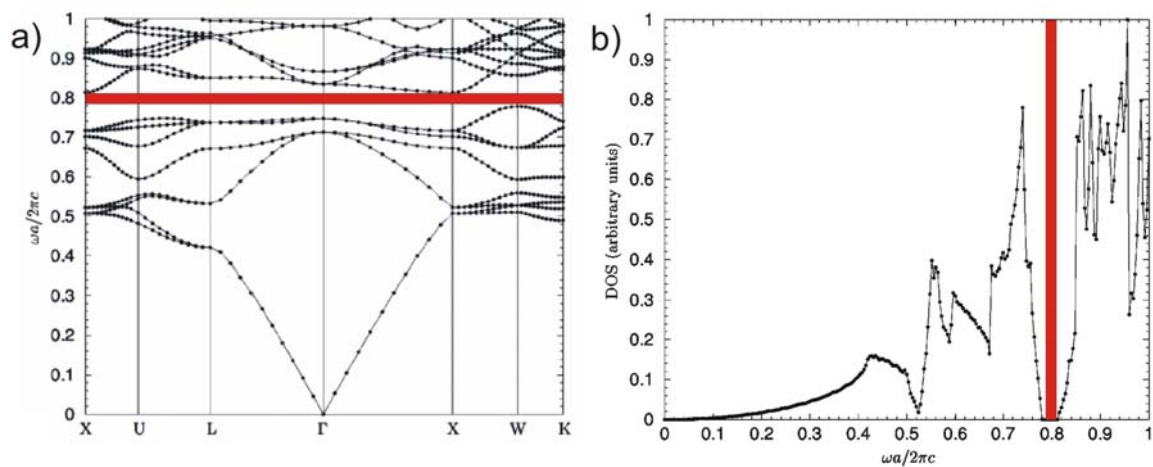


Figure 1.1: Photonic bandstructure diagram (a) and corresponding DOS diagram (b) of a fcc-lattice of air spheres in a dielectric matrix ($\epsilon = 11.9$).¹⁰

Conditions for the opening of photonic band gaps are a three-dimensional periodicity and depending on the photonic crystal geometry also a large dielectric contrast of the high and low refracting components of the periodic material ($\epsilon = n^2$, n : refractive index).

Often, we do not find complete band gaps in photonic crystals but so-called stop bands. In this case, the propagation of the corresponding frequencies is not entirely blocked when entering the crystal but only along specific lattice directions.

The above introduction to the concept of photonic crystals shows many analogies between the electromagnetism in a periodic dielectric and quantum mechanics in a periodic potential. More concretely, the behavior of photons in a photonic crystal can be compared to the behavior of electrons in an electronic semiconductor:⁹

The periodic modulation of the dielectric constant for photons is analogous to the lattice

periodic potential of atoms in a semiconductor for electrons. Eigenvalue equation (1.2) has a striking similarity with the electronic Schrödinger equation ($H\Psi = E\Psi$). The operator in equation (1.2) corresponds to the Hamilton operator, the eigenvalue $(\omega/c)^2$ to the energy eigenvalue E and the magnetic field \mathbf{B} to the wavefunction Ψ . In analogy to electronic bandstructure diagrams and band gaps in semiconductors (between valence and conduction band), we can observe photonic band gaps (between dielectric and air band) in the bandstructure diagrams of photonic crystals. However, in contrast to quantum mechanics, electrodynamics is free from any fundamental length scales. Nothing prevents us for example, from relating results obtained for centimeter scale photonic crystals to the submicrometer scale equivalent.

1.2.2 Photonic Crystal Types and Preparation Techniques

Having a look at different photonic crystal types, we can for example distinguish between the dimensionality of the periodicity. Depending on a one, two or three dimensional periodic lattice, we talk about 1D, 2D or 3D photonic crystals (Figure 1.2).⁹

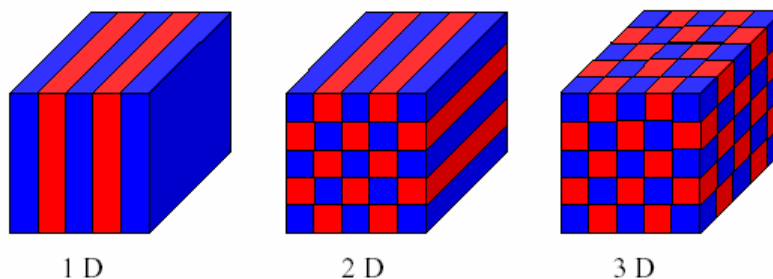


Figure 1.2: Schematic illustration of one, two and three dimensional periodicity in a medium.

Further characteristic parameters that control the optical properties of photonic crystals are symmetry, topology and lattice constant, as well as the refractive index contrast and the effective refractive index (calculated as the square root of the average volume dielectric constant) of the periodic material.¹¹

In one and two dimensional photonic crystals, band structure diagrams and band gaps are limited to the directions of periodic dielectric modulation. Unaffected propagation of electromagnetic waves is possible along those lattice directions showing no periodicity.⁹

One dimensional photonic crystals are known as Bragg mirrors. They consist of periodically stacked layers of different refractive indices (Figure 1.3a).¹²

Two dimensional photonic crystals are often realized in practise by a periodic arrangement of air cylinders in a dielectric or by cylinders consisting of a dielectric material in air (Figure 1.3b).¹³⁻¹⁶

Three dimensional photonic crystal types for example include "woodpile"-architectures (Figure 1.3c),^{17,18} the simplified diamond structure Yablonovite (named after its discoverer E. Yablonovitch)¹⁹⁻²¹ as well as fcc-lattice structures of dielectric spheres in air and their inverted systems. The latter two are nothing else than colloidal photonic crystals. They are the basic building blocks of the work described in this thesis and will be dealt with separately in the next section of this chapter.

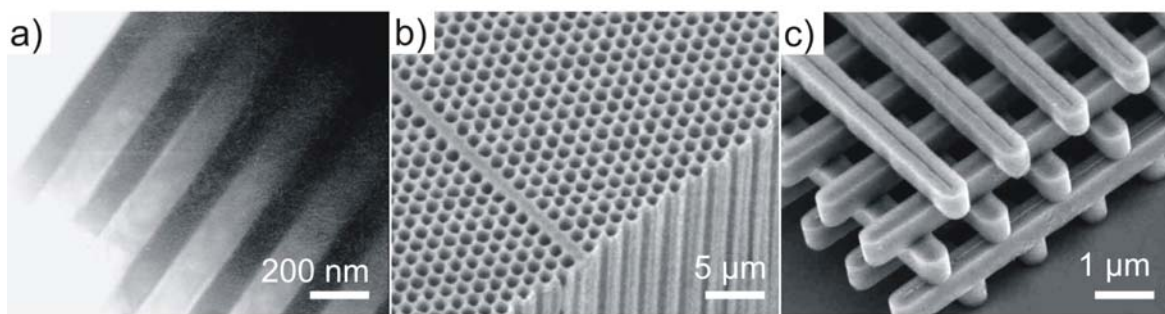


Figure 1.3: Electron microscopy images of different photonic crystal types with 1D, 2D and 3D periodicity. a) GaAs-AlAs Bragg stack.¹² b) Air cylinders in silicon.¹⁶ c) Silicon woodpile structure.¹⁷

In the last years, a large number of preparation methods has been developed for the construction of photonic crystals working in the visible and near infrared (NIR) regimes. The photonic crystal lattice constant is consequently located in the submicrometer and nanometer range. The known top-down fabrication methods include electron-beam lithography, holographic and direct laser writing, as well as microrobotic manipulation.²²⁻²⁵ Alternative bottom-up synthesis methods are especially the self-assembly of nano- or microscale building blocks such as spheres, rods or tubes^{26,27} or the spontaneous organization of block-copolymers or liquid crystals into periodic structures.²⁸⁻³⁰ Interesting are also combinations of both approaches.^{31,32}

Photonic crystals are not only an artificial design and construct but we can also find nanoscaled periodic structures in nature (Figure 1.4).³³ They impress by brilliant colors resulting from light with frequencies reflected by the photonic band gaps and stop bands. Nacre, for instance, is made up of a one dimensional periodic arrangement of organic-inorganic material that can be found in the inside of abalone shells (Figure 1.4a).³⁴⁻³⁷ Sea mouse spines consist of two dimensionally ordered hollow cylinders in α -Chitin

(Figure 1.4b)³⁸ and the secret of many marvellously colored butterfly wings is a highly ordered three dimensional architecture (Figure 1.4c).^{39,40}

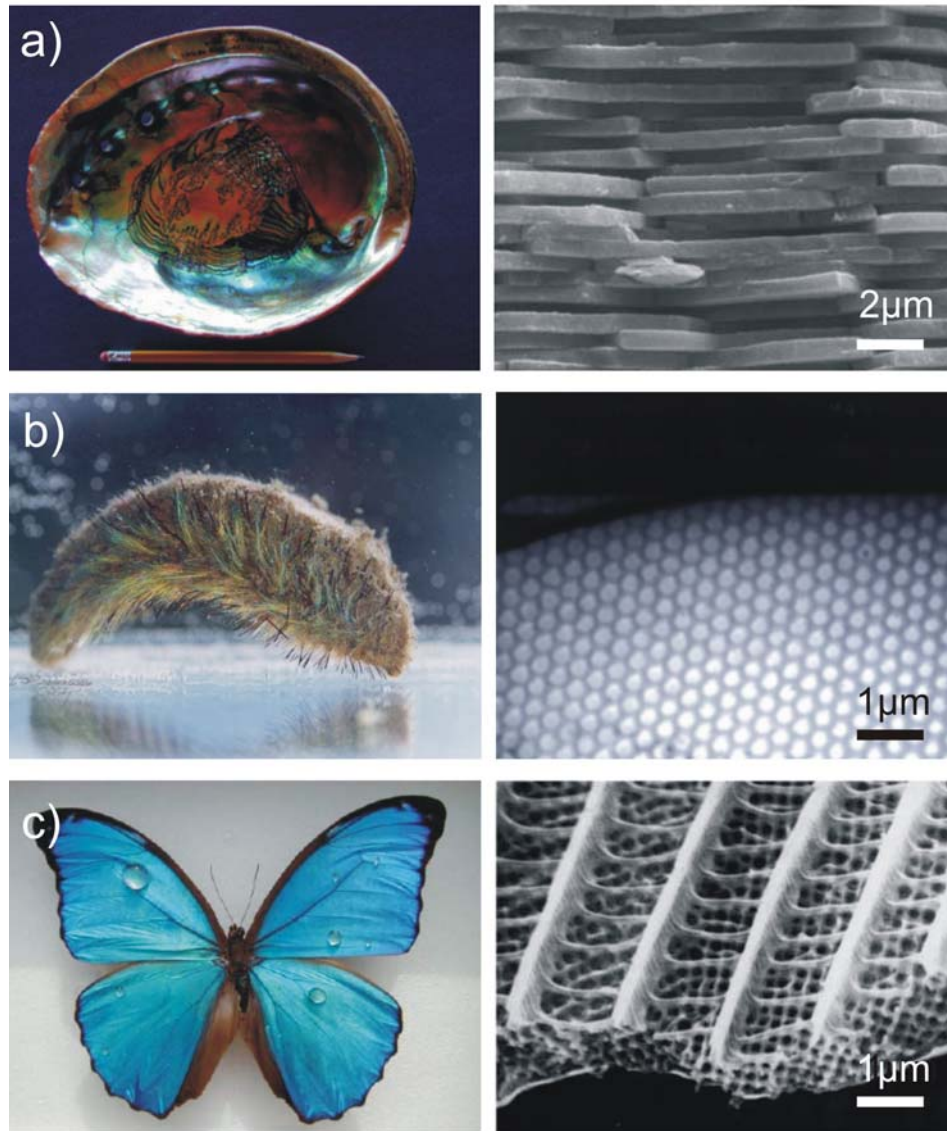


Figure 1.4: 1D, 2D and 3D photonic crystals in nature. Left: a) Abalone shell inside,³⁴ b) sea mouse *Aphrodita*,⁴¹ c) butterfly *Morpho didus* (photographs).⁴² Right: a) Nacre at the inside of an abalone shell,³⁵ b) sea mouse spine³⁸, c) butterfly wing of *Callophrys rubi* (electron microscopy images in cross-section).⁴⁰

Besides the creation of intense reflection colors and their influence on the interaction in flora and fauna (territory control, mate selection), photonic crystals in nature can also protect from damages caused by radiation.³³ Additionally, the periodic arrangement can provide strength and toughness. UV-light protection by a periodic structure is for example achieved in the petals and leaves of certain plants (e.g. the high altitude flower edelweiss).⁴³ Structural color in fruit skin reduces post-maturation discoloration and

ultimately improves dispersal.³³ The abalone shell impressively demonstrates how a periodic layer arrangement of CaCO_3 and proteins can increase the strength of the organic-mineral composite by orders of magnitude compared to the main CaCO_3 building blocks.³⁷

1.2.2.1 Colloidal Photonic Crystals (Opals)

Further examples of naturally occurring photonic crystals are opals. Electron microscopy images of the gem stones show that they consist of fcc-packed monodisperse silica spheres with diameters in the submicrometer and nanometer range (Figure 1.5a).⁴⁴ Consequently they are a subgroup of 3D photonic crystals.¹⁰

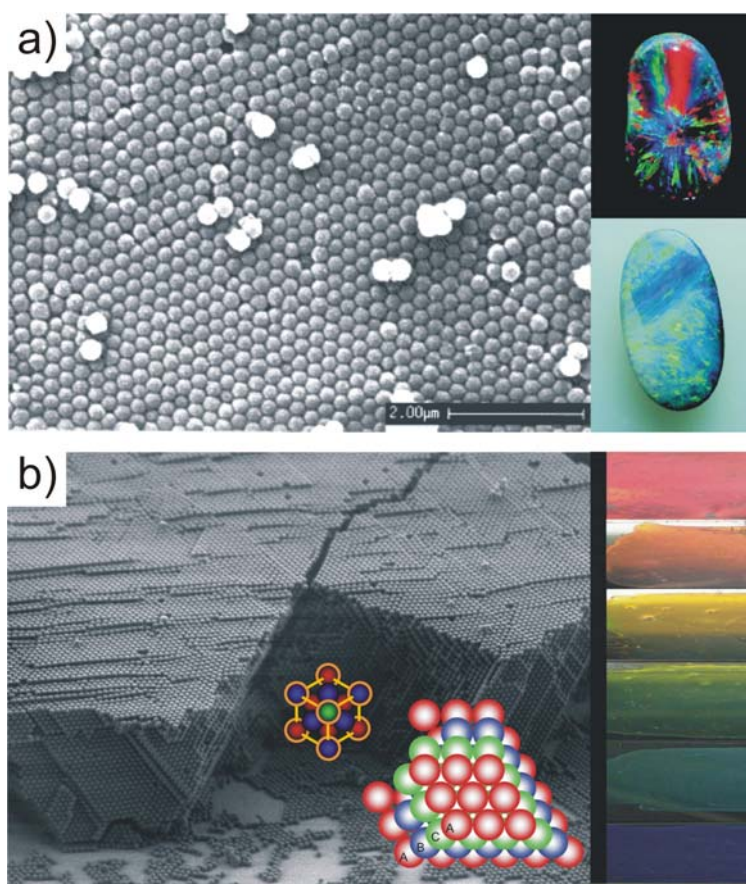


Figure 1.5: a) SEM image (left) and photographs (right) of natural opals.⁴⁵ b) SEM image of a synthetic polymer opal (left).⁴⁶ Photographs of synthetic opals with stop bands at wavelength between 400 nm and 650 nm (right).⁴⁷

Synthetic opals or so-called colloidal photonic crystals (CPCs) are the most important representatives of bottom-up synthesized photonic crystals. CPCs can be self-assembled from monodisperse silica spheres analogously to their natural equivalent, but they can also consist of monodisperse metaloxide or polymer colloids (Figure 1.5b, Figure 1.6a).

Polymer and inorganic colloidal dispersions are usually prepared by sol-gel techniques or by emulsion polymerization.^{26,48-52} They can be produced in large quantities and possess a great significance in daily-life products, such as paints, coatings or cosmetic products. From this point of view, colloidal particles are one of the "oldest" and most frequently used synthetic nanomaterials. Highly monodisperse colloids can be crystallized into fcc-packed CPCs by controlled evaporation of the dispersion agent.

Compared to many other photonic crystal types, opals possess the big advantage that they allow for a facile low-cost and large-area preparation. In addition, CPCs can be used as templates to synthesize their inverted structures. For this purpose a suitable material is infiltrated into the CPC voids and the template is removed afterwards. The preparation of inverted CPCs from various materials including semiconductors, metaloxides and polymers has been demonstrated (Figure 1.6b).⁵³⁻⁵⁵

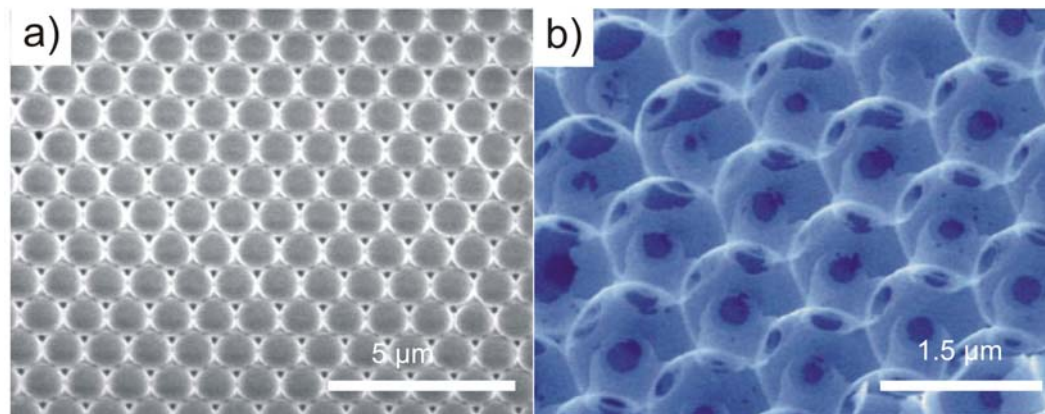


Figure 1.6: a) Surface of a high-quality silica CPC,²⁶ b) cross-section of a silicon inverted CPC (SEM images).⁵³

The optical properties of CPCs cannot only be described with electrodynamics, but also in a simplified form with the help of wave optics. Figure 1.7 schematically shows the optical path of light hitting the surface of a CPC:

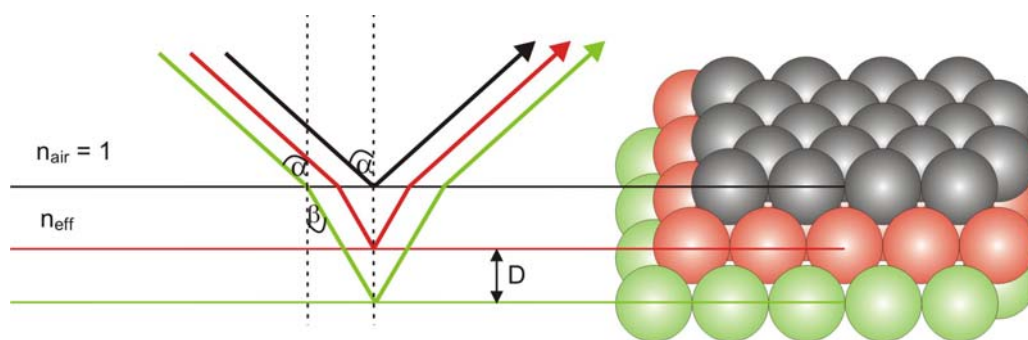


Figure 1.7: Path of light hitting the surface of a CPC.

Incident light is refracted according to Snell's law (1.3) and reflected at the lattice planes of the crystal:

$$\frac{n_{\text{air}}}{n_{\text{eff}}} = \frac{\sin \beta}{\sin \alpha} \quad (1.3)$$

Bragg's law tells us that light waves being reflected at different lattice planes can only interfere constructively, if the phase difference between the waves is an integer multiple of the wavelength. Neglecting the small phase difference of incident waves at the air/ CPC interface leads to:

$$2 D n_{\text{eff}} \cos \beta = i \lambda \quad i = 1, 2, 3, \dots \quad (1.4)$$

If we combine equation (1.3) and (1.4) and use the relation $\sin^2 \beta + \cos^2 \beta = 1$, we obtain the following modified Bragg equation:

$$2 \cdot D \cdot \sqrt{n_{\text{eff}}^2 - \sin^2 \alpha} = i \cdot \lambda \quad i = 1, 2, 3, \dots \quad (1.5)$$

$$D = (2/3)^{1/2} d \quad \text{D: Distance between the lattice planes}$$

$$n_{\text{eff}} = (f_{\text{fcc}} \varepsilon_{\text{sphere}} + (1 - f_{\text{fcc}}) \varepsilon_{\text{air}})^{1/2} = \quad \text{d: sphere diameter}$$

$$= (0,74 \varepsilon_{\text{sphere}} + 0,26 \varepsilon_{\text{air}})^{1/2} \quad f_{\text{fcc}}: \text{fcc filling factor}$$

In terms of bandstructure diagrams, λ corresponds to the first low energy stop band at the position L of the Brillouin zone ($\alpha = 0$, $i = 1$). If we increase α , we move along the Brillouin zone from L to U. For larger angles of α and especially for $i > 1$, equation (1.5) is not suitable anymore. In general, the modified Bragg equation (1.5) is a quick, facile and accurate way to calculate the first stop band in a CPC along the crystal's [111]-direction depending on sphere diameter, material and filling fraction. More complicated systems and a more detailed analysis require bandstructure calculations.

CPCs only open stop bands along several lattice directions, but do not show full band gaps. Experimentally, the positions of the stop bands can be optically detected by transmission or reflection spectroscopy. If the stop band frequencies are located in the visible, our eyes will notice the corresponding reflection color of the material as well (Figure 1.5b).

1.2.3 Defects in Photonic Crystals

Analogously to the doping process of semiconductors, the functionality of photonic crystals can be extended by the controlled introduction of extrinsic defects into the crystal.⁵⁶ Depending on the geometry and the material, the introduced defect can lead to optical defect transmission states located within the photonic band gaps or stop bands (Figure 1.8).⁵⁷ Electromagnetic waves of those frequencies and wave vectors are consequently allowed to propagate within the photonic crystal - they can "tunnel" through the previously forbidden band gap or stop band regions.

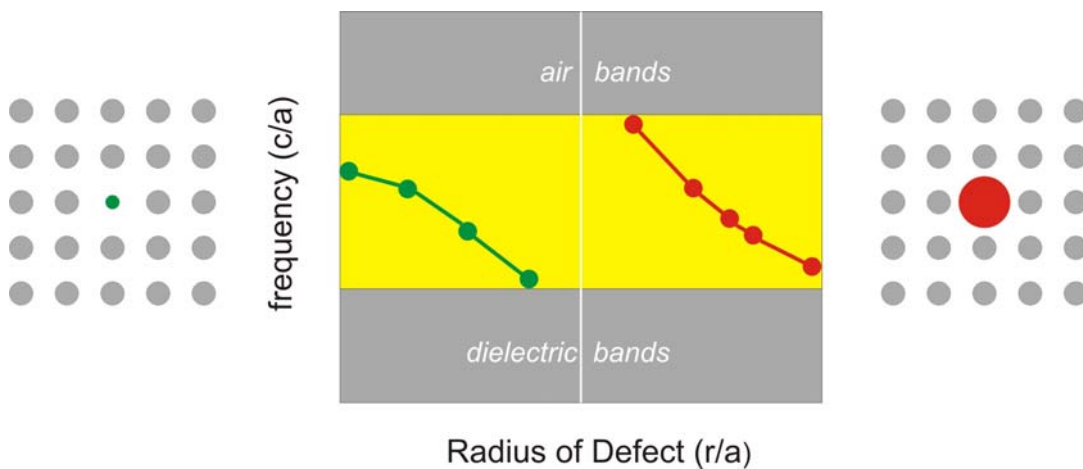


Figure 1.8: Examples of air and dielectric defects and the defect states appearing in the photonic band gap. The defect is caused by a differently sized rod in a two-dimensional photonic crystal consisting of dielectric rods in air.

Similar to 1D, 2D and 3D photonic crystal lattices, we can also distinguish between point, linear and planar defects that can be embedded in each crystal structure. Illustrating examples are shown in Figure 1.9.

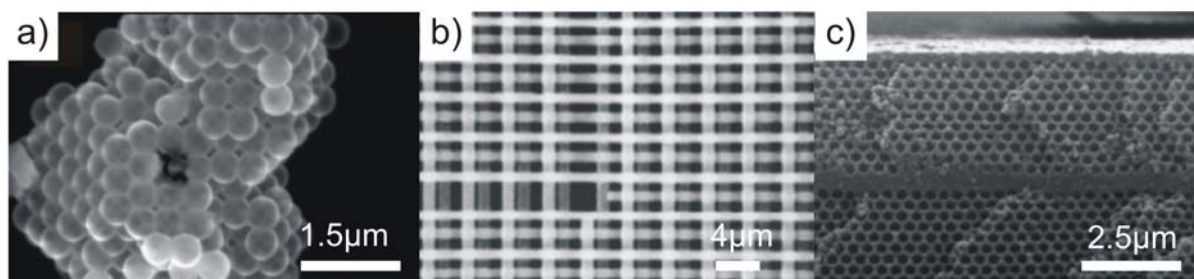


Figure 1.9: a) E-beam lithographically introduced point air defect in a self-assembled CPC.⁵⁸ b) GaAs woodpile structure with line air defect prepared by laser lithography and wafer fusion.¹⁸ c) Inverted silica CPC with planar silica defect prepared in a complete bottom-up approach.⁵⁹ (Electron microscopy images)

If a top-down engineering approach is used in the photonic crystal preparation (see 1.2.2),

defects can be incorporated with the same techniques used in the actual photonic crystal fabrication process (Figure 1.9b).^{16,18,60-62} If the photonic crystal lattice is synthesized by bottom-up self-assembly (see 1.2.2), defect structures can be added subsequently at desired sites e.g. by lithography or micromanipulation (Figure 1.9a).^{31,32,58,63-65} Also, a few procedures have been developed that allow for the preparation of photonic crystal plus defect in a complete bottom-up fashion (Figure 1.9c).⁶⁶⁻⁶⁸

1.2.4 Calculation Methods

Several approaches have been applied to calculate photonic band structures from eigenvalue equation (1.2).⁶⁹ In the following section I will describe the plane wave method (PWM) with full vector calculations as well as the scalar wave approximation (SWA). SWA calculations were used to simulate the optical properties and spectra of the photonic crystal composites developed in this work.

1.2.4.1 Planar Wave Method (PWM)

The PWM is an adaptation of a classical method to calculate bandstructures in semiconductors that takes advantage of the periodicity of the lattice. The Bloch-Floquet theorem is applied to the eigenvalue equation and the periodic part of the eigenfunctions as well as the periodic dielectric constant are expanded into a Fourier series on the reciprocal lattice vectors. Fourier transformation is now a discrete summation and the problem is reduced to diagonalize a matrix.⁶⁹

1.2.4.1.1 Full vector calculation

As it is already indicated by eigenvalue equation (1.2), Maxwell equations have been combined such that the field used for calculations is the magnetic field vector $\mathbf{H}(\mathbf{r})$. The reasons are that $\mathbf{H}(\mathbf{r})$ is a continuous function (in contrast to $\mathbf{E}(\mathbf{r})$) and the operator applied on $\mathbf{H}(\mathbf{r})$ is Hermitian. These facts simplify calculations drastically. The electric field $\mathbf{E}(\mathbf{r})$ can be determined subsequently from solutions for $\mathbf{H}(\mathbf{r})$ via Maxwell equations.

According to the Bloch-Floquet theorem, eigenfunctions of differential equations with periodic coefficients may be expressed as a product of plane waves and lattice periodic functions. Consequently $\mathbf{H}(\mathbf{r})$ can be written as:

$$\mathbf{H}_{\mathbf{k}}(\mathbf{r}) = e^{i\mathbf{k}\mathbf{r}} \mathbf{h}(\mathbf{r}) \mathbf{e}_{\mathbf{k}} \quad (1.6)$$

where $\mathbf{h}(\mathbf{r})$ is a periodic function and \mathbf{e}_k the polarization vector.

Due to the discrete translational symmetry of the lattice, the wave vectors \mathbf{k} may be restricted to lie in the first Brillouin zone of the reciprocal lattice.

In the next step, the dielectric constant function $\epsilon(\mathbf{r})$ as well as the periodic part $\mathbf{h}(\mathbf{r})$ of the eigenfunction (1.6) are expanded into a Fourier series on the reciprocal lattice. We obtain

$$\epsilon(\mathbf{r}) = \sum_{\mathbf{G}} \epsilon_{\mathbf{G}} e^{i\mathbf{G}\cdot\mathbf{r}} \quad (1.7)$$

$$\mathbf{H}_{\mathbf{k}}(\mathbf{r}) = \mathbf{h}(\mathbf{r}) e^{i\mathbf{k}\cdot\mathbf{r}} \mathbf{e}_k = \sum_{\mathbf{G}'} h_{\mathbf{G}'} e^{i\mathbf{G}'\cdot\mathbf{r}} e^{i\mathbf{k}\cdot\mathbf{r}} \mathbf{e}_k \quad (1.8)$$

where \mathbf{G} and \mathbf{G}' are wave vectors of the reciprocal lattice.

Inserting equations (1.7) and (1.8) into eigenvalue equation (1.2), leads to a $2N \times 2N$ matrix problem that must be computed. N is the number of plane waves with two polarization directions each. The accuracy of the calculations increases with N . The unknown Fourier coefficients $h_{\mathbf{G}'}$ can be determined by diagonalizing the matrix. Consequently we obtain solutions for $\mathbf{H}_{\mathbf{k}}(\mathbf{r})$ and we can use the results to calculate the dispersion relation $\omega(\mathbf{k})$ from eigenvalue equation (1.2). Applying PWM to equation (1.2) requires previous independent calculation of the Fourier components of the known dielectric function $\epsilon(\mathbf{r})$.^{9,69}

1.2.4.1.2 Scalar wave approximation (SWA)

As the name implies, the scalar wave approximation neglects the full vector character of the electromagnetic field. Once simplified, this approach is useful to obtain basic but important information without complicated calculations. As an approximation, the utilization of SWA must be done carefully since some of the results can lead to wrong conclusions. For example all the effects caused by polarization are neglected.

This method can be further simplified by using just one plane wave. In the case of CPCs for example, we are examining mostly the [111]-direction. Then, the Fourier expansion of the dielectric constant is truncated as $\epsilon(\mathbf{r}) = \epsilon(\mathbf{G}_0) + \epsilon(\mathbf{G}_{111}) e^{i\mathbf{G}_{111}\cdot\mathbf{r}}$ and all other terms are neglected. Calculations show that $\epsilon(\mathbf{G}_0)$ is nothing but the average dielectric constant and $\epsilon(\mathbf{G}_{111})$ can be easily determined for many systems. The eigenvalue problem is just a 2×2

matrix that can be analytically solved.⁷⁰⁻⁷² Furthermore appropriate boundary conditions may give us information about the transmitted field through a finite (in the propagation direction) crystal.⁷⁰ The method allows us to simulate field functions as well as transmission and reflection spectra of CPCs and inverted CPCs along the [111]-axis in the frequency region of the first stop band. Also, different slabs with different properties (e.g., different sphere diameters, different materials) can be easily combined using textbook transfer-matrix techniques. Here reflection and transmission at the interface and the continuity of the electric field and its derivative between media is additionally taken into account.⁷² Along these lines even complex structures like planar defects inside colloidal photonic crystals can be described. Contrary to full vector calculations, this method fails for high dielectric constants and high energy bands.

1.3 Thin Films

1.3.1 Preparation Methods

"How thick is thin?" - is of course the first question to be asked, since the adjective "thin" certainly is a very relative term. However, the expression "thin films" is commonly used in materials and applied science and generally refers to solid films with a thickness reaching from the molecular or atomic level to the submicrometer range.

In the following part I will give a short overview of different preparation techniques and different thin film "types" especially focused on macromolecular thin films and "layer-by-layer" (LbL) self-assembly presenting a keystone of this work.

With dip-, spin- and spray-coating methods, thin films of various molecules, polymers or particles (e.g. colloids, nanocrystals, aggregates) can be deposited on a substrate from the corresponding solvents or dispersion agents. Other techniques include chemical or physical vapor deposition (CVD, PVD), electrochemical deposition or sputtering. They are mainly used for the preparation of semiconductor, metal, metaloxide and carbon thin films.²

Having a look at the first category of thin films, we can distinguish between different types: Plain uniform films e.g. are mostly prepared by spin-coating. The film thickness can be fine-tuned by parameters like spinning speed and spinning time, solvent or dispersion agent and concentration. It is a versatile technique that allows for thin film preparation from a myriad of materials with thickness control of a few tens of a

nanometer. Other thin film types of this category for example are more restricted to specific molecules or particles but allow for thickness control on the molecular level.

Prominent representatives are self-assembled monolayers (SAMs), Langmuir-Blodgett (LB) films or LbL self-assembled multilayers. SAMs were mainly pioneered by Nuzzo and Whitesides *et al.*⁷³⁻⁷⁵ The classic examples consist of long-chain alkanethiolates monolayers chemisorbed on a gold substrate that can be prepared in a simple dip-coating and rinsing fashion. Some variations in the choice of substrate and molecules are possible. Langmuir and Blodgett invented a technique that allows for the build-up of stacked monolayers of amphiphilic molecules in a "head-tail"/ "tail-head" fashion. A monolayer of amphiphiles is carefully spread and close-packed on the water surface in a special trough and subsequently transferred onto a substrate by immersion and emersion.⁷⁶ The LbL self-assembly method mainly developed by Decher *et al.* is based on the alternate deposition of oppositely charged polyelectrolyte layers to an electrostatically bound superlattice.⁷⁷ It is a facile and powerful approach to the formation of thin multilayer films with controlled architecture and will be discussed in more detail in the next paragraph.

1.3.1.1 Layer-by-layer (LbL) self-assembly

Iler discovered in 1966 that certain surfaces modified with cationic surfactants bind monolayers of negatively charged colloidal silica or latex particles.⁷⁸ The anionic layers can then bind cationic colloids like boehmite or gelatin, a cationic colloidal biopolymer.⁷⁹ Alternate immersions in suspensions of opposite charge gave multilayer films one layer at a time.

Decher in 1991, extended the concept to LbL growth of soluble organic polyelectrolytes.^{77,80-82} The procedure is schematically illustrated in Figure 1.10. A charged substrate (e.g. an aminoalkoxysilane functionalized glass slide) is alternately immersed in polyelectrolyte solutions of opposite charge with rinse steps following each immersion. During each layer deposition step, the polyelectrolytes from solution are electrostatically attracted by the oppositely charged molecules constituting the last layer of the film that have already been deposited on the substrate. The polyelectrolyte deposition leads to charge overcompensation at the interface, which in turn causes electrostatic repulsion and limits the adsorption to only one additional monolayer. This allows for precise thickness control of the final multilayer stack by the number of deposited layers. However, it should be mentioned that Figure 1.10b shows a very simplified molecular picture of a polyelectrolyte multilayer. Investigations clearly demonstrate a certain degree

of interpenetration of the single layers.⁷⁷ Some polyelectrolytes are even shown to undergo a diffusion process "in" and "out" the entire film during each bilayer deposition step.⁸³ The deposition characteristics as well as the thickness per layer (typically between 1 and 10 nm) can be further modified by, for instance, varying the pH, salt concentration, or polyelectrolyte charge density.⁸⁴⁻⁸⁷

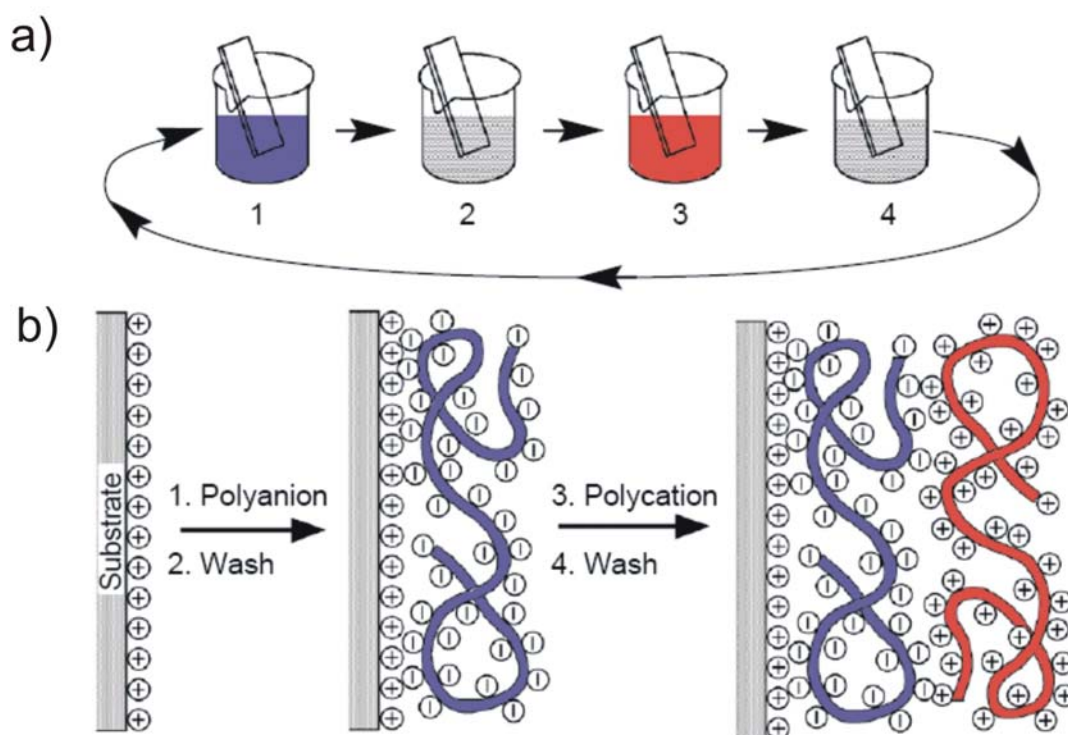


Figure 1.10: a) Schematic illustration of the LbL self-assembly process. Steps 1 and 3 represent the adsorption of polyanion and polycation, respectively, and steps 2 and 4 are rinsing steps. The four steps are the basic buildup sequence for the simplest film architecture $(A/B)_n$. The construction of more complex film architectures requires only additional polyelectrolyte and rinsing solutions and a different deposition sequence. b) Simplified molecular picture of the first two adsorption steps when starting from a positively charged substrate.⁷⁷

Although the LbL approach is based on electrostatic attraction between positively and negatively charged species, the primary thermodynamic driving force is of entropical and not enthalpical nature.⁸⁸ The complexation of the polyions by a charged surface liberates undissociated low molar mass counterions, thus increasing the entropy of the system. An additional entropy gain may derive from the liberation of solvent molecules from the solvation shell of the polymer-bound ionic groups.

The technique does not require complicated equipment but can be automated and generalized to any species bearing multiple charges (to guarantee adhesion and interfacial charge overcompensation). Ionomers,⁸⁹ charged proteins,⁹⁰ clay platelets,⁹¹ polynucleic

acids,⁹² virus particles⁹³ or colloids,^{94,95} to name a few, can be employed to build up multicomponent films in an LbL fashion with nanometer scale precision. Also, the original dip-coating procedure can be alternatively replaced by LbL spray- or spin-coating techniques reported in literature.⁹⁶⁻⁹⁸

An additional benefit of the LbL method is that there is in principle no restriction with respect to substrate, size and topology.⁷⁷ LbL self-assembly has been performed on the highly curved surface of colloids^{99,100} and Hammond *et al.* for example have demonstrated LbL growth on a poly(dimethylsiloxane) (PDMS) stamp that allows for subsequent microcontact transfer printing and patterning of the multilayer.¹⁰¹

1.3.2 Characterization Methods

Thin film characterization methods are as multiple as the previously discussed preparation techniques. We have to distinguish between the determination of thickness and refractive index, internal structure or composition of the film. Here, I will focus on the parameters thickness and refractive index that are the crucial input factors with respect to the optical properties of "thin film"-defect CPCs investigated in this work.

Electron microscopy such as SEM and TEM as well as mechanical raster-scanning of the deposited film by atomic force microscopy (AFM) are possible tools for thickness determination by direct "visualization". Absorption spectroscopy is an indirect approach for thickness measurements if the extinction coefficient of the absorbing group is known. Optical profilometry or reflectometry are based on the constructive interference of light at the film interface. They provide information about film thickness or refractive index if one of the parameters is available. Surface plasmon resonance (SPR) investigations require film deposition on a suitable substrate like gold and allow us to obtain either thickness or refractive index of the investigated sample. The measurements are based on the conversion of incident photons into surface plasmons at a certain momentum and energy that depend on the optical properties of the adsorbed film. It is a highly sensitive technique - still, knowledge of one of the two quantities is necessary to calculate the second one. Spectroscopic ellipsometry offers the possibility to determine both unknown thin film parameters, thickness and refractive index, in parallel. It was employed as major characterization method of the various polymer thin films used as active CPC defect layers in this work. Details will be explained in the following section.

1.3.2.1 Ellipsometry

Ellipsometry measures the change in polarization of light upon non-normal reflection on the surface of a sample to be studied (Figure 1.11).

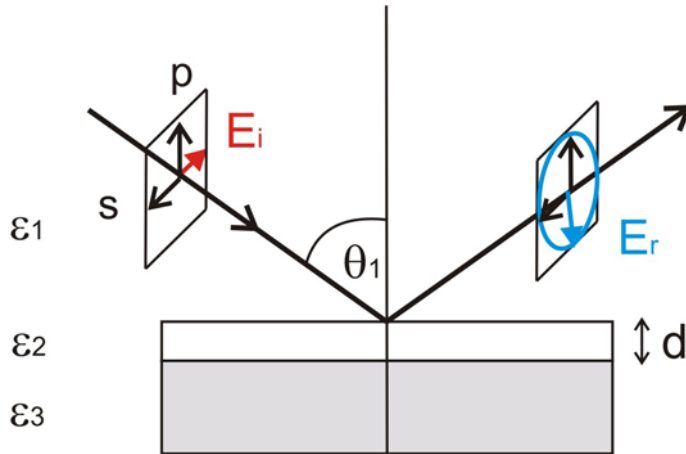


Figure 1.11: Ellipsometry schematically illustrated. The change in polarization of light upon reflection on the surface of a sample on a substrate is measured.

The incident light (E_i) is linearly polarized with field components in the directions parallel (p) and perpendicular (s) to the plane of incidence (the labelling s originates from the German word "senkrecht"). Upon reflection the s - and p -polarized waves undergo a phase shift as well as a change in amplitude. The reflected light (E_r) therefore is elliptically polarized giving the technique its name. The experimental data are usually expressed as two parameters Ψ and Δ , which are related to the Fresnel reflection coefficients by:

$$\frac{R^p}{R^s} = \tan \Psi e^{i\Delta} \quad (1.9)$$

R^p and R^s are the ratios of incident to reflected amplitudes of s - and p -polarized waves, respectively. Δ defines the shift in phase difference between s - and p -waves before and after reflection. Ψ is defined in such a manner that $\tan \Psi = |R^p|/|R^s|$.

In the case of a spectroscopic ellipsometer, Ψ and Δ are measured over a range of wavelengths in the visible or NIR spectrum. The resulting experimental wavelength dependent data of Ψ and Δ have to be modelled with the help of Fresnel equations. For a single film on a substrate as sketched in Figure 1.11 we have to take into account additional refraction and reflection at the interface. The total reflection coefficients R^p and R^s are calculated as:

$$R^p = \frac{r_{12}^p + r_{23}^p \exp(-i2\beta)}{1 + r_{12}^p r_{23}^p \exp(-i2\beta)} \quad R^s = \frac{r_{12}^s + r_{23}^s \exp(-i2\beta)}{1 + r_{12}^s r_{23}^s \exp(-i2\beta)} \quad (1.10)$$

where

$$r_{ij}^p = \frac{\tilde{n}_j \cos \phi_i - \tilde{n}_i \cos \phi_j}{\tilde{n}_j \cos \phi_i + \tilde{n}_i \cos \phi_j} \quad \beta = 2\pi \left(\frac{d}{\lambda} \right) \tilde{n}_2 \cos \phi_2 \quad (1.11)$$

$$\varepsilon_i = \tilde{n}_i^2 = (n_i + ik)^2$$

$$r_{ij}^s = \frac{\tilde{n}_i \cos \phi_i - \tilde{n}_j \cos \phi_j}{\tilde{n}_i \cos \phi_i + \tilde{n}_j \cos \phi_j} \quad \tilde{n}_i \sin \phi_i = \tilde{n}_j \sin \phi_j$$

r_{ij} : Fresnel reflection coefficient

ε_i : dielectric constant

\tilde{n}_i : complex index of refraction

n_i : index of refraction

k : extinction coefficient

ϕ_i : angle of incidence

d : film thickness

Information about thickness and refractive index dispersion of the analyzed sample can be obtained from carefully performed theoretical fits of the experimental data. A variable angle spectroscopic ellipsometer allows in addition to operate at two or more angles of incidence. Thus, the accuracy of the fits is increased.

If the sample is non-absorbant, the refractive index dispersion is usually described by the Cauchy-model:

$$n(\lambda) = a + \frac{b}{\lambda^2} + \frac{c}{\lambda^4} \quad a, b, c: \text{Cauchy parameters} \quad (1.12)$$

If the sample is absorbant in the wavelengths range the measurement is performed at, additional oscillators modelling excitonic resonances can be included in the expression of the refractive index. The Lorentz-model, for example, is based on this concept.¹¹²

1.4 Motivation, Goals and Research Plan

As discussed in section 1.2.3, the functionality of photonic crystals can only be truly harnessed by the controlled introduction of extrinsic defects that can lead to defined optical defect states within the photonic band gaps or stop bands. This behavior is analogous to the doping process of electronic semiconductors. Several methods have been developed that allow for the incorporation of passive "rigid" defect structures into top-down and bottom-up synthesized three-dimensional photonic crystal types.

The primary goal of this work is the preparation of CPCs with embedded functional planar defects that can be actively addressed by external stimuli.

The bottom-up construction of such "smart" defect CPCs possessing tunable optical intragap transmission states requires the following challenging preparation steps: First, monodisperse spheres have to be synthesized and self-assembled to a high-quality bottom-CPC. A smooth surface structure, thickness control and mechanical stabilization of the bottom-CPC will be necessary to allow further processing. These steps will be followed by a homogeneous defect layer synthesis of controlled thickness and self-assembly of a high-quality top-CPC. Thin film preparation methods such as LbL self-assembly and spin-coating (see 1.3.1) are promising techniques with respect to the incorporation of a huge variety of materials into CPC defect layers. However, protection of the CPC-voids from defect layer material infiltration will be crucial and could be realized by transfer printing or sacrificial CPC fillings, for example.

Active defect state tuning is intended to be investigated by incorporating functional macromolecules responsive to light, redox-cycling or mechanical pressure into CPC planar defects. I consider azo-benzene based polymers, polyferrocenylsilanes or elastomers as interesting candidates. Independently performed ellipsometry measurements and theoretical SWA-calculations are planned to be used as additional quantitative control-experiments.

In a next step, one can investigate whether functional defect CPCs can also be employed for monitoring aspects. CPCs with biomolecular planar defect, for example, would present a completely novel type of optical bio-functional material. We can examine, if it is possible to monitor conformational changes or different types of chemical or biochemical reactions taking place in the defect layer through shifts of the defect mode.

An additional research goal would be the incorporation of light emitters into defect CPCs. Here, the influence of photonic stop band and tunable defect state on the photoluminescence properties of the embedded light emitters is of interest to be studied.

1.5 Outline of Thesis

The thesis is written in seven chapters. In chapter 2, I present two complete bottom-up preparation methods that allow for the integration of designed functional planar defects in CPCs. In chapter 3, I demonstrate active tuning of the defect wavelength by a number of external stimuli. Chapter 4 turns the tables and shows that defect CPCs can also be employed to optically monitor various aspects of chemistry and biochemistry taking place in the functional defect layer through shifts of the defect mode. Chapter 5 reports on the integration of fluorophores into defect CPCs. The influence of photonic stop-band and tunable defect state on the photoluminescence is investigated. Ideas and concepts about future work as well as experimental details are included in chapters 6 and 7.

1.6 References

- (1) <http://www.zyvex.com/nanotech/feynman.html>.
- (2) Ozin, G. A.; Arsenault, A. C. *Nanochemistry: A Chemical Approach to Nanomaterials*, RSC Publishing, Cambridge, 2005.
- (3) Yablonovitch, E. *Phys. Rev. Lett.* **1987**, *58*, 2059.
- (4) John, S. *Phys. Rev. Lett.* **1987**, *58*, 2486.
- (5) Joannopoulos, J. D.; Villeneuve, P. R.; Fan, S. H. *Nature* **1997**, *387*, 830.
- (6) Asher, S. A.; Holtz, J.; Weissman, J.; Pan, G. *MRS Bull.* **1998**, *23*, 44.
- (7) Lopez, C. *Adv. Mater.* **2003**, *15*, 1679.
- (8) Arsenault, A.; Fournier-Bidoz, S.; Hatton, B.; Miguez, H.; Tetreault, N.; Vekris, E.; Wong, S.; Yang, S. M.; Kitaev, V.; Ozin, G. A. *J. Mater. Chem.* **2004**, *14*, 781.
- (9) Joannopoulos, J. D. *Photonic Crystals: Molding the Flow of Light*, Princeton University Press, Princeton, NJ, 1995.
- (10) Busch, K.; John, S. *Phys. Rev. E* **1998**, *58*, 3896.
- (11) Garcia Santamaria, F., Thesis, 2003.
- (12) Thomas, P. J. S.; Hosea, T. J. C.; Lancefield, D.; Meidia, H. *Semicond. Sci. Technol.* **2001**, 107.
- (13) Birner, A.; Busch, K.; Müller, F. *Phys. Blätter* **1999**, *55*, 27.
- (14) Lin, S. Y.; Chow, E.; Hietala, V.; Villeneuve, P. R.; Joannopoulos, J. D. *Science* **1998**, *282*, 274.
- (15) Kramper, P.; Birner, A.; Agio, M.; Soukoulis, C. M.; Müller, F.; Gösele, U.; Mlynek, J.; Sandoghar, V. *Phys. Rev. B* **2001**, *64*, 23102.
- (16) Birner, A.; Wehrspohn, R. B.; Gösele, U.; Busch, K. *Adv. Mater.* **2001**, *13*, 377.
- (17) Lin, S. Y.; Fleming, J. G.; Hetherington, D. L.; Smith, B. K.; Biswas, R.; Ho, K. M.; Sigalas, M. M.; Zubrzycki, W.; Kurtz, S. R.; Bur. J. *Nature* **1998**, *394*, 251.
- (18) Noda, S.; Tomaka, K.; Yamamoto, N.; Chutinan, A. *Science* **2000**, *289*, 604.
- (19) Yablonovitch, E. *J. Mod. Optics* **1994**, *41*, 173.
- (20) Feiertag, G.; Ehrfeld, W.; Freimuth, H.; Kollé, H.; Lehr, H.; Schmidt, M.; Sigalas, M.M.; Soukoulis, C.M.; Kuhl, J.; Koenig, W. *Appl. Phys. Lett* **1997**, *71*, 1441.
- (21) Miklyaev, Y.V.; Meisel, D.C.; Blanco, A.; von Freymann, G.; Busch, K.; Koch, W.; Enkrich, C.; Deubel, M.; Wegener, M. *Appl. Phys. Lett* **2003**, *82*, 1284.
- (22) Krauss, T. F.; DeLaRue, R. M.; Brand, S. *Nature* **1996**, *382*, 699.

-
- (23) Deubel, M.; v. Freymann, G.; Wegener, M.; Pereira, S.; Busch, K.; Soukoulis, C. *M. Nat. Mater.* **2004**, *3*, 444.
- (24) Campell, M.; Sharp, D. N.; Harrison, M. T.; Denning, R. G.; Turberfield, A. J. *Nature* **2000**, *404*, 53.
- (25) Aoki, K.; Myazaki, H.; Inoshita, T.; Baba, K.; Sakoda, N.; Shinya, N.; Aoyagi, Y. *Nat. Mater.* **2003**, *2*, 117.
- (26) Wong, S.; Kitaev, V.; Ozin, G. A. *J. Am. Chem. Soc.* **2003**, *125*, 15589.
- (27) Kempa, K.; Kimball, B.; Rybczynski, J.; Huang, Z. P.; Wu, P. F.; Steevens, D.; Sennett, M.; Giersig, M.; Rao, D. V. G. L. N.; Carnahan, D. L.; Wang, D. Z.; Lao, J. Y.; Li, W. Z.; Ren, Z. F. *Nano Lett.* **2003**, *3*, 13.
- (28) Fink, Y.; Urbas, A.; Bawendi, M.; Joannopoulos, J.; Thomas, E. *J. Lightwave Technol.* **1999**, *17*, 1963.
- (29) Chen, X. L.; Jenekhe, S. A. *Science* **1999**, *283*, 372.
- (30) Müller, M.; Zentel, R. *Macromol. Chem. Phys.* **2000**, *201*, 2055.
- (31) Tetreault, N.; Miguez, H.; Yang, S. M.; Kitaev, V.; Ozin, G. A. *Adv. Mater.* **2003**, *15*, 1167.
- (32) Ferrand, P.; Egen, M.; Zentel, R.; Seekamp, J.; Romanov, S. G.; Sotomayor Torres, C. M. *Appl. Phys. Lett.* **2003**, *83*, 5289.
- (33) Vukusic, P.; Sambles, J. R. *Nature* **2003**, *424*, 14.
- (34) <http://www.biosbcc.net/ocean/marinesci/06future/abintro.htm>.
- (35) <http://www.biophysik.uni-bremen.de/fritz/images/perlmutt.jpg>.
- (36) <http://www.solids.bnl.gov/~dimasi/bones/abalone/>.
- (37) Smith, B. L.; Schäffer, T. E.; Viani, M.; Thompson, J. B.; Frederick, N. A.; Kindt, J.; Belcher, A.; Stucky, G. D.; Morse, D. E.; Hansma, P. K. *Nature* **1999**, *399*, 761.
- (38) Parker, A. R.; McPhedran, R. C.; McKenzie, D. R.; Botten, L. C.; Nicorovici, N. *P. Nature* **2001**, *409*, 36.
- (39) Srinivasarao, M. *Chem. Rev.* **1999**, *99*, 1935.
- (40) http://217.33.105.254/Previous_Projects/Exploiting_the_electromagnetic_spectrum/Opticks/RoySamblesR.pdf.
- (41) <http://www.physics.usyd.edu.au/theory/seamouse/TheAnimal/aphrodit.acu.jpg>.
- (42) Gu, Z., Morpho-Schmetterling (Kanagawa Academy of Science and Technology), **2003**.

- (43) Kertesz, K.; Balint, Z.; Vertesy, Z.; Mark, G. I.; Lousse, V.; Vigneron, J. P.; Biro, L. P. *Curr. App. Phys.* **2006**, *6*, 252.
- (44) Sanders, V. *Nature* **1964**, *204*, 1151.
- (45) <http://minerals.gps.caltech.edu/IMAGES/Opal2.gif>.
- (46) Egen, M., Thesis, 2003.
- (47) Fleischhaker, F.; Zentel, R. *Chem. Mater.* **2005**, *17*, 1346.
- (48) W. Stöber, A. Fink, E. J. Bohn *J. Colloid Interface Sci.* **1968**, *26*, 62.
- (49) P. Jiang, J. F. Bertone, K. S. Hwang, V. L. Colvin *Chem. Mater.* **1999**, *11*, 2132.
- (50) Xia, Y.; Gates, B.; Yin, Y.; Lu, L. *Adv. Mater.* **2000**, *12*, 693.
- (51) Miguez, H.; Meseguer, F.; Lopez, C.; Blanco, A.; Moya, J. S.; Requene, J.; Mifsud, A.; Fornes, V. *Adv. Mater.* **1998**, *10*, 480.
- (52) Egen, M.; Zentel, R. *Macromol. Chem. Phys.* **2004**, *205*, 1479.
- (53) Blanco, A.; Chomski, E.; Grabtchak, S.; Ibisate, M.; John, S.; Leonard, S. W.; Lopez, C.; Meseguer, F.; Miguez, H.; Mondia, J. P.; Ozin, G. A.; Toader, O.; van Driel, H. M. *Nature*, **2000**, *405*, 437.
- (54) Wijnhoven, J. E. G. J.; Vos, W. C. *Science* **1998**, *281*, 802.
- (55) Arsenault, A. C.; Clark, T. J.; v. Freymann, G.; Cademartiri, L.; Sapienza, R.; Bertolotti, J.; Vekris, E.; Wong, S.; Kitaev, V.; Manners, I.; Wang, R. Z.; John, S.; Wiersma, D.; Ozin, G. A. *Nat. Mater.* **2006**, *5*, 179.
- (56) Yablonovitch, E.; Gmitter, T. J.; Meade, R. D.; Rappe, A. M.; Brommer, K. D.; Joannopoulos, J. D. *Phys. Rev. Lett.* **1991**, *67*, 3380.
- (57) Johnson, G. J. *Periodic surprises in electromagnetism*, MIT lecture series, lecture 2 (2004).
- (58) Xie, R.; Sekiguchi, T.; Li, D.; Yang, D.; Jiang, M. *J. Phys. Chem. B Lett.* **2006**, *110*, 1107.
- (59) Tetreault, N.; Mihi, A.; Miguez, H.; Rodriguez, I.; Ozin, G. A.; Meseguer, F.; Kitaev, V. *Adv. Mater.* **2004**, *16*, 346.
- (60) Mertens, G.; Wehrspohn, R. B.; Kitzerow, H. S.; Matthias, S.; Jamois, C.; Gösele, U. *Appl. Phys. Lett.* **2005**, *87*, 1108.
- (61) Garcia-Santamaria, F.; Lopez, C.; Meseguer, F.; Lopez-Tejeira, F.; Sanchez-Dehesa, J.; Miyazaki, H. T. *Appl. Phys. Lett.* **2001**, *79*, 2309.
- (62) Scrimgeour, J.; Sharp, D., N.; Blanford, C. F.; Roche, O. M.; Denning, R. G.; Turberfield, A. J. *Adv. Mater.* **2006**, *12*, 1557.

- (63) Vekris, E.; Kitaev, V.; v. Freymann, G.; Perovic, D. D.; Aitchison, J. S.; Ozin, G. A, *Adv. Mater.* **2005**, *17*, 1269.
- (64) Lee, W. M.; Pruzinsky, S. A.; Braun, P. V. *Adv. Mater.* **2002**, *14*, 271.
- (65) Jun, Y. H.; Leatherdale, C. A.; Norris, D. J. *Adv. Mater.* **2005**, *17*, 1908.
- (66) Egen, M.; Voss, R.; Griesebock, B.; Zentel, R. *Chem. Mater.* **2003**, *15*, 3786.
- (67) Tetreault, N.; Mihi, A.; Miguez, H.; Rodriguez, I.; Ozin, G. A.; Meseguer, F.; Kitaev, V. *Adv. Mater.* **2004**, *16*, 346.
- (68) Pozas, R.; Mihi, A.; Ocana, M.; Miguez, H. *Adv. Mater.* **2006**, *18*, 1183.
- (69) Busch, K. *C. R. Physique* **2002**, *3*, 53.
- (70) Shung, K. W. K.; Tsai, Y. C. *Phys. Rev. B* **1993**, *48*, 11265.
- (71) Mittleman, D., M.; Bertone, J. F.; Jiang, P.; Hwang, K., S.; Colvin, V. L. *J. Chem. Phys.* **1999**, *111*, 345.
- (72) Mihi, A.; Míguez, H. *J. Phys. Chem. B.* **2005**, *109*, 15968.
- (73) Bain, C. D.; Troughton, E. B.; Tao, Y. T.; Evall, J.; Whitesides, G. M.; Nuzzo, R. *G. J. Am. Chem. Soc.* **1989**, *111*, 321.
- (74) Bishop, A. R.; Nuzzo, R. G. *Curr. Opin. Colloid Interface Sci.* **1996**, *1*, 127.
- (75) Xia, Y. N.; Whitesides, G. M. *Angew. Chem. Int. Ed.* **1998**, *37*, 551.
- (76) Roberts, G. G. *Contemp. Phys.* **1984**, *25*, 109.
- (77) Decher, G. *Science* **1997**, *277*, 1232.
- (78) Iler, R. K. *J. Colloid Interf. Sci.* **1966**, *21*, 569.
- (79) Harrington, W. F., Hippel, P. H. **1961**, *16*, 1.
- (80) Decher, G.; Hong, J. D. *Makromol. Chem. Macromol. Symp.* **1991**, *21*, 569.
- (81) Decher, G.; Hong, J. D. *Ber. Bunsen-Ges.* **1991**, *95*, 1430.
- (82) Decher, G.; Hong, J. D.; Schmitt, J. **1992**, *210*, 831.
- (83) Porcel, C.; Lavalle, P.; Ball, V.; Decher, G.; Senger, B.; Voegel, J.-C.; Schaaf, P. *Langmuir* **2006**, *22*, 4376.
- (84) Yoo, D.; Shiratori, S. S.; Rubner, M. F. *Macromolecules* **1998**, *31*, 4309.
- (85) Shiratori, S. S.; Rubner, M. F. *Macromolecules* **2000**, *33*, 4213.
- (86) Clark, S. L.; Montague, M. F.; Hammond, P. T. *Macromolecules* **1997**, *30*, 7237.
- (87) Plunkett, M. A.; Claesson, P. M.; Ernstsson, M.; Rutland, M. W. *Langmuir* **2003**, *19*, 4673.
- (88) Bertrand, P.; Jonas, A.; Laschewsky, R.; Legras, R. *Macromol. Rapid Commun.* **2000**, *21*, 319.
- (89) Mruk, R.; Prehl, S.; Zentel, R. *Macromol. Rapid Commun.* **2003**, *24*, 1014.

-
- (90) Hong, J. D.; Lowack, K.; Schmitt, J.; Decher, G. *Prog. Colloid. Polym. Sci.* **1993**, 93, 98.
- (91) Kotov, N. A.; Haraszti, T.; Turi, L.; Zavala, G.; Geer, R. E.; Dekany, I.; Fendler, J. H. *J. Am. Chem. Soc.* **1997**, 119, 6821.
- (92) Lvov, Y.; Decher, G.; Sukhorukov, G. *Macromolecules* **1993**, 26, 5396
- (93) Lvov, Y.; Haas, H.; Decher, G.; Moehwald, H.; Mikhailov, A.; Mtchedlishvili, E.; Morgunova, E.; Vainshtein, B. *Langmuir* **1994**, 10, 4232.
- (94) Fendler, J. H.; Meldrum, F. C. *Adv. Mater.* **1995**, 7, 607.
- (95) Kotov, N. A.; Dekany, I.; Fendler, J. H. *J. Phys. Chem.* **1995**, 99, 13065.
- (96) Schlenoff, J. B.; Dubas, S. T.; Farhat, T. *Langmuir* **2000**, 16, 9968.
- (97) Izquierdo, A.; Ono, S. S.; Voegel, J.-C.; Schaaf, P.; Decher, G. *Langmuir* **2005**, 21, 7558.
- (98) Cho, J.; Char, K.; Hong, J.-D.; Lee, K.-B. *Adv. Mater.* **2001**, 13, 1076.
- (99) Donath, E.; Sukhorukov, G.; Caruso, F.; Davis, S. A.; Moehwald, H. *Angew. Chem. Int. Ed. Engl.* **1998**, 37, 2201.
- (100) Caruso, F.; Caruso, R. A.; Moehwald, H. *Science* **1998**, 282, 1111.
- (101) Park, J.; Hammond, P. T. *Adv. Mater.* **2004**, 16, 520.
- (102) Tompkins, H. G.; McGahan, W. A. *Spectroscopic Ellipsometry and Reflectometry: A User's Guide*, John Wiley & Sons, Inc., New York, 1999.

Chapter 2

2. Synthesis and Characterization of Functional Defects in Colloidal Photonic Crystals

2.1 Preamble

From the early days of photonic crystals,^{1,2} the development of methods to build up periodic dielectric structures has grown parallel to the interest in creating ways to introduce defects within them in a controlled manner.³ Properly designed extrinsic doping can serve as a platform for waveguiding, resonator cavities, and ultra-narrow optical filters.⁴⁻⁶ Several methods for the integration of defect structures into CPCs and other 3D photonic crystals have been reported (see 1.2.3). However, the incorporated defect states are of a passive nature and cannot be addressed by external stimuli. In this chapter, I present a set of techniques that allow for the preparation of CPCs with embedded active defect layers. The active element is a chemically functional thin film that interrupts the periodicity of a CPC and leads to a responsive intragap transmission state.

2.2 Introduction

Passive defects can be introduced into self-assembled CPCs by subsequent top-down inscription methods such as electron-beam lithography or laser writing.⁷⁻¹¹ In a bottom-up method, a monolayer of spheres of an arbitrary diameter serving as passive impurity state has been embedded into the bulk between two CPCs by Langmuir-Blodgett transfer.^{12,13} Chemical vapor deposition (CVD) has been used to sandwich a silica defect slab between two inverted silica CPC layers.^{14,15} Here, I present two bottom-up methods for preparing CPCs with chemically active planar defects. The defect is based on a functional thin film that is either prepared in a LbL self-assembly fashion or by spin-coating. This opens the door to the preparation of defect layers from a myriad of functional materials such as polymers, biopolymers, dyes, quantum dots and other particles, to name a few.

In both methods, defect CPCs are prepared according to the following concept: I start with a mechanically stabilized bottom-CPC that is self-assembled from monodisperse silica or

polymer spheres. The planar defect is formed on the surface of the bottom-CPC and a top-CPC is grown over the defect layer to complete the structure. Monodisperse sphere synthesis, CPC crystallization and mechanical stabilization as well as the developed defect incorporation techniques are described in the following sections. The preparation steps are accompanied by SEM and optical characterization. Also, theoretical simulations comparing the optical properties of CPCs and defect CPCs are included.

2.3 Colloidal Photonic Crystal Synthesis

2.3.1 Monodisperse Spheres

2.3.1.1 Silica Spheres

Highly monodisperse silica spheres were synthesized following a modified Stöber-Fink-Bohn method, which involves multiple re-growth cycles as described by Giesche.^{16,17} Briefly, the spheres are synthesized by ammonium hydroxide catalysed hydrolytic polycondensation of tetraethoxysilane in ethanol. The particle size can be controlled by the ratio of employed reactants. In order to maintain low polydispersity, seeds for times smaller than the needed diameter are synthesized and used for re-growth. The seeds typically have a polydispersity of about 5 - 10 %. The absolute variation is usually retained during re-growth so that a final polydispersity of about 1.3 - 2.5 % is achieved. The method is suitable for the preparation of sphere diameters between 180 nm - 1.5 μm . Before crystallization is possible, the spheres are thoroughly cleaned by consecutive centrifuging, decanting and redispersing in ethanol. Doublets (two spheres fused together) and secondary seeds are sometimes formed in low concentrations during synthesis. They can be removed by fractioning using sedimentation.

2.3.1.2 Polymer Spheres

Monodisperse polymer spheres are generally synthesized from styrene or acrylate derivatives in an emulsion polymerization process. Suitable candidates for the preparation of CPC sandwiches with LbL-self-assembled defect layer are polymethylmethacrylate (PMMA) spheres with polyglycidylmethacrylate (PGlyMA) shell, for example. Thermal polymerization of the epoxy-groups in the glycidylmethacrylate (GlyMA) units allows for

good mechanical stabilization of the crystallized spheres¹⁸ - a crucial factor for the buildup of defect CPCs (see 2.3.3). The method of choice for the sphere preparation is surfactant-free emulsion polymerization:¹⁹⁻²¹ A water-soluble radical initiator is added to an emulsion of monomer in water. Amphiphilic oligomers are formed that act as surfactant and form micelles. Subsequent polymerization takes place in the interior of the micelles and additional monomer is supplied from the monomer droplets. The sphere size can be controlled by the initial water/monomer ratio. To obtain core-shell spheres, a second monomer is added to the reaction batch once the first monomer is converted. Similar to the preparation of silica spheres, additional work-up steps are necessary. The polydispersity of the resulting spheres (about 2 %) and the range of sphere diameters that can be prepared are comparable to that of silica colloids. However, polymer spheres are less immune towards exposure to heat, solvents or other chemicals compared to their silica equivalents. The preparation of defect CPCs is possible if the LbL option is chosen, but subsequent active addressing of the defect state by means of chemistry is restricted. Hence, the research presented in this work mainly focuses on silica spheres as defect CPCs building blocks.

Table 2.1 shows a list of the prepared monodisperse sphere dispersions of different sphere diameters and materials :

Table 2.1: Monodisperse sphere dispersions of different sphere diameters and materials.

Spheres	Diameter (nm)	Polydispersity %
SiO ₂	255	2
SiO ₂	280	1.5
SiO ₂	625	2
PMMA/PGlyMA	260	2.5

2.3.2 Crystallization

The methods I used for the crystallization of monodisperse silica or polyacrylate spheres to CPCs are all based on the concept of capillary force induced self-assembly on a flat vertical substrate (Figure 2.1).

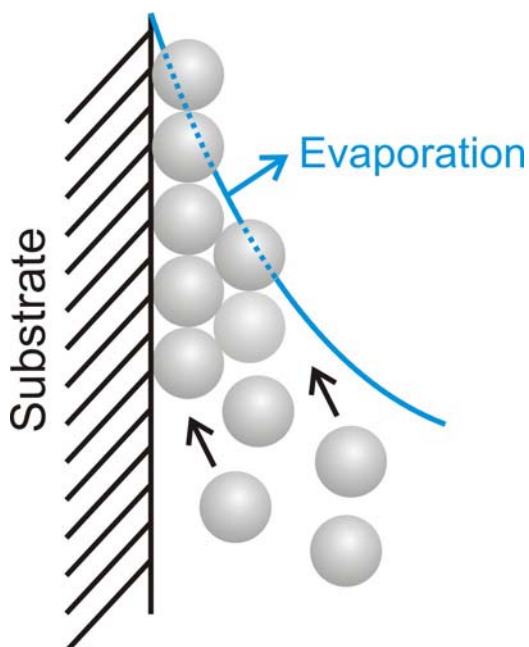


Figure 2.1: Schematic representation of evaporation induced self-assembly on a flat vertical substrate.

Silica spheres were crystallized by evaporation induced self-assembly as reported by Colvin *et al.*²² A previously thoroughly cleaned substrate (e.g. a glass slide) is vertically placed into a colloidal dispersion. As the dispersion agent ethanol evaporates, spheres are drawn to the meniscus, where they form a high quality fcc crystal. The thickness of the film can be precisely controlled by varying the colloidal volume fraction in the suspension (see 7.1.2.1). Unfortunately, this method is not usable for silica spheres larger than about 450 nm, since their sedimentation velocity is faster than the ethanol evaporation rate. Hence, the meniscus of spheres is depleted and the colloidal crystal formation is stopped. The problem can be solved by providing "assistance" to the dispersion to maintain the larger diameter spheres in solution. I worked with low-pressure evaporation induced self-assembly, where the crystallization is performed in a low-pressure chamber (around 45 Torr) to accelerate the evaporation rate of the dispersion agent to the same level as the sedimentation rate.

Polyacrylate spheres were crystallized best by slowly drawing a vertically placed substrate out of the corresponding aqueous dispersion.¹² For this purpose, a small electric motor is

used operating at a draw rate of about 100 nm/s. In this case, the slow evaporation rate of water is compensated by constant movement of the immersed substrate against gravity.

SEM images in cross-section and optical properties of the prepared high-quality CPCs are shown and discussed in sections 2.4 and 2.5.

2.3.3 Mechanical Stabilization

For the preparation of defect CPC sandwich structures, mechanical stabilization of the crystallized spheres is necessary. Mechanical stabilization means interconnection of the spheres as well as connection of the bottom sphere layer to the substrate by covalent bonds. During this process, small "necks" are formed at the sphere connection points and the procedure is sometimes referred to as "necking".

In case of silica CPCs, I used silica CVD as necking method.²³ In a specially designed apparatus, a silica CPC crystallized on a glass substrate is subsequently exposed to water and SiCl_4 vapors with a nitrogen drying sequence in between. In more detail, $\text{SiCl}_{4(l)}$ and water are placed in two parallelly connected bubble counters through which a nitrogen stream is flowed. This flow transports either of the reactants to the reactor chamber where the colloidal crystal is located. A porous glass septum placed between the bubble counters and the reactor favors the homogeneity of the reactive gas in the sample compartment. Exposure of the sample to water vapor covers the spheres in the lattice with a layer of water, hydrogen bonded to the highly hydroxylated surface of the silica particles. This water reacts with the $\text{SiCl}_{4(g)}$ flow to form silica. The nucleophilic attack of SiCl_4 by H_2O results in the formation of silicic acid $\text{Si}(\text{OH})_4$ and HCl , the latter of which, in turn, may catalyze the polycondensation of $\equiv\text{Si}-\text{OH}$ bonds to form water and siloxane bonds. This gives rise to the formation of a thin continuous silica layer that coats the microspheres and connects them to each other as well as to the glass substrate (Figure 2.2a).

CPCs from PMMA spheres with PGlyMA shell were necked by thermal polymerization of the epoxy-groups in the GlyMA units of adjacent spheres (Figure 2.2b).¹⁸ Also, heat induced covalent bonds between the silanol groups of the glass substrate and the PGlyMA shell epoxy-units promote adhesion between substrate and CPC. The CPC is simply heated at about 90°C until the desired mechanical stability is reached.

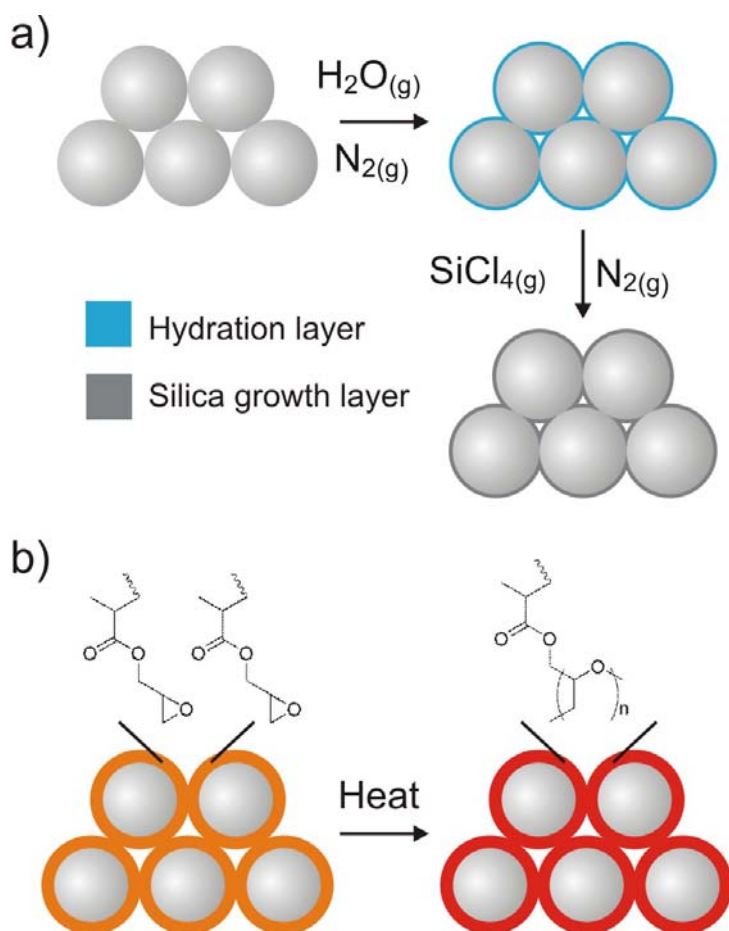


Figure 2.2: Mechanical stabilization of CPCs from a) silica spheres and b) PMMA/PGlyMA core-shell spheres. (Schematical illustration)

2.4 Defect Incorporation

2.4.1 Method 1 (LbL self-assembly)

In method 1, the defect consists of a LbL self-assembled multilayer thin film. As shown in section 1.3.1.1, the LbL technique is a simple and versatile method that allows for the incorporation of diverse charged materials and for thickness control on the molecular level (± 2 nm). However, if we use the colloidal crystal directly as substrate and perform the LbL process as described in chapter 1, LbL coating of all sphere surfaces facing the dissolved multilayer species will occur. The multilayer is not exclusively formed on top of the CPC as desired. A solution to this problem is microcontact transfer printing.²⁴ I pre-form a LbL multilayer stack separately onto a flat piece of PDMS and the entire multilayer is transfer printed onto the top surface of a mechanically stabilized CPC. A

second CPC is grown over this surface layer to complete the structure. The procedure is schematically represented in Figure 2.3.

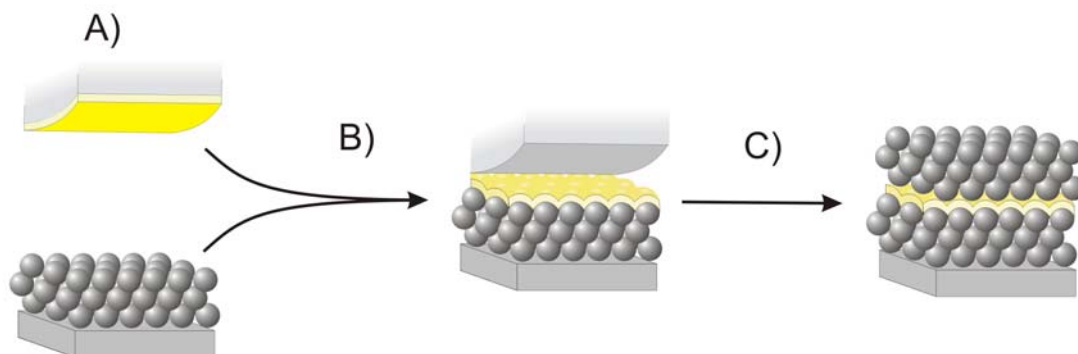


Figure 2.3: Schematic illustration of method 1: a) Growth of a LbL multilayer onto a flat PDMS stamp. b) Transfer printing of the multilayer stack onto the mechanically stabilized bottom CPC. c) Crystallization of the top CPC.

The thickness of the defect layer can be varied by the thickness of the transfer printed multilayer stack, or by repeated printings. To successfully transfer the multilayer thin film from the PDMS sheet to the CPC surface, the interactions between the base-layer and the PDMS surface must be weaker than the interactions between the top-layer and the surface of the colloidal crystal. For this purpose, poly(allylamine hydrochloride) (PAH) is always used as base-layer in the LbL self-assembly process on the PDMS sheet. The top-layer is chosen to be oppositely charged to the surface charge of the substrate onto which the film is transferred. The reason for the choice of a PAH base-layer is two-fold: Firstly, the hydrophobic backbone of PAH accommodates the adsorption of a charged initial layer to the hydrophobic PDMS surface. Secondly, the non-electrostatic interactions of the PAH hydrocarbon backbone with the hydrophobic PDMS surface is weaker than the electrostatic interactions between the charged top-layer and the charged CPC surface (negative surface charge for a plain silica CPC for example). Hence, the conditions for successful transfer printing are fulfilled.

2.4.2 Method 2 (Spin-coating)

The LbL concept, method 1 is based on, allows for the incorporation of a large variety of functional materials into the defect layer. It was developed right in the beginning of my PhD work and employed for the preparation of most of the samples that I used in the switching and monitoring experiments described in the following chapters. However, the technique is limited to polymers, molecules or particles that are highly charged and the solvent is aqueous. Method 2 was developed later on, to compensate the deficiencies of

method 1 and it is of complementary nature. It allows for the preparation of defect layers from a wide variety of polymers or particles that dissolve in hydrophobic solvents. Here, the defect layer is prepared by spin-coating. Analogously to method 1, the defect cannot be directly spin-coated on the bottom-CPC surface, because penetration into the CPC voids occurs. The key to preventing infiltration of the cladding opal layer during the spin-coating process is filling the CPC voids with a suitable sacrificial material. Following spin-coating of the defect, the filling material is removed and the second CPC grown on top to complete the structure (Figure 2.4). The use of a sacrificial substrate has been reported in the preparation of free-standing thin films;²⁵ in our case a sacrificial CPC filling is crucial to confine the spin-coated defect material to the CPC surface and to block penetration into the opal voids. To obtain adhesion between the spin-coated defect layer and the bottom-CPC, a free-standing film and consequently also an overlayer of the filling on the opal surface is not desired. For this purpose ribose, a low-melting point sugar, is chosen, which is melt-infiltrated under vacuum into the voids of a mechanically stabilized silica CPC. To avoid the formation of a ribose overlayer on the CPC, a flat PDMS slab is pressed onto the surface of the ribose-CPC composite while heating under vacuum, allowing any excess sugar to flow out the sides of the sample. After cooling to solidify the ribose, the PDMS is carefully peeled off. Spin-coating is performed on top of the ribose infiltrated opal, followed by dissolving the sugar in water and growth of the top-CPC by self-assembly.

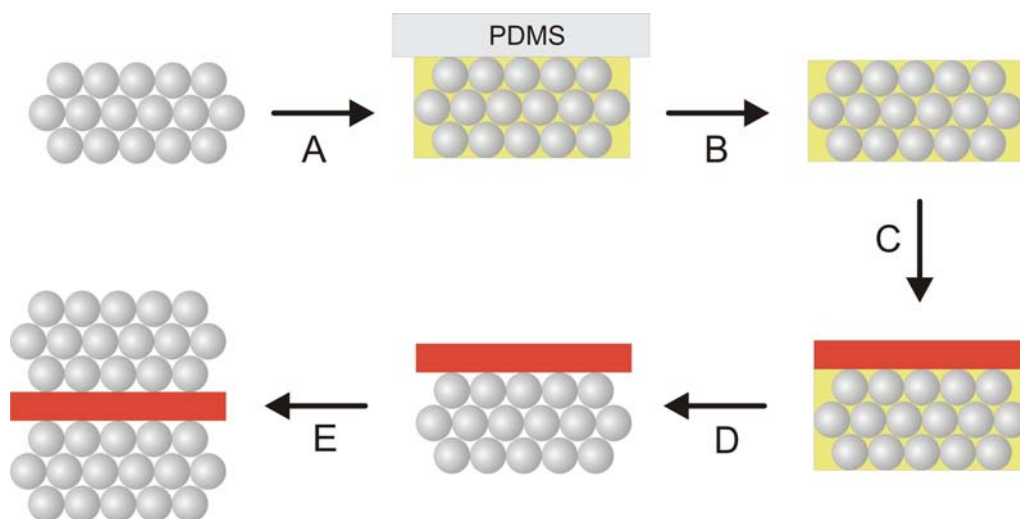


Figure 2.4: Preparation of a CPC with spin-coated defect layer (method 2). a) A sacrificial sugar filling is melted into the voids of a mechanically stabilized silica CPC. Top compression with a PDMS sheet prevents the formation of an overlayer. b) The PDMS sheet is carefully peeled off after complete infiltration and solidification of the sugar. c) Spin-coating of various materials from hydrophobic solvents can be performed on top of the infiltrated CPC. d) The sacrificial sugar filling is dissolved in water. e) A second silica CPC is grown to complete the defect structure.

A list of functional defect layer materials that I incorporated into CPCs using method 1 or method 2 is presented in Table 2.2. They are dealt with in detail in the following chapters of this thesis.

Table 2.2: Functional defect layer materials and preparation method.

Functional defect layer material	Preparation method	Detailed discussion (section)
Azo-benzene based polyelectrolyte (PAZO)	LbL self-assembly	3.2
Polyferrocenylsilane (PFS) polyelectrolytes	LbL self-assembly	3.4
Kraton	Spin-coating	3.5
Calf-thymus DNA	LbL self-assembly	4.3, 4.4
Poly-L-lysine	LbL self-assembly	4.5
Poly-L-glutamic acid	LbL self-assembly	4.5
Fluorescent dye (DCM) doped PMMA	Spin-coating	5.4

2.5 Scanning Electron Microscopy Characterization

Scanning electron microscopy (SEM) is a versatile characterization tool for direct visualization when the optical microscope resolution is insufficient. Briefly, an electron beam is tightly focused to form an electronic probe, which is raster-scanned on the sample surface using a combination of magnetic lenses. Electron-matter interaction creates a multitude of detectable species like secondary electrons, x-rays, γ -rays etc. The image is formed on a screen by using the signals to modulate the brightness of a cathode ray tube, that is raster scanned in synchrony with the electron beam.

Representative cross-sectional SEM images of CPCs with LbL self-assembled defect layer (method 1) are shown in Figure 2.5. In Figure 2.5a,b we can clearly recognize top- and bottom-CPC as well as the very homogeneous planar defect sandwiched between the two CPC cladding layers. The colloids are of uniform size and crystallized into high quality fcc-arrangements showing a smooth surface. The defect layer is of uniform controlled thickness without cracks or blank areas. In addition, the high resolution micrograph 2.5b demonstrates successful "necking" of the bottom-CPC. Cleaving of the sample was breaking the necks interconnecting the spheres and leaving holes as well as the corresponding knob-like counterparts at the former connection points. Slight distortions in the arrangement of the spheres are also caused by the cleaving process. Image 2.5c presents an example where the top-CPC partially flipped off during the SEM sample

preparation process. The micrograph impressively shows the topology of the LbL self-assembled polyelectrolyte defect layer that clearly reflects the surface structure of the underlying opal.

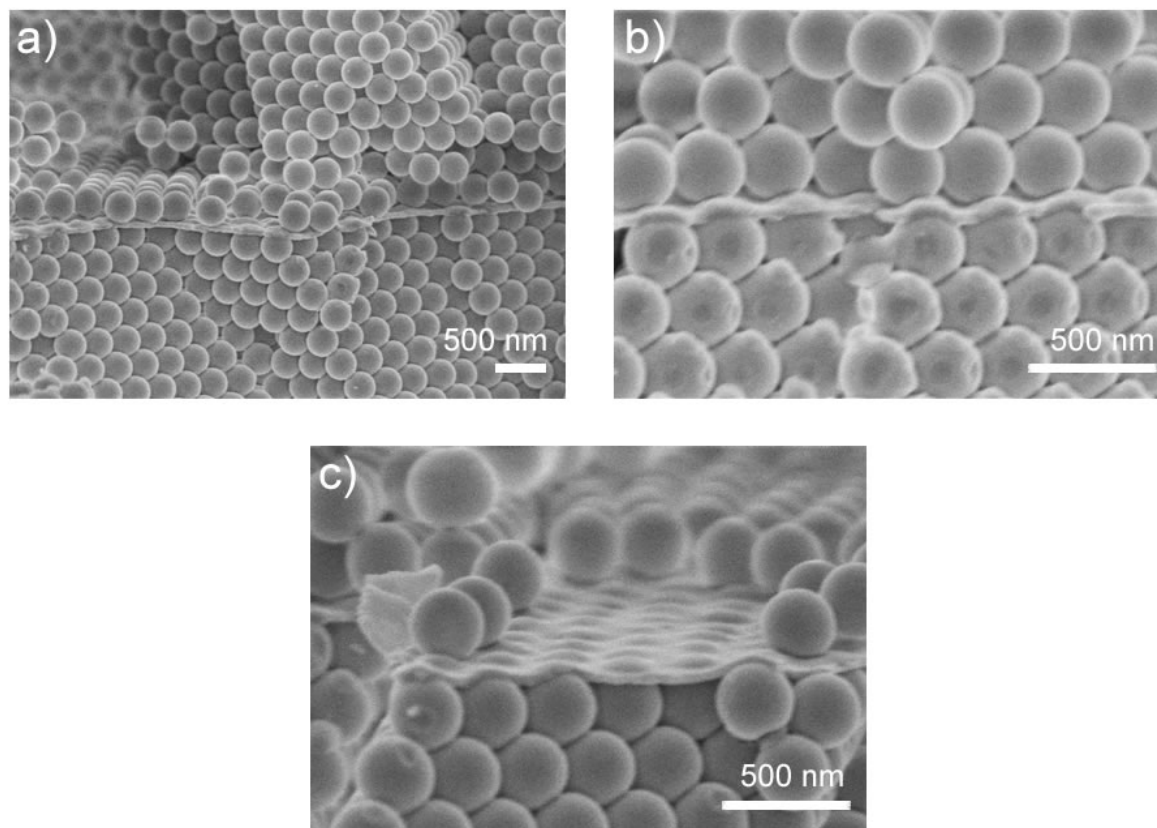


Figure 2.5: Representative cross-sectional SEM micrographs of silica CPCs with LbL self-assembled defect layer prepared according to method 1.

Representative cross-sectional SEM images of a ribose infiltrated bottom-CPC as well as the complete structure of a CPC with spin-coated defect layer prepared according to method 2 are shown in Figure 2.6. Highly monodisperse colloids crystallized to well-ordered fcc-arrangements and a homogeneous spin-coated planar defect can be noticed. Also, the images clearly prove that the formation of a ribose overlayer (Figure 2.6a) and the penetration of spin-coated defect material into the bottom-CPC voids (Figure 2.6b) are successfully prevented.

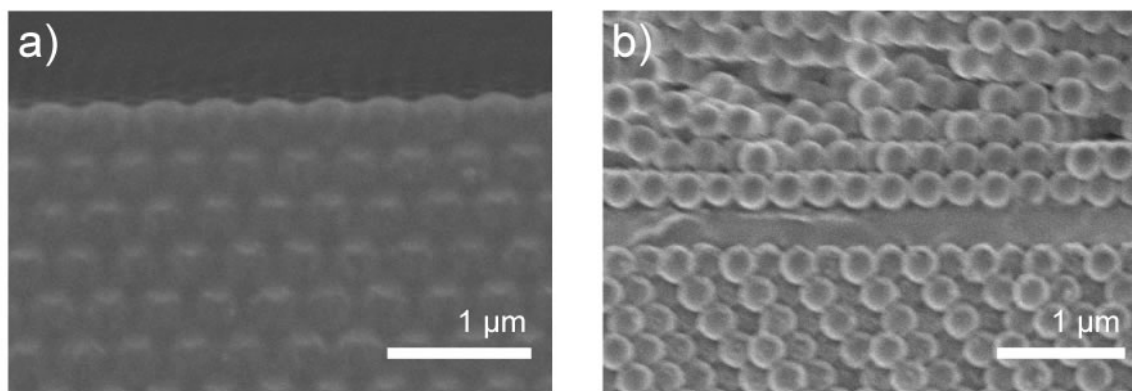


Figure 2.6: Representative cross-sectional SEM images at different preparation steps of method 2. a) Ribose infiltrated silica CPC. b) CPC with spin-coated dye doped PMMA defect layer.

2.6 Optical Characterization

Optical characterization was performed with a fiber optics spectrometer attached to an optical microscope. This setup allows for real time measurements especially important with respect to the switching and monitoring experiments with defect CPCs described in the following chapters. The samples were probed in transmission along the $[111]$ -axis of the colloidal crystal lattice.

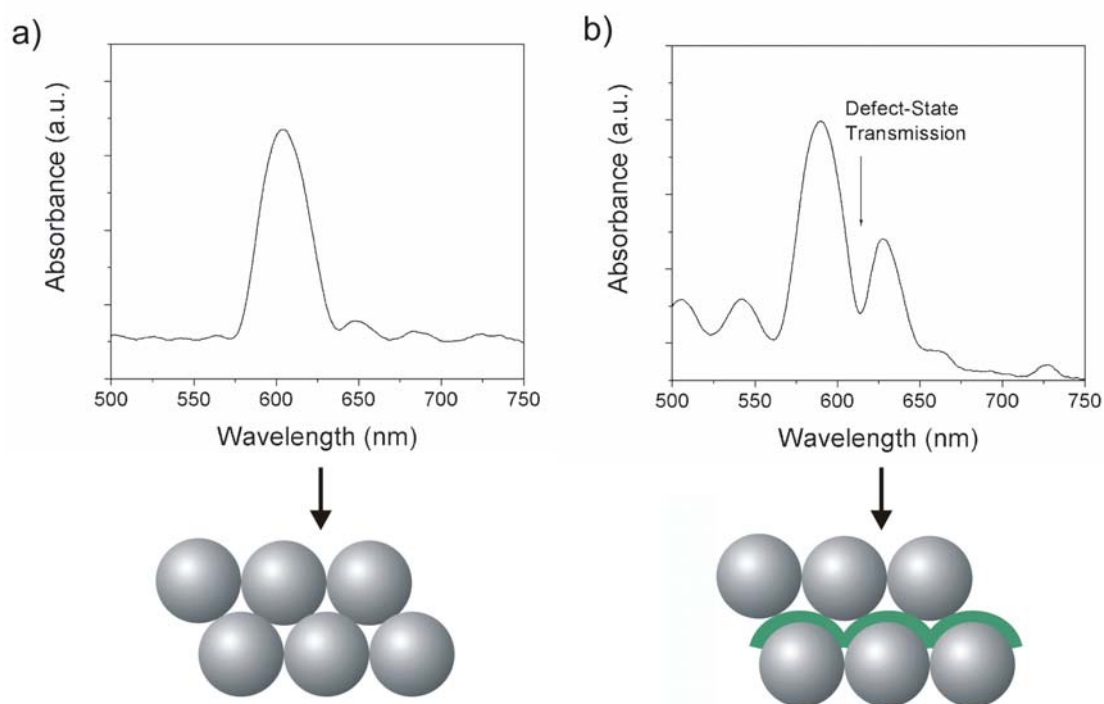


Figure 2.7: Optical spectra of a silica CPC (a) and a silica CPC with embedded polyelectrolyte defect layer (b). The samples are probed in transmission along the $[111]$ -axis of the colloidal crystal.

Figure 2.7a shows the optical spectrum of a high quality silica CPC self-assembled from monodisperse spheres with diameters of 280 nm. A clear maximum generally named the "Bragg-peak" reflects the opening of a photonic stop band along the CPC's [111]-direction. The labelling "absorbance" on the abscissa is equivalent to $\lg(1/T)$, the decadic logarithm of the reciprocal transmission ($T = I/I_0$). With respect to photonic bandstructures it does not refer to the classical meaning of "absorbance" resulting from actual chromophores, but simply describes the change in light intensities during transmission. Figure 2.7b demonstrates how the optical spectrum is modified when we interrupt the periodicity of the CPC by embedding a planar defect. If the defect layer is of a thickness and refractive index such that the resulting defect state is located within the photonic stop-band, we can observe a narrow defect transmission state located within the Bragg-peak. The position of the defect wavelength within the Bragg-peak depends on thickness and refractive index of the defect layer as well and can be shifted by varying those parameters. Here, the defect represents a polyelectrolyte multilayer with a thickness of about 100 nm and a refractive index of about 1.6.

In the following part, I will illustrate the changes of the optical spectra in course of the single defect CPC preparation steps:

The Bragg diffraction peak of the bottom-CPC is slightly red shifted upon mechanical stabilization (Figure 2.8) due to the formation of necks between the spheres and the increase in effective refractive index of the CPC (equation (1.5)).

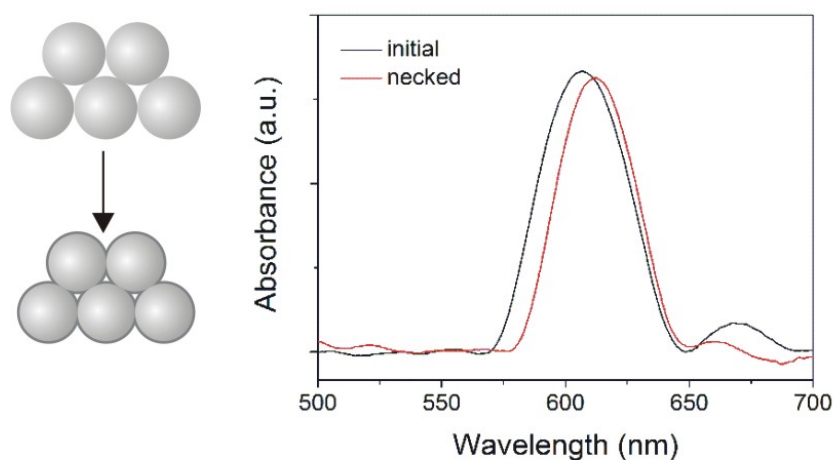


Figure 2.8: Optical transmission spectra at normal incidence of a silica CPC before and after mechanical stabilization.

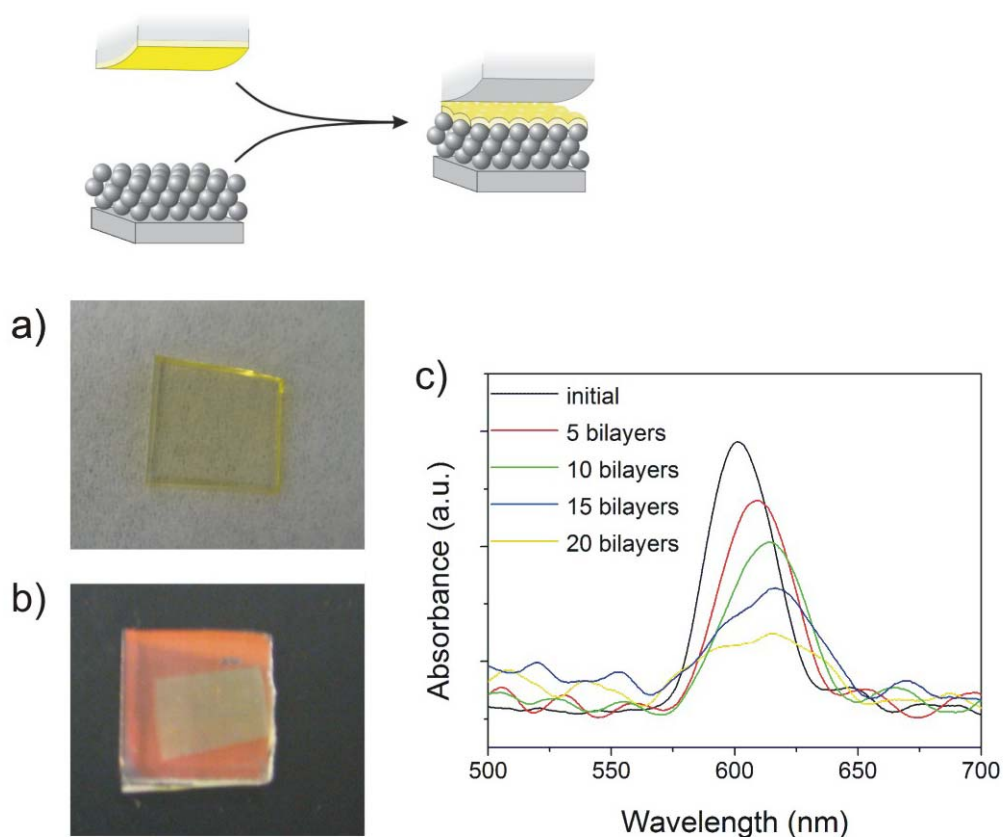


Figure 2.9: a) PDMS sheet with PAZO/PDAC polyelectrolyte multilayer (photograph). b) CPC with transfer printed PAZO/PDAC polyelectrolyte multilayer (photograph). c) Optical transmission spectra at normal incidence of a CPC with PAZO/PDAC polyelectrolyte multilayer surface defects of different thicknesses.

Figure 2.9a shows a photograph of a PDMS sheet with LbL self-assembled polyelectrolyte multilayer. PAH is used as base-layer, as explained in 2.4.1. Polydiallyldimethylammonium chloride (PDAC) and poly[1-[4-(3-carboxy-4-hydroxyphenyl-azo)benzenesulfonamido]-1,2-ethandiyl, sodium salt] (PAZO) (see section 3.2) present the successive polyelectrolyte pairs. The color results from the azo-benzene based PAZO polyelectrolyte. It helps us "visualize" the otherwise transparent film and the uniform coloring underlines a homogeneous film formation. In Figure 2.9b, we clearly see the multilayer film transfer printed onto the surface of a stabilized silica CPC on a glass substrate. The stop-band of the initial CPC is around 600 nm explaining the red reflection color of the material. Both samples present smaller sections (1-2 cm²) cut out of larger area samples initially prepared. Figure 2.9c shows the optical properties of the CPC with surface defects of different thicknesses. With increasing number of successively transfer printed bilayers, the initial Bragg-peak is red shifted, the intensity decreases and finally shoulders appear and the peak is broadened. This behavior is "periodical" meaning with increasing surface defect thickness, the peak is blue shifted

again and the intensity is growing until finally the initial spectrum is reached when the optical properties of the surface defect layer are in coincidence with the CPC dielectric modulation along the [111]-axis. Then the surface defect is no longer an actual defect (at least when probing along the [111]-axis) and the "periodic cycle" can start from the beginning. In this example, the CPC consists of 280 nm silica spheres. Thickness and refractive index of a PAZO/PDAC bilayer are 4.6 nm and 1.58, respectively, determined by variable angle spectroscopic ellipsometry (see 1.3.2.1). For this purpose, a known number of bilayers (in the linear growth regime) is microcontact transfer printed onto a silicon wafer presenting a suitable substrate for ellipsometry measurements. Thus, the preparation process is comparable to the actual defect layer synthesis.

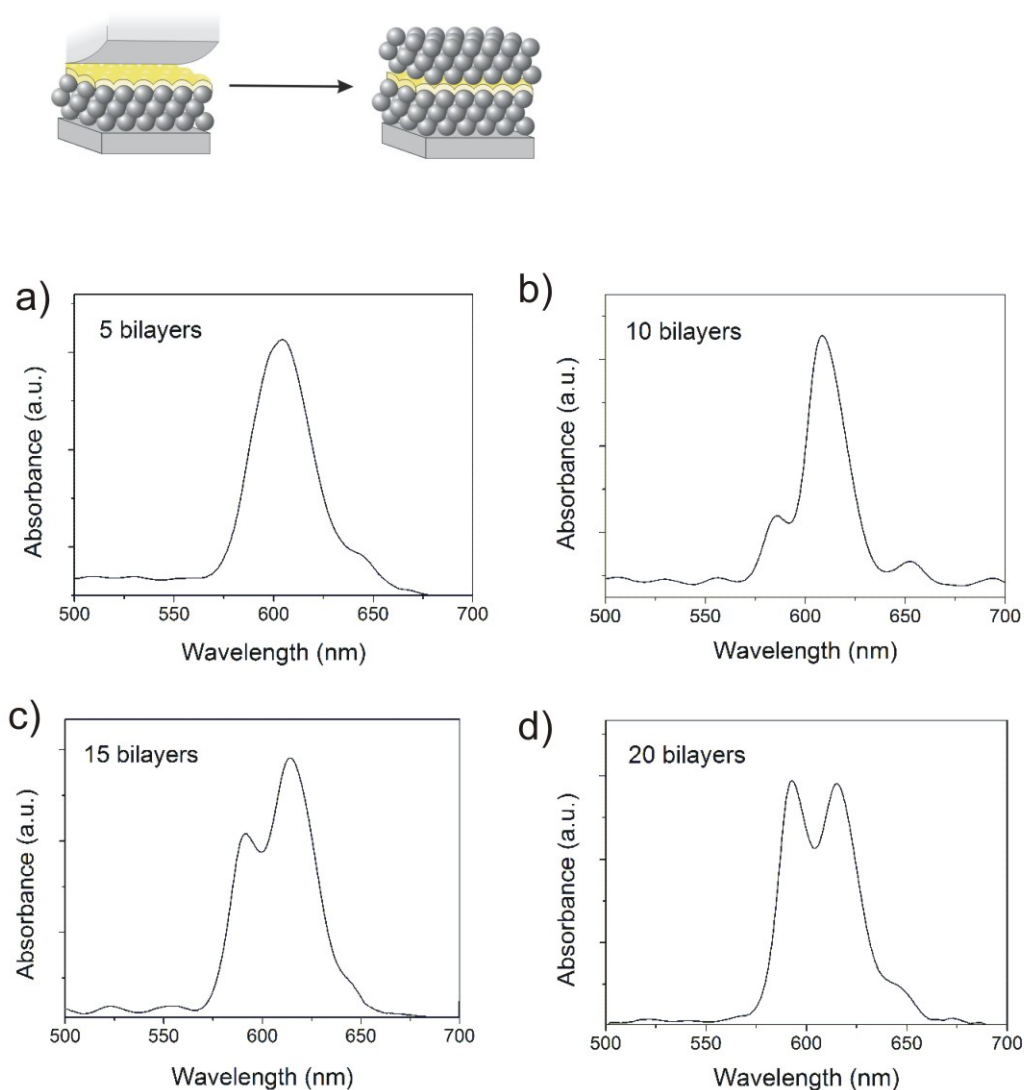


Figure 2.10: Optical transmission spectra at normal incidence of defect CPCs with PAZO/PDAC multilayers of different thickness.

Figure 2.10 shows the optical spectra of complete defect CPCs with embedded PAZO/PDAC defect layers of different thickness. We can see that with increasing numbers of bilayers, a defect transmission dip gradually shifts into the Bragg-peak from the blue band edge side. SWA-simulations²⁶ (see 1.2.4.1 and 2.7) and experimental observations demonstrate periodic shifts of the defect state from the blue to the red band edge of the Bragg-peak with increasing optical defect layer thickness. No defect states can be observed whenever the optical thickness of the defect layer coincides or nearly coincides with the dielectric modulation of the colloidal crystal lattice at normal incidence. Hence, for a PAZO/PDAC defect CPC consisting of 280 nm silica spheres (refr. index: 1.43) with a lattice spacing of ~ 230 nm (see equation (1.5)), the first order defect state is roughly located in the middle of the Bragg-peak at around 20 PAZO/PDAC bilayers (Figure 2.10c).

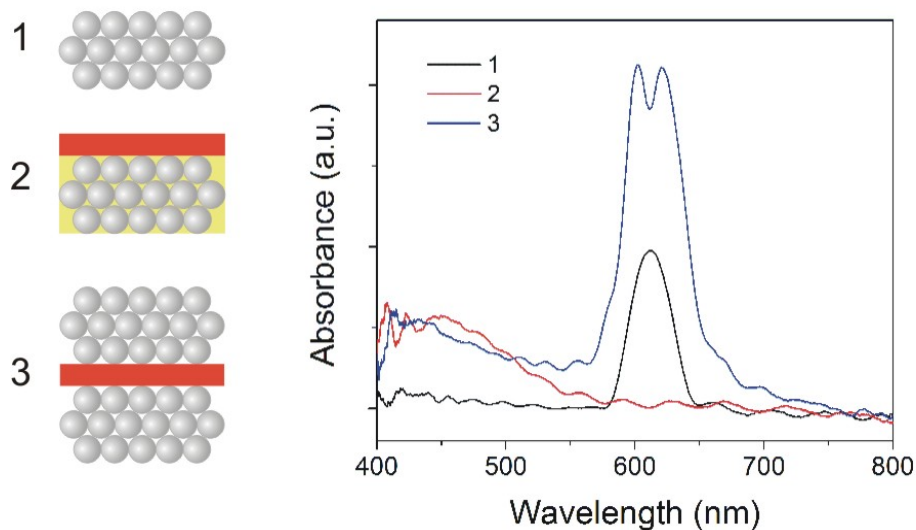


Figure 2.11: Optical spectra of a silica CPC with spin-coated PMMA/DCM defect layer at different preparation steps: (1) mechanically stabilized bottom-CPC; (2) sugar infiltrated bottom-CPC with spin-coated PMMA/DCM layer; (3) final structure. The spectra are taken in transmission along the CPC-[111]-axis.

We have dealt with the optical spectra of mechanically stabilized CPCs and of CPCs with surface and embedded defects. The samples analysed so far have been prepared according to method 1 and it is straightforward that the described concepts can also be transferred to method 2. However, method 2 requires additional ribose infiltration and dissolving steps. The corresponding optical spectra are shown in Figure 2.11. Here, the spin-coated defect layer consists of PMMA doped with laser dye 4-(dicyanomethylene)-2-methyl-6-(p-

dimethyl-aminostyryl)-4H-pyran (DCM). Ribose infiltration into the bottom-CPC voids leads to the expected disappearance of the Bragg peak caused by the large decrease in refractive index contrast. Additional absorbance between 400 and 550 nm after spincoating is a result of the DCM doped PMMA defect layer. After dissolving the ribose filling and crystallizing the top-CPC, the Bragg peak reappears and shows a higher intensity (caused by the increasing number of sphere layers) as well as an intragap defect state.

2.7 SWA-Simulations

I used the SWA-method as explained in section 1.2.4.1 to simulate transmission spectra of a CPC with and without planar defect (Figure 2.12a,b). As input parameters for the calculations I worked with a CPC thickness of 40 monolayers and spheres of refractive index $n = 1.43$ (like silica) and diameter of 280 nm. The planar defect of $n = 1.5$ and thickness 100 nm is introduced between the 20th and 21st sphere layer. These assumptions compare well to the actual experimental data of the defect CPCs discussed in the previous section. In addition, the spatial distribution of the square magnitude of the electric field is plotted in Figure 2.12c and Figure 2.12d. The calculations are done for the Bragg-peak maximum wavelength (λ_1) in case of the plain CPC and for the defect wavelength (λ_2) in case of the defect CPC. The spatial distribution is regarded along the CPC [111]-axis with the crystal surface as starting point. From such calculations, the different features of light propagation at those wavelengths can be clearly seen. Waves impinging on the crystal at the forbidden wavelength λ_1 become evanescent within the crystal, causing a high reflectance. At λ_2 , a resonance appears around the dielectric slab embedded within the crystal, highly increasing the probability for those photons to reach the transmission medium. Such phenomenon is observed as a sharp decay in the Bragg-peak.

Figure 2.12e shows the periodic variation of the defect state position as the thickness of the embedded dielectric slab is changed. The central frequency of the defect state oscillates periodically within the photonic gap between the high energy air band and the low energy dielectric band as already discussed in 2.6.

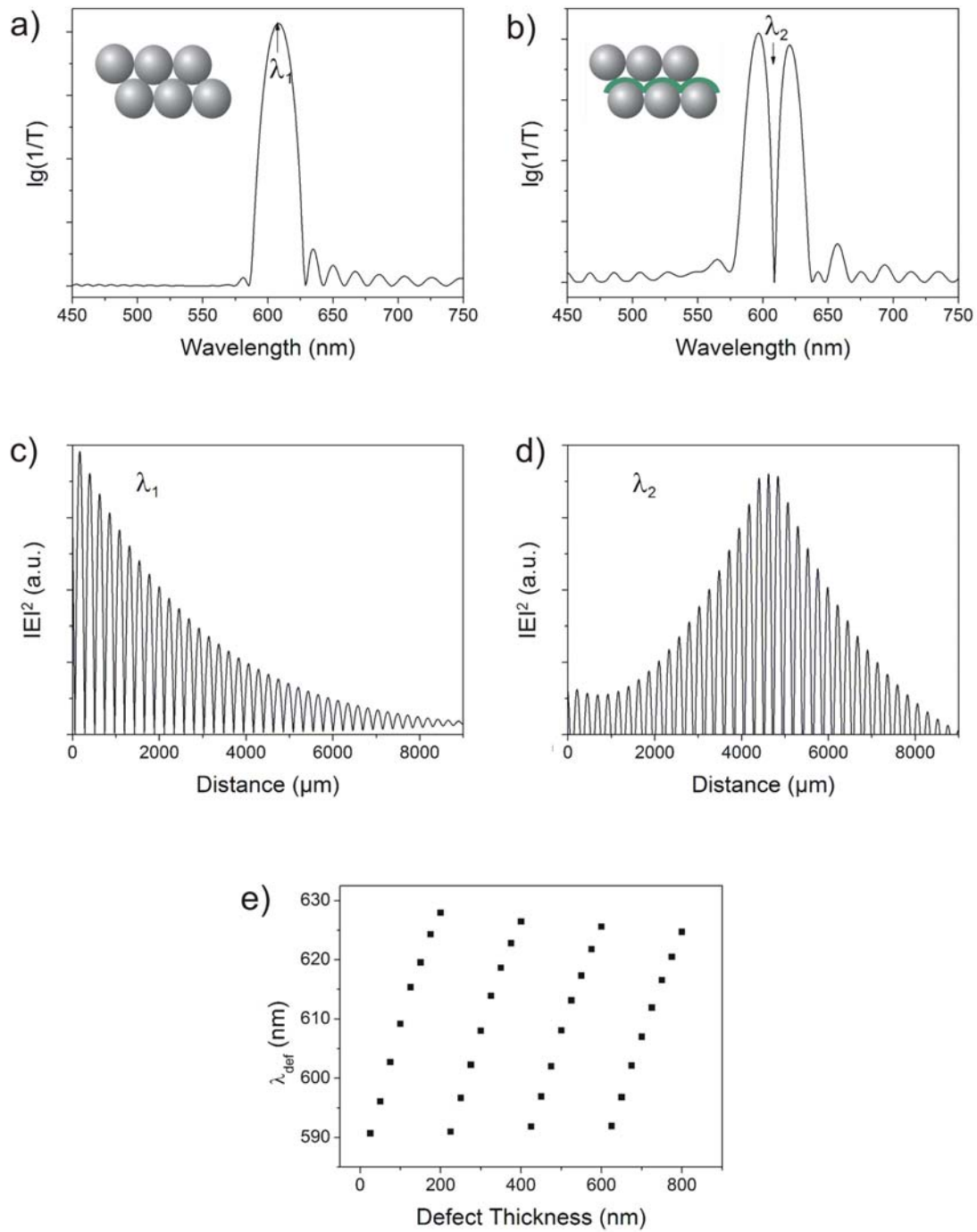


Figure 2.12: Calculated transmission spectra at normal incidence of a CPC (a) and a defect CPC (b). Spatial distribution of the square magnitude of the electric field for the wavelengths λ_1 (c) and λ_2 (d). e) Calculated position of defect state versus defect thickness. Input parameters: CPC spheres of $d = 280$ nm and $n = 1.43$, CPC thickness of 40 sphere layers, planar defect of $n = 1.5$ and thickness 100 nm between 20th and 21st sphere layer.

2.8 Conclusion

In summary, I presented two complementary bottom-up approaches for the construction of designed planar defects embedded in CPCs. The defect layer is based on a functional thin film that is either prepared by LbL self-assembly and microcontact transfer printing or by spin-coating from hydrophobic solvents. Hence, it can consist of a large variety of charged and non-charged materials. SEM micrographs clearly "visualize" the planar defect sandwiched between two CPC cladding layers. Optical spectroscopy measurements and SWA-simulations are nicely consistent with the unique defect structures prepared by these methods.

2.9 References

- (1) Yablonovitch, E. *Phys. Rev. Lett.* **1987**, *58*, 2059.
- (2) John, S. *Phys. Rev. Lett.* **1987**, *58*, 2486.
- (3) Yablonovitch, E.; Gmitter, T. J.; Meade, R. D.; Rappe, A. M.; Brommer, K. D.; Joannopoulos, J. D. *Phys. Rev. Lett.* **1991**, *67*, 3380.
- (4) Knight, J.; Broeng, J.; Birks, T.; Russel, P. *Science* **1998**, *282*, 1476.
- (5) Noda, S.; Chutinan, A.; Imada, M. *Nature* **2000**, *407*, 608.
- (6) Stoffer, R.; Hoekstra, H.; De Ridder, R. M.; van Groesen, E.; van Beckum, F. P. *H. Optical and Quantum Electronics* **2000**, *32*, 947.
- (7) Tetreault, N.; Miguez, H.; Yang, S. M.; Kitaev, V.; Ozin, G. A. *Adv. Mater.* **2003**, *15*, 1167.
- (8) Ferrand, P.; Egen, M.; Zentel, R.; Seekamp, J.; Romanov, S. G.; Sotomayor Torres, C. M. *Appl. Phys. Lett.* **2003**, *83*, 5289.
- (9) Xie, R.; Sekiguchi, T.; Li, D.; Yang, D.; Jiang, M. *J. Phys. Chem. B Lett.* **2006**, *110*, 1107.
- (10) Lee, W. M.; Pruzinsky, S. A.; Braun, P. V. *Adv. Mater.* **2002**, *14*, 271.
- (11) Jun, Y. H.; Leatherdale, C. A.; Norris, D. J. *Adv. Mater.* **2005**, *17*, 1908.
- (12) Egen, M.; Voss, R.; Griesebock, B.; Zentel, R. *Chem. Mater.* **2003**, *15*, 3786.
- (13) Massé, P.; Reculosa, S.; Clays, K.; Ravaine, S. *Chem. Phys. Lett.* **2006**, *422*, 251.
- (14) Tetreault, N.; Mihi, A.; Miguez, H.; Rodriguez, I.; Ozin, G. A.; Meseguer, F.; Kitaev, V. *Adv. Mater.* **2004**, *16*, 346.
- (15) Palacios-Lidon, E.; Galisteo-Lopez, J. F.; Juarez, B. H.; Lopez, C. *Adv. Mater.* **2004**, *16*, 341.
- (16) Stöber, W.; Fink, A.; Bohn E. J. *J. Colloid Interface Sci.* **1968**, *26*, 62.
- (17) Giesche, H. *J. Eur. Ceram. Soc.* **1994**, *14*, 205.
- (18) Lange, B.; Zentel, R.; Ober, C. K. *Polymer Preprints* **2006**, *47*, 517.
- (19) Goodwin, J. W.; Hearn, J.; Ottewill, R. H.; *Coll. Polym. Sci.* **1974**, *252*, 464.
- (20) Goodwin, J.W.; Ottewill, R.H.; Pelton, R.; Vianello, G.; Yates, D.E.; *Brit. Polym. J.*; **1978**, *10*, 173.
- (21) Egen, M.; Zentel, R.; *Chem. Mater.* **2002**, *14*, 2176.
- (22) Jiang, P.; Bertone, J. F.; Hwang, K. S.; Colvin, V. L. *Chem. Mater.* **1999**, *11*, 2132.
- (23) Miguez, H.; Tetreault, N.; Hatton, B.; Yang, S. M.; Perovic, D.; Ozin, G. A. *Chem. Commun.* **2002**, 2736.

- (24) Park, J.; Hammond, P. T. *Adv. Mater.* **2004**, *16*, 520.
- (25) Tang, Z.; Kotov, N. A.; Magonov, S.; Ozturk, B. *Nat. Mater.* **2003**, *2*, 413.
- (26) Software provided by Dr. Georg v. Freymann.

Chapter 3

3. Switching of Functional Defects in Colloidal Photonic Crystals

3.1 Preamble

In the previous chapter, I presented a set of bottom-up preparation techniques that allow for the synthesis of CPCs with active defect layers. Optical spectra showed a narrow intragap transmission state with a defect wavelength depending on the optical thickness of the embedded dielectric slab.

In this chapter, I demonstrate the incorporation of addressable molecules into the planar defect and show active tuning of the defect wavelength by several external stimuli. This is achieved by inducing changes in thickness and/or refractive index of the defect. The concept is illustrated in Figure 3.1.

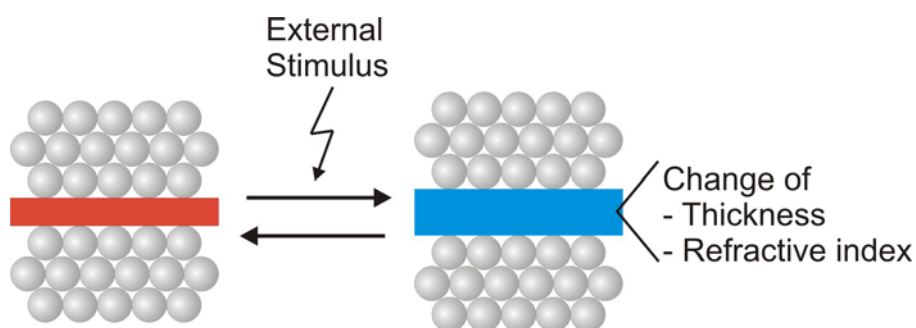


Figure 3.1: Schematic illustration of tunable defect CPCs.

3.2 UV-Switching

Chemical functionality was introduced into the defect layer for instance by incorporating the azobenzene based PAZO polyelectrolyte into the multilayer stack according to preparation method 1 (see 2.4.1). The azo-group in PAZO undergoes trans-to-cis photoisomerization during UV-light exposure and partial thermal backisomerization when the molecule is left in the dark¹ (Figure 3.2).

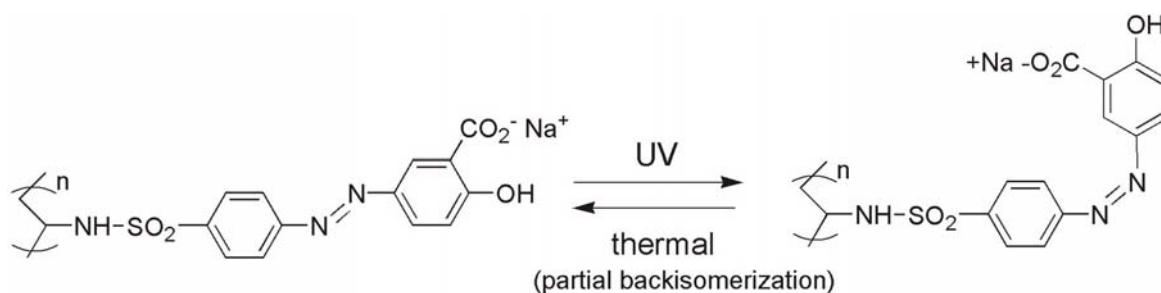


Figure 3.2: UV-induced trans-to-cis isomerization and partial thermal backisomerization of the azo-group in a PAZO polyelectrolyte molecule.

I tried to exploit this conformational change to vary the optical density of the defect layer and to induce an optical shift of the defect mode. PAZO was chosen as azobenzene containing polyelectrolyte since it allows for homogeneous LbL self-assembly, it is commercially available and the isomerization kinetics of PAZO containing multilayers as such have been investigated in previous studies and can be used as reference.¹

Irradiating a silica CPC (sphere diameter: 280 nm) with embedded microtransfer-printed PAZO/PDAC multilayer (thickness: 65 nm, refr. index: 1.58) with UV-light (Xe-lamp, 180 W) at constant temperature leads to a small but reproducible blue shift of the defect state due to trans-cis isomerization of the PAZO molecules (Figure 3.3a). The stopband edges remain constant, implying that the CPC cladding layers are not affected by UV-irradiation. The defect state position dependence on the UV-irradiation time is plotted in Figure 3.3c, and is best fitted using an exponential decay curve. After 120 min a stationary state is reached. This is in agreement with Stroeve *et al.* reporting on the kinetics of photoisomerization of PAZO multilayer films.¹

Leaving the PAZO/PDAC-opal heterostructure in the dark leads to partial backisomerization of the azo-component (~50% based on wavelength shift), and consequently to a red shift of the defect state towards the original position (Figure 3.3b). The defect position versus the backisomerization time is plotted in Figure 3.3d, and compares well to previous studies of the PAZO alone.¹

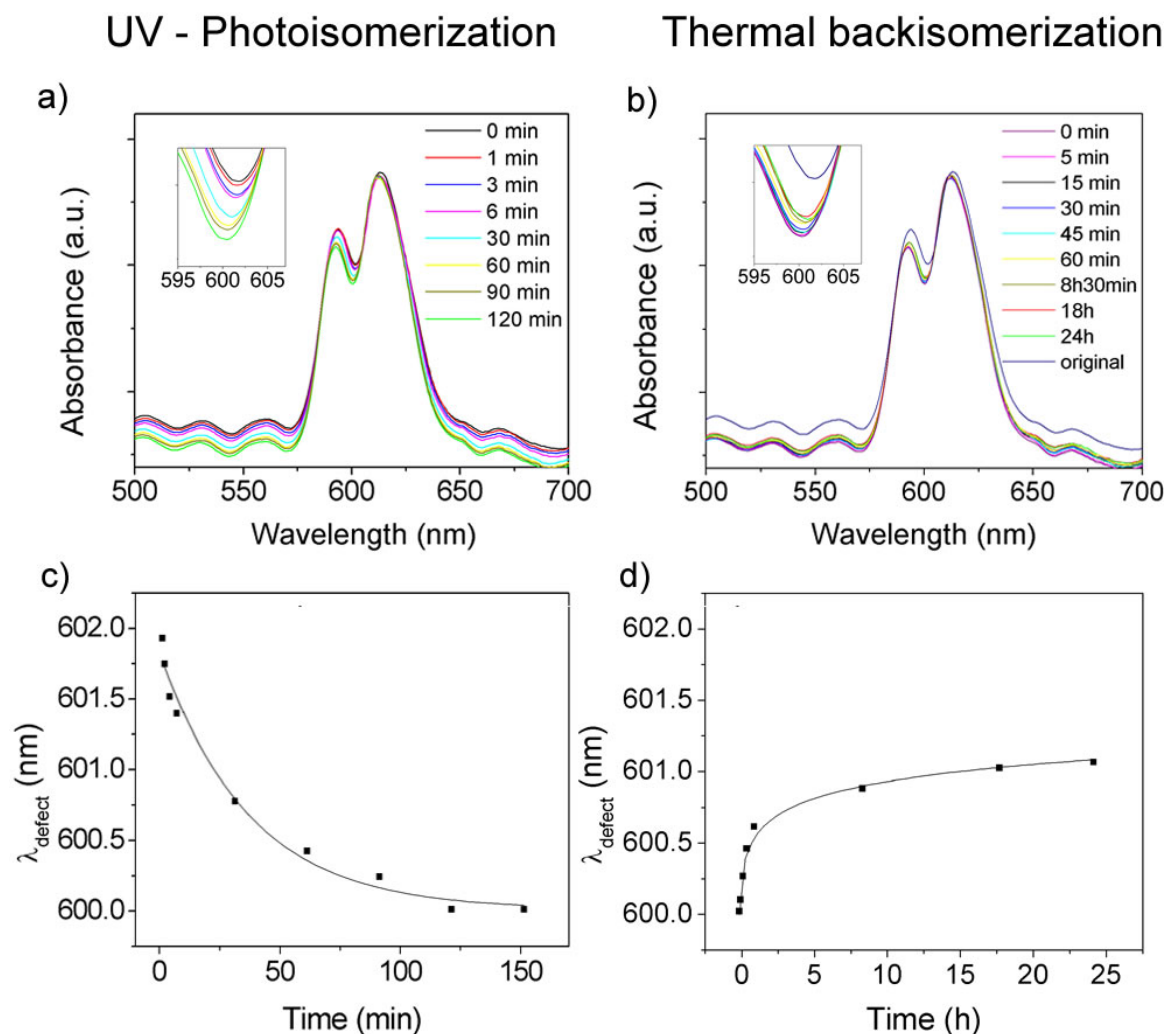


Figure 3.3: Top: Transmission spectra of a PAZO/ PDAC defect CPC at different a) UV-irradiation and b) backisomerization times. The insets show a magnification of the defect state positions. Bottom: Dependence of defect state wavelength on c) UV-irradiation and d) backisomerization time. Exponential and logarithmic fits are applied.

Ellipsometry measurements show that the UV-induced trans-cis isomerization causes 10% decrease in thickness and 5% increase in the refractive index of PAZO/PDAC multilayer films. I used these parameters as input to simulate the observed optical spectra with the SWA-model and the theoretically calculated defect shift is found to be in perfect agreement with experimental observations (Figure 3.4). Slight deviations between experimental and calculated data can be observed, which is expected since the simulations do not take into account intrinsic defects as well as the three-dimensional topology of the defect.

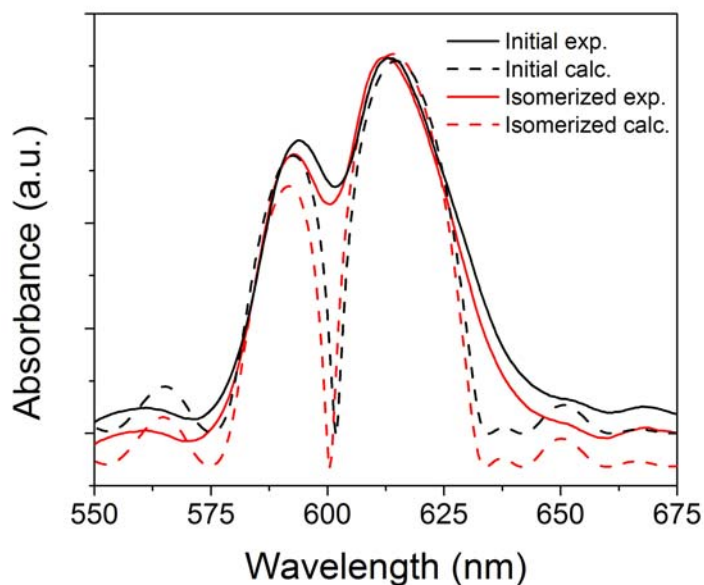


Figure 3.4: Experimental (solid lines) and calculated (dotted lines) transmission spectra (normalized) of a PAZO defect CPC in the initial and photoisomerized form.

The data obtained by ellipsometry also explain the small defect wavelength shift: In agreement with SWA-calculations, a decrease in defect thickness causes a blue shift whereas an increase in refractive index leads to a red shift of the defect mode. Consequently we have two counteracting effects partially cancelling out each other.

However, since the optical thickness of the defect layer is changed by a factor and not by a summand and the defect wavelength oscillates between air and dielectric band with the periodicity of a constant defect layer thickness increment (see Figure 2.12e), larger shifts of the defect mode can simply be achieved by working with higher defect modes, meaning thicker defect layers.

All ellipsometry control-experiments described in this work are performed as explained in chapter 2: I microcontact transfer print a multilayer stack of the corresponding polyelectrolytes separately on a silicon wafer and I investigate the initial sample as well as the sample modified according to the defect CPC switching experiment. Thus, the changes in thickness and refractive index measured by ellipsometry are comparable to the actual changes in the defect layer.

3.3 Thermal-Switching

Additionally, tuning the defect state can also be achieved by thermal cycling of polyelectrolyte multilayer defect CPCs. By heating and cooling a PAZO/PDAC defect CPC between 10°C and 80°C, completely reversible shifts of the photonic defect state and the stopband edges can be observed after 3-5 “conditioning” cycles (Figure 3.5). The sample was kept in a closed box on a thermoelectric Peltier element, and transmission spectra were taken in temperature increments of 10°C at a rate of 10°C/min. The blue shift of defect state and Bragg peak with increasing temperature is due to the evaporation of water trapped in the planar defect as well as in the voids of the CPCs. The water loss leads to both a decreasing thickness of the planar defect and a decreasing effective refractive index of the opal. Upon cooling the sample, ambient humidity condenses back into the hydrophilic voids of the CPCs and into the defect, red shifting the defect state and band edges. The temperature dependency of amorphous silica itself and of the defect polymer is negligible.²

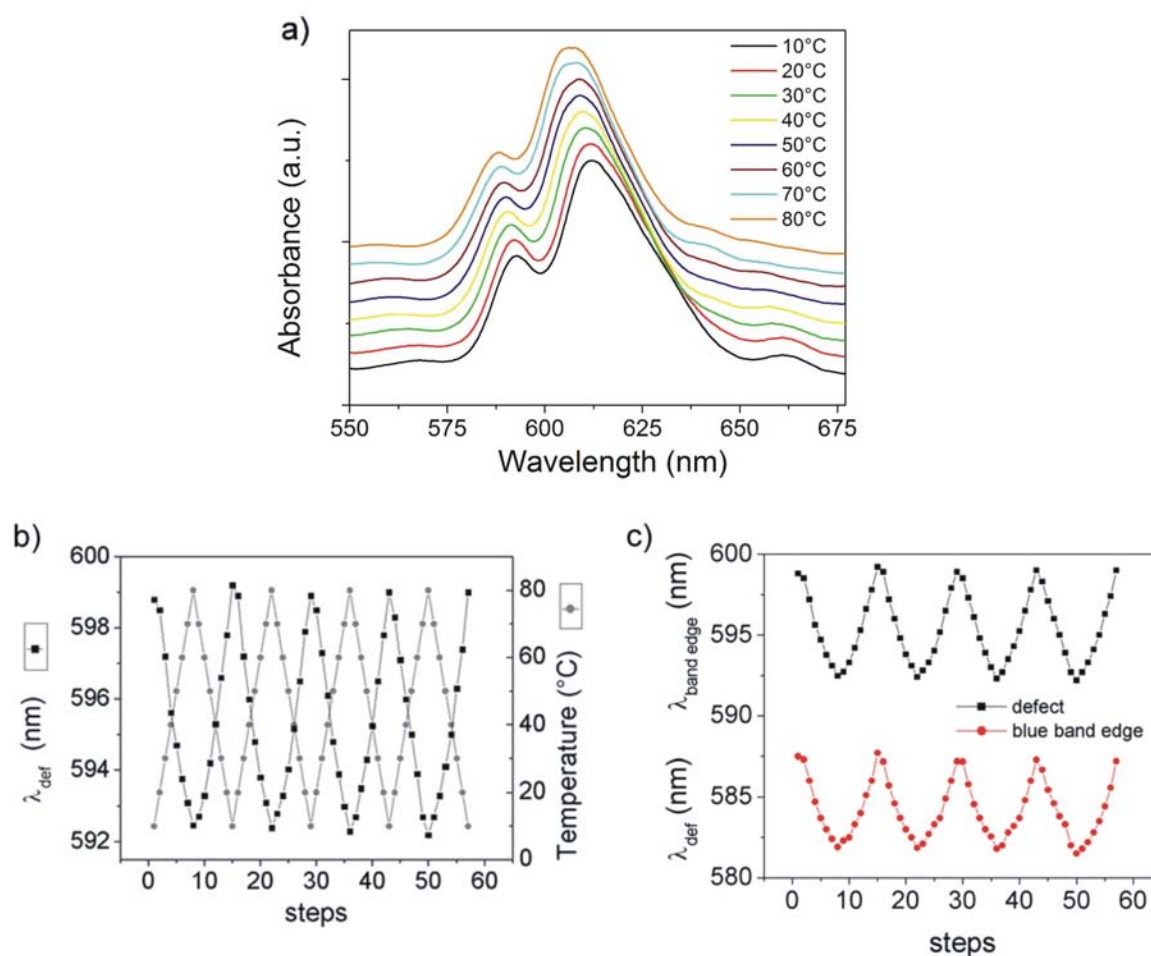


Figure 3.5: a) Transmission spectra of a PAZO/PDAC defect CPC at temperatures between 10°C and 80°C (staggered). b) Dependence of defect state wavelength on temperature during heating and cooling cycles (“conditioning” cycles are not shown). c) Changes in defect state and blue band edge wavelength during the applied heating and cooling steps.

Using the SWA-model, the observed behavior can be simulated by taking into account a 10 and 20 vol% water loading in the CPC voids and defect state, respectively, at 10°C, and a near-zero humidity level when the temperature was raised to 80°C (Figure 3.6). Thermal gravimetric analysis (TGA) shows the water content to be 9.14 and 18.1 vol%, respectively. These thermal experiments support the claim that the UV-induced defect state tuning is dominated by trans-cis isomerization, and not photo-thermal effects.

It is interesting to notice that the temperature induced defect mode switching is highly reversible and reproducible and does not seem to be effected by changes of the ambient relative humidity. A potential explanation is the formation of a constant high humidity layer at the air/substance interface since evaporated water cannot be removed immediately.

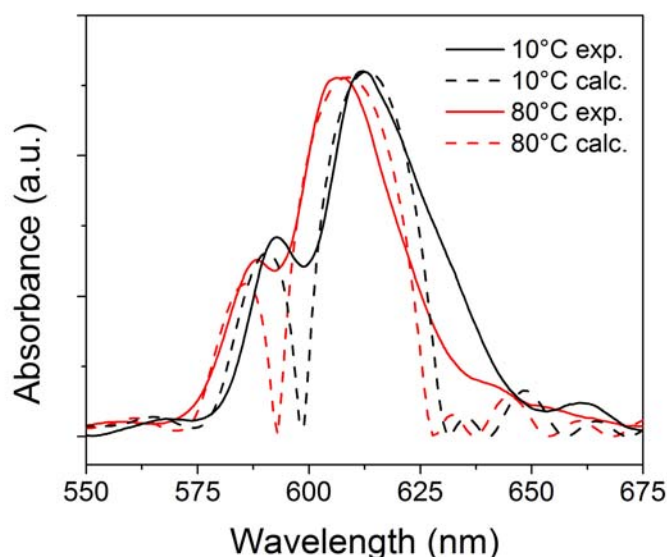


Figure 3.6: Experimental (solid lines) and calculated (dotted lines) transmission spectra (normalized) of a PAZO/PDAC defect CPC at 10°C and 80°C.

3.4 Redox-Switching

Furthermore, CPCs with a redox-switchable planar defect actuated by a polyferrocenylsilane (PFS) polyelectrolyte multilayer have been prepared.

PFSs are an interesting class of transition metal containing macromolecules with a backbone that consists of alternating ferrocene and organosilane units. They are readily accessible via thermal, anionic, photolytic or transition metal-catalyzed ring-opening polymerization (ROP) of strained, ring tilted silicon-bridged [1]ferrocenophanes and offer

a continuum in degree of oxidation states between their reduced and fully oxidized forms^{3,4}

I incorporated anionic and cationic water soluble PFS polyelectrolytes as redox-active species in LbL self-assembled CPC defect layers (Figure 3.7). The two polyelectrolytes were generously provided by Prof. Ian Manners's group at the University of Toronto. Both polyelectrolytes are synthesized by functionalization of poly(ferrocenylmethylchlorosilane) that is obtained from lithiated ferrocene $\text{Fe}(\eta\text{-C}_5\text{H}_4\text{Li})_2$ and methyltrichlorosilane and subsequent ROP. The anionic PFS polyelectrolyte is prepared by nucleophilic substitution of the chlorine in poly(ferrocenylmethylchlorosilane) with amino-protected $\text{LiC}\equiv\text{CCH}_2\text{N}(\text{SiMe}-\text{CH}_2)_2$. Introduction of charged sulfonate groups is accomplished via ring opening of 1,3-propane sultone by the amino-group under removal of the disilyl protecting group. Analogously, nucleophilic substitution with $\text{LiC}_6\text{H}_4\text{CH}_2\text{NMe}_2$ and subsequent quaternization of the amino-group with dimethylsulfate leads to the corresponding cationic polyelectrolyte.^{5,6}

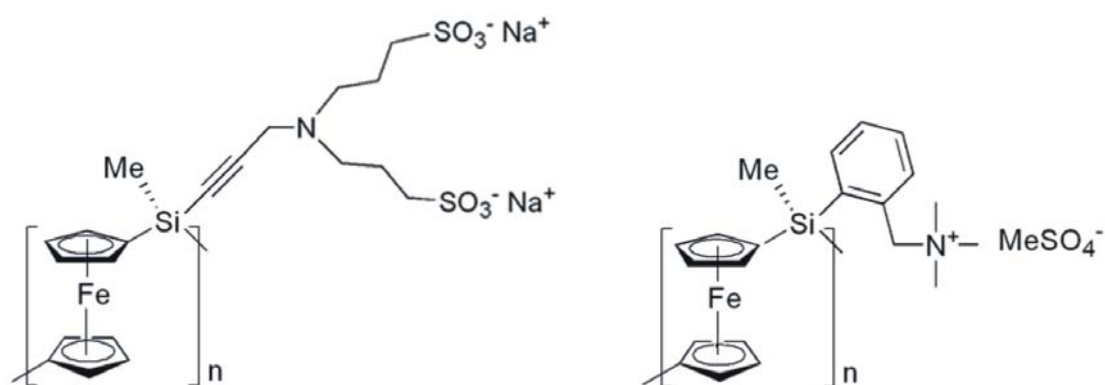


Figure 3.7: Molecular structures of the anionic and cationic PFS polyelectrolytes.

Defect state tuning of PFS defect CPCs (sphere diameter: 280 nm, defect thickness: 60 nm) is achieved by chemically oxidizing and reducing the ferrocene units in the PFS defect layer. Iodine dissolved in hexane (5 mM) was chosen as the oxidizing agent, while reduction was performed with the electron-rich decamethylferrocene in tetrahydrofuran (THF) (9 mM). Compared to the minute amounts of ferrocene units in the nanometer scaled PFS film, the oxidation and reduction agents are used in large excess, ensuring maximum degree of oxidation and complete reduction. The polarity of THF allows the extraction of the decamethylferrocenium iodide by-product out of the polyelectrolyte defect layer, which would otherwise contribute to the sample's optical properties and complicate data analysis. After a first conditioning cycle, completely reversible and

reproducible tuning of the defect wavelength is achieved (Figure 3.8). The stop band edges remain at the same wavelength throughout the cycling, implying that the CPC cladding layers are not influenced by the redox-process.

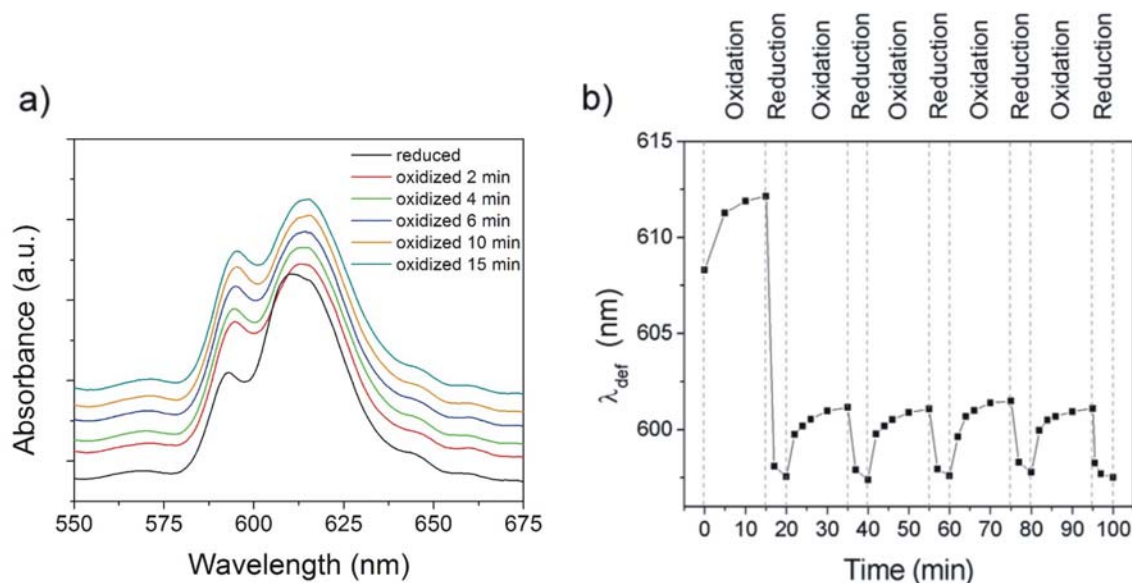


Figure 3.8: a) Transmission spectra of a PFS defect CPC in the reduced state and after different oxidation times (staggered). b) Changes of the wavelength position of the defect state during multiple redox cycles.

Variable angle spectroscopic ellipsometry was used to independently determine the optical properties of a LbL self-assembled and microcontact transfer-printed PFS multilayer, which yielded a thickness of 4.8 nm per PFS bilayer with a refractive index of 1.52 in the wavelength range of the photonic stop gap. Additionally, ellipsometry measurements show a 14% increase in thickness and 6.5% increase in the refractive index of the PFS multilayer film in the fully oxidized state explaining the red shift of the defect wavelength during oxidation. 8% increase in thickness and 3.5% increase in refractive index are already achieved in the semi-oxidized state after 2 min. Upon reduction these properties return to their original states causing a reversible blue shift. The thickness increase in the oxidation process is mostly generated by the incorporation of the Γ / I_3^- counterions into the defect layer. The increased refractive index is a consequence of the higher polarizability of the ferrocenium-iodide repeat units in the oxidized PFS defect layer. Solvent effects on the optical properties of the PFS defect CPCs are negligible since the samples are spectroscopically investigated in a dried state after solvent evaporation.

These results were used to simulate the experimental spectra with the SWA-model. The calculated transmission spectra (dotted lines) of the PFS- silica CPC heterostructure in the reduced and oxidized states are plotted along with the experimental data in Figure 3.9. Experimental positions of the stop band, the defect state and the Fabry-Perot fringes as well as the relative peak intensities are well reproduced by the SWA-simulations. The redox-cycling of the PFS-opal composite CPC could be continuously repeated without degradation in optical and mechanical properties. In addition, the defect wavelength cannot only be switched between two extremes but all intermediate states are individually and controllably accessible depending on the fraction of oxidized PFS repeat units.

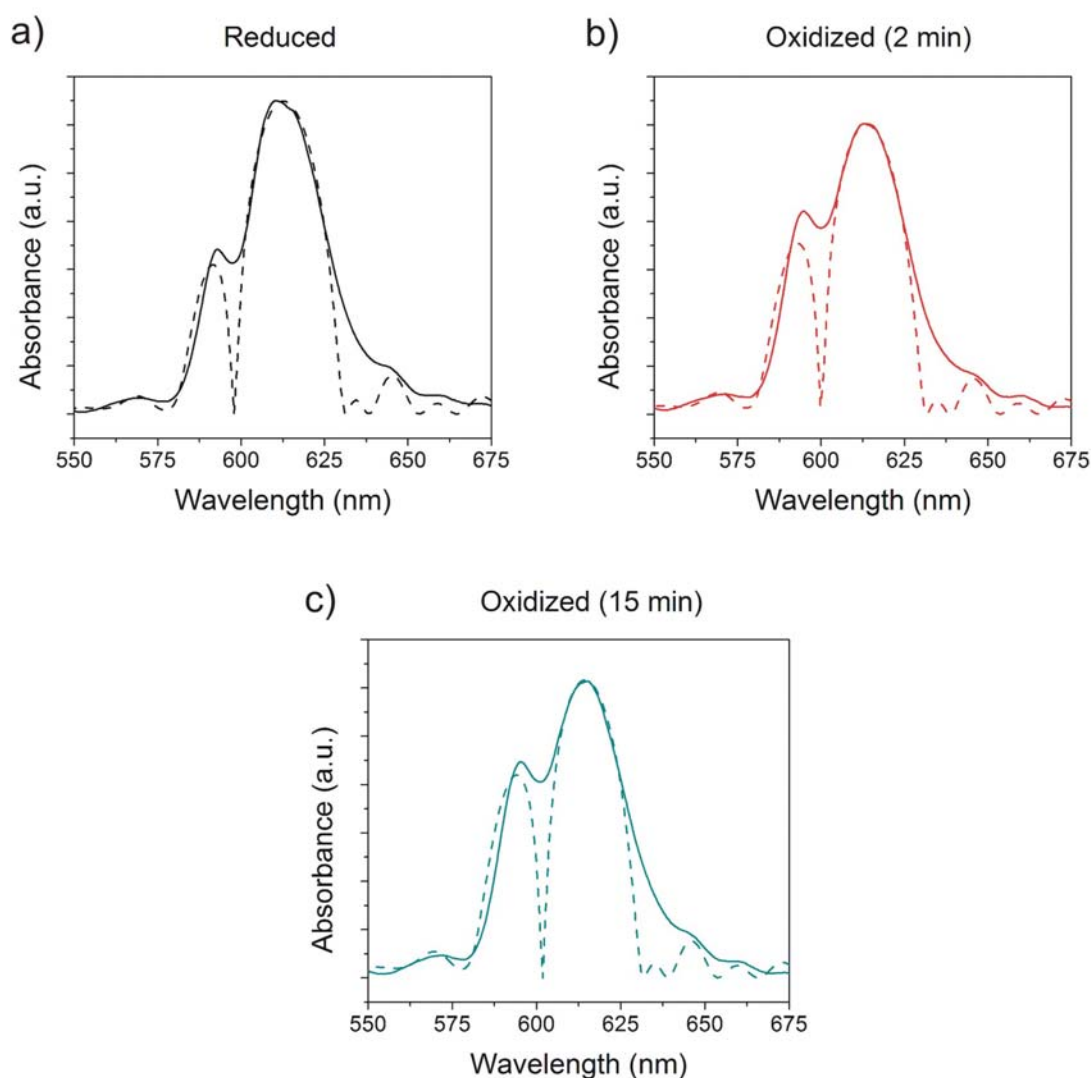


Figure 3.9: Experimental (solid lines) and calculated (dotted lines) transmission spectra (normalized) of a PFS defect CPC in the reduced, semi-oxidized and fully oxidized form.

3.5 Mechanical-Switching

A silica CPC bearing an elastomeric defect layer, allowing for active mechanical tuning of the defect wavelength, was prepared according to the described spin-coating approach (see 2.4.2). I used the thermoplastic elastomer Kraton G[®], a blockcopolymer with "hard" polystyrene domains (network junctions) in a "soft" polyethylene/polybutylene matrix, as defect material (Figure 3.10). Because of physical and not chemical cross-linking, the elastomer can be dissolved in a hydrophobic solvent (e.g. toluene) and processed into a thin film by spin-coating.

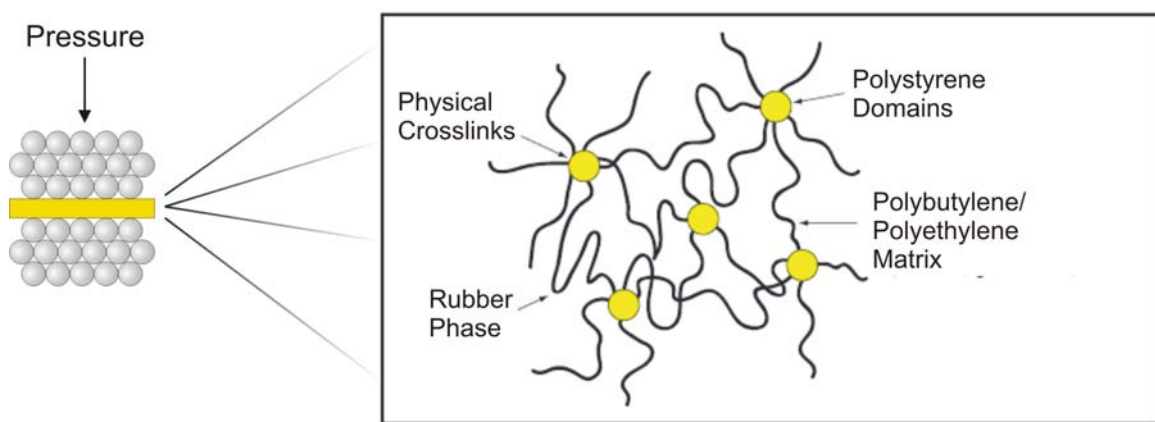


Figure 3.10: Schematic illustration of the physically crosslinked elastomer Kraton G[®] as mechanically tunable CPC defect layer.

The optical spectrum of the elastic defect CPC shows a defect transmission state that can be blue shifted by applying mechanical pressure along the sample's [111]-axis (Figure 3.11a). The sphere diameter of the CPC cladding layers is 280 nm and thickness and refractive index of the defect layer were determined with 365 nm and 1.52, respectively. Hence, we work with a second order defect mode in this case (see section 2.7). Theoretical SWA-simulations of the experimental spectra show that the observed blue shift of the defect wavelength is caused by a 4% and 10% length compression of the defect layer along the [111]-axis (Figure 3.11b-c). With a Young modulus of $2.5 \cdot 10^5$ Pa determined by rheological measurements of Kraton G[®] films, this corresponds to applied pressures on the CPC heterostructure between 0.1 and 0.25 bar.

As already explained in section 3.2, this experiment nicely demonstrates that larger defect wavelength shifts can be observed with higher order defect modes compared to the previous first order defect switching examples with a comparable relative change of the defect layer optical thickness.

The mechanical pressure tuning of Kraton defect CPCs is fully reversible. However, reproducible switching cycles were difficult to run, since pressure was applied manually and not by an automated actuator.

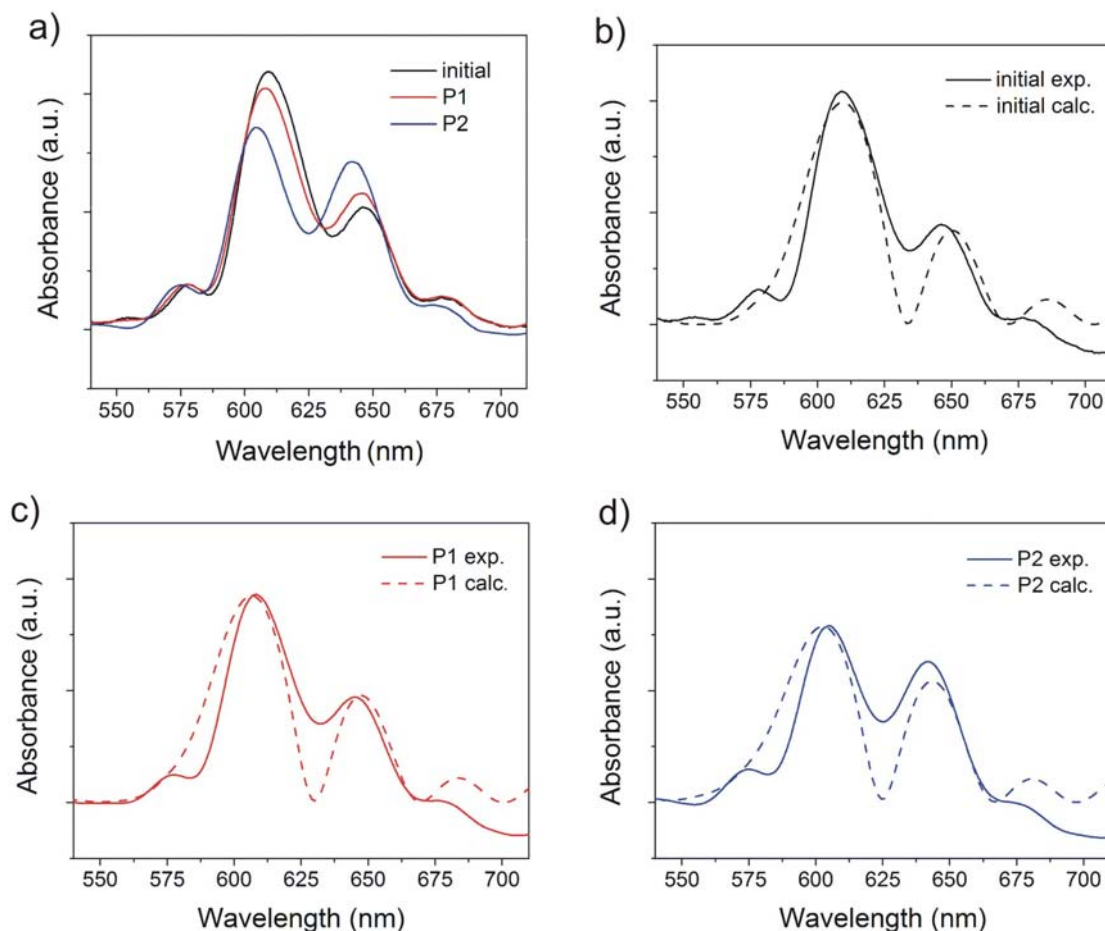


Figure 3.11: a) Transmission spectra of a CPC with spin-coated elastomeric Kraton G[®] defect layer. Initial spectrum and spectra when applying mechanical pressure ($P1 < P2$) perpendicular to the sample surface. b)-d) Experimental (solid lines) and calculated (dotted lines) transmission spectra (normalized) of a Kraton G[®] defect CPC in the initial state and when applying pressure.

3.6 Conclusion

Defect layers with functional groups responsive to light, temperature, redox-cycling and mechanical pressure have been incorporated into CPCs. Precise, reproducible and in most cases reversible tuning of the intragap defect mode is induced by these external stimuli. The switching experiments are supported by independently performed ellipsometry measurements and SWA-calculations. The materials are interesting candidates for tunable CPC based resonator cavities, adjustable ultra-narrow optical filters or color-based sensors.

3.7 References

- (1) Dante, S.; Advincula, R.; Frank, C. W.; Stroeve, P. *Langmuir* **1999**, *15*, 19.
- (2) Tan, C. Z.; Arndt, J. *J. Phys. Chem. Solid.* **2000**, *61*, 1315.
- (3) Manners, I. *Chem. Commun.* **1999**, *10*, 857.
- (4) Tanabe, M.; Manners, I. *J. Am. Chem. Soc.* **2004**, *126*, 11434.
- (5) Wang, Z.; Lough, A.; Manners, I. *Macromolecules* **2002**, *35*, 7669.
- (6) Jäkle, F.; Wang, Z.; Manners, I. *Macromol. Rapid Commun.*, **2000**, *21*, 1291.

Chapter 4

4. Monitoring Biochemistry with Defect Colloidal Photonic Crystals

4.1 Preamble

In Chapter 3, I demonstrated switching of functionalized defects in CPCs by a number of external stimuli. We have seen that the position of the defect wavelength is sensitive to chemical and physical changes in the optical thickness of the active defect layer film. In this chapter, I will show that defect CPCs also present a new class of materials to optically monitor various aspects of chemistry or biochemistry taking place in the functional defect layer, such as (bio-)chemical reactions, conformational changes or the intercalation of molecules.

4.2 Introduction

The need for more accurate, rapid, and powerful chemical sensing methods has been a driving force for the development of new materials and devices. The sensing of biological species and biochemical interactions represents today the major part of these efforts, with important ramifications from disease identification to understanding the basis of organic life. While many important advances have been made in the monitoring of bio-recognition and interaction events at surfaces and in solution, the increasing ability to fabricate complex architectures with nanoscale precision presents unprecedented opportunities for obtaining materials with new and improved properties and designed function.¹⁻³ Biosensors based on optical,⁴⁻⁶ electrochemical,⁷⁻¹² and mass-change readouts¹³⁻¹⁵ have been developed, and major strides have been made concerning array-based analysis and strategies for enhancing sensitivity by amplification. A drawback of many of these methods is the need for sophisticated, complex and expensive instrumentation, especially for most of the available optical readout techniques including fluorescence-based biosensing and surface plasmon resonance (SPR). Especially lacking

is the ability for “on the spot” analysis, where a technician could perform an analysis out of the laboratory setting with a simple probe and detector.

Photonic crystals are arguably a versatile platform for optical sensing and monitoring. CPCs as a subgroup can be self-assembled at low-cost and large scale and the resulting Bragg diffraction peak wavelengths are dependent on the dimensions of the crystal lattice and the refractive index contrast between spheres and voids. The latter property has been used successfully to effect the sensing of a variety of analytes, such as glucose,¹⁶ H⁺ concentration (pH),¹⁷ or metal ions¹⁸ by embedding a crystalline array of spheres into a specially designed electrostatically swellable-shrinkable hydrogel. However, the size of the CPC entrance windows is a limiting factor for the incorporation of (bio-) macromolecules as active matrix inside the CPC voids. Also, the active matrix molecules cannot be incorporated into the voids as such, but require a hydrogel environment to keep up the refractive index contrast and to sufficiently sensitize the Bragg peak for monitoring aspects.

Here, I present CPCs with functional biomolecular planar defects. Using LbL self-assembly, I incorporate biomacromolecules such as proteins and DNA as nanometer thin sheets embedded in a CPC, while maintaining both the bioactivity of these molecules and the optical properties of the CPC. I use the DNA-based planar defect to demonstrate defect mode based optical monitoring of DNA conformational changes such as melting and annealing, as well as its interaction with biologically-relevant molecules such as a chiral anti-cancer drug. Polypeptide defect CPCs are employed to monitor enzyme kinetics and activities, demonstrating the potential of these systems as a novel platform for optical biosensing, bio-diagnostic and biochip applications.

As described in section 2.6, optical characterization requires no sophisticated instrumentation and it is performed with a simple fiber optics spectrometer attached to an optical microscope. The setup allows for real time measurements and a spot size of less than 2 μm in diameter can be probed.

4.3 Monitoring DNA Conformational Changes

Optical monitoring of DNA conformation changes at the denaturation and hybridization point combined with a reversible thermal switching of the defect state position was performed with a calf-thymus DNA/PDAC defect CPC heterostructure (Figure 4.1). Defect thickness and refractive index (in frequency range of stop gap) are determined by ellipsometry with 90 nm and 1.54, respectively. The melting-annealing transition is indispensable to the replication of biological life, and is the central mechanism in forensic DNA amplification. The DNA-CPC composite was kept in a closed box on a thermoelectric Peltier element, and thermally cycled between 40 and 98°C at a rate of 10°C/min. As it was the case in our previous study (see section 3.3), heating the sample leads to a blue shift of the stop band edges due to the evaporation of water adsorbed onto the surface of the CPC cladding layers, resulting in a decreased effective refractive index. Upon cooling the sample, ambient humidity re-adsorbs onto the CPC layers, red shifting the band edges. In terms of the position of the defect transmission window, a starkly contrasting behavior is observed. According to the literature,¹⁹ the melting of the calf-thymus double helix into single-stranded DNA occurs between 85 and 87.5 °C. Correspondingly, in this temperature range we observe a large and abrupt red-shift of the defect wavelength, superimposed onto the slight blue shift due to water loss, allowing us to optically detect the exact DNA denaturation point. Using the SWA-model, we determined that the defect state red shift at the DNA denaturation temperature range is caused by a 10% increase in thickness of the DNA/PDAC defect layer (Figure 4.2). Cooling the sample leads to a blue shift of the defect state due to reformation of the DNA double helix at 20-25 °C below the melting point,²⁰ superimposed onto again the slight red shift due to condensation of the ambient humidity back into the defect layer. The blue shift caused by reformation of double-stranded DNA is not as abrupt as the red shift caused by splitting of the double helix, since the annealing is a kinetically slower process: matching DNA base-pairs have to "find each other" and new hydrogen bonds have to be formed. The thermal tuning of the defect state is reversible, with expected hysteresis, and cyclable. In contrast to the conventional method used for investigating the denaturation temperature of DNA, detecting increased UV absorbance (260 nm) of DNA in solution, this method can optically measure shifts in the photonic defect state through DNA thermal transitions in the solid state. Relying on the ability to vary the thickness of the defect layer as well as the size of the CPC microspheres with nanometer precision, the defect wavelength is not limited to the UV range, but can be situated and detected anywhere in the visible and NIR

frequency range. In addition, minute amounts of DNA (defect thickness ~ 100 nm, ~ 10 ng DNA per mm^2) are involved in the measurement, while still generating precise and reliable results.

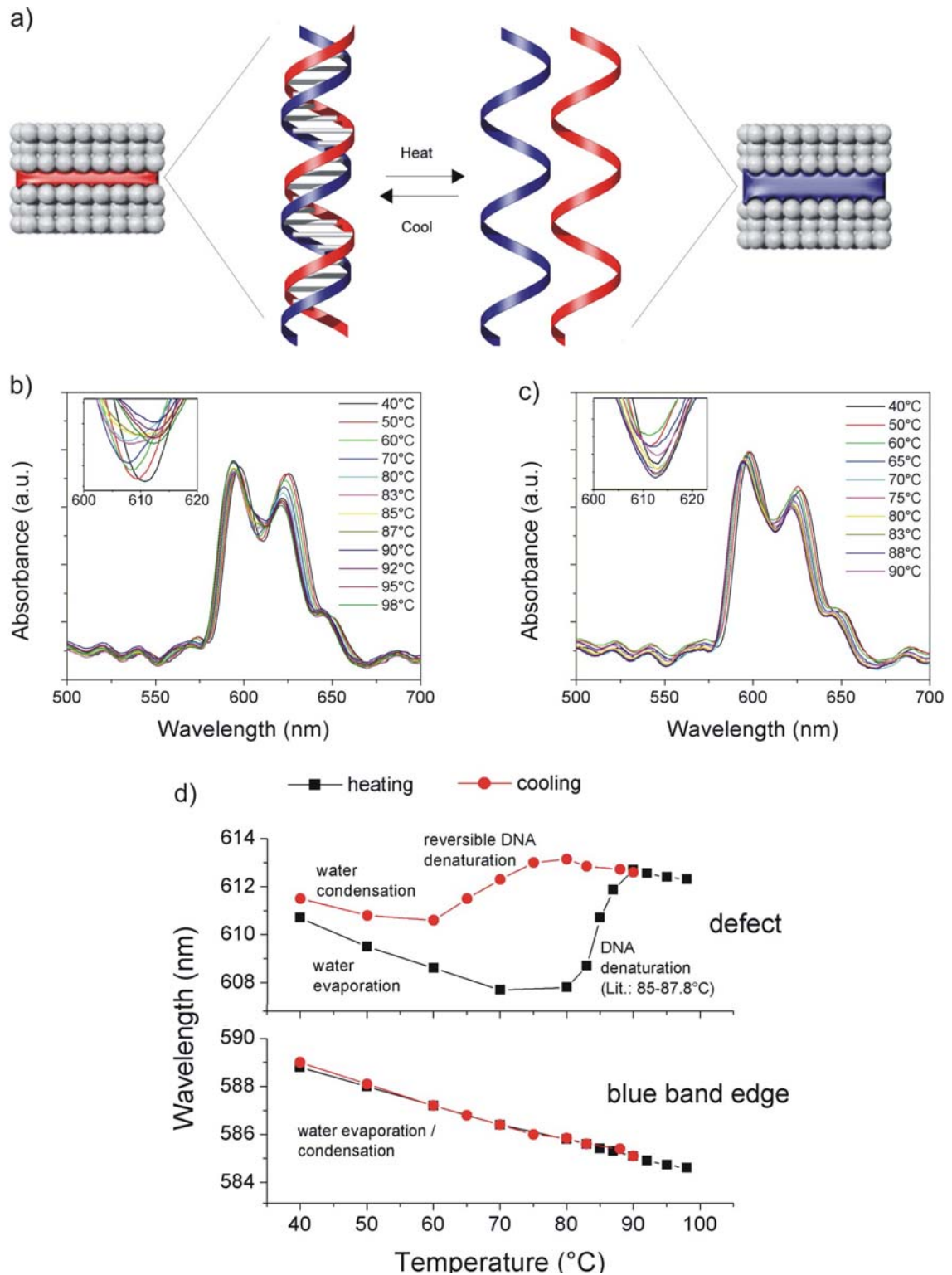


Figure 4.1: Optical detection of DNA melting and annealing. a) Scheme illustrating denaturation and hybridization effects of DNA double strands embedded as a planar defect in a CPC. b,c) Transmission spectra of a calf-thymus DNA defect CPC at temperatures between 40°C and 98 °C upon heating (b) and cooling (c). The insets show a magnification of the defect state position. d) Changes in defect state wavelength and blue band edge during the applied heating and cooling steps.

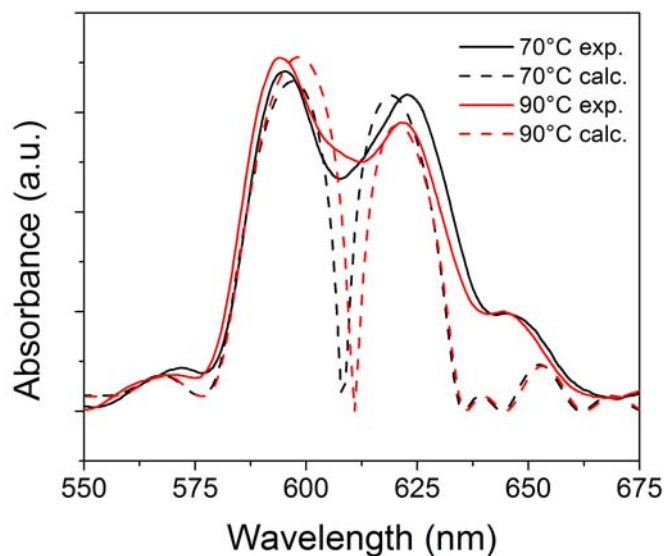


Figure 4.2: Experimental (solid lines) and calculated (dotted lines) transmission spectra (normalized) of a calf-thymus DNA defect CPC below (70°C) and above (90°C) the DNA denaturation temperature.

4.4 Chiral Recognition of an Anti-Cancer Drug

Chiral recognition experiments can also be performed with calf-thymus DNA/PDAC defect CPCs (Figure 4.3). Due to the right-handed helical structure of DNA, chiral molecules and their enantiomers can display vastly different interactions with the double-helix. In particular, the anti-cancer drug daunorubicin and its enantiomer WP900 show different binding affinities to DNA, allowing this interaction to be optically monitored with our photonic crystal detection system. Because of a precise stereochemical fit of the daunosamine sugar moiety of daunorubicin into the minor groove of right-handed DNA, daunorubicin binds to right-handed calf-thymus DNA 24 times more strongly than its enantiomer WP900 under identical conditions.²¹ Exposure of calf-thymus DNA defect CPCs to individual enantiomer solutions having the same concentration, consequently leads to different intercalation amounts of the corresponding enantiomers into the DNA defect layer, and to different changes in the optical properties of the DNA defect CPC. As shown in Figure 4.3b-d, immersing a calf-thymus DNA/PDAC defect CPC sample in a daunorubicin solution (10^{-4} M) for 10 min and drying it afterwards leads to a 13 nm red shift of the defect wavelength whereas the enantiomer solution of WP900 (10^{-4} M) only causes a red shift of the defect position of less than 2 nm. Unambiguous differentiation between the active and inactive enantiomers of this and other existing or potential drugs is consequently possible.

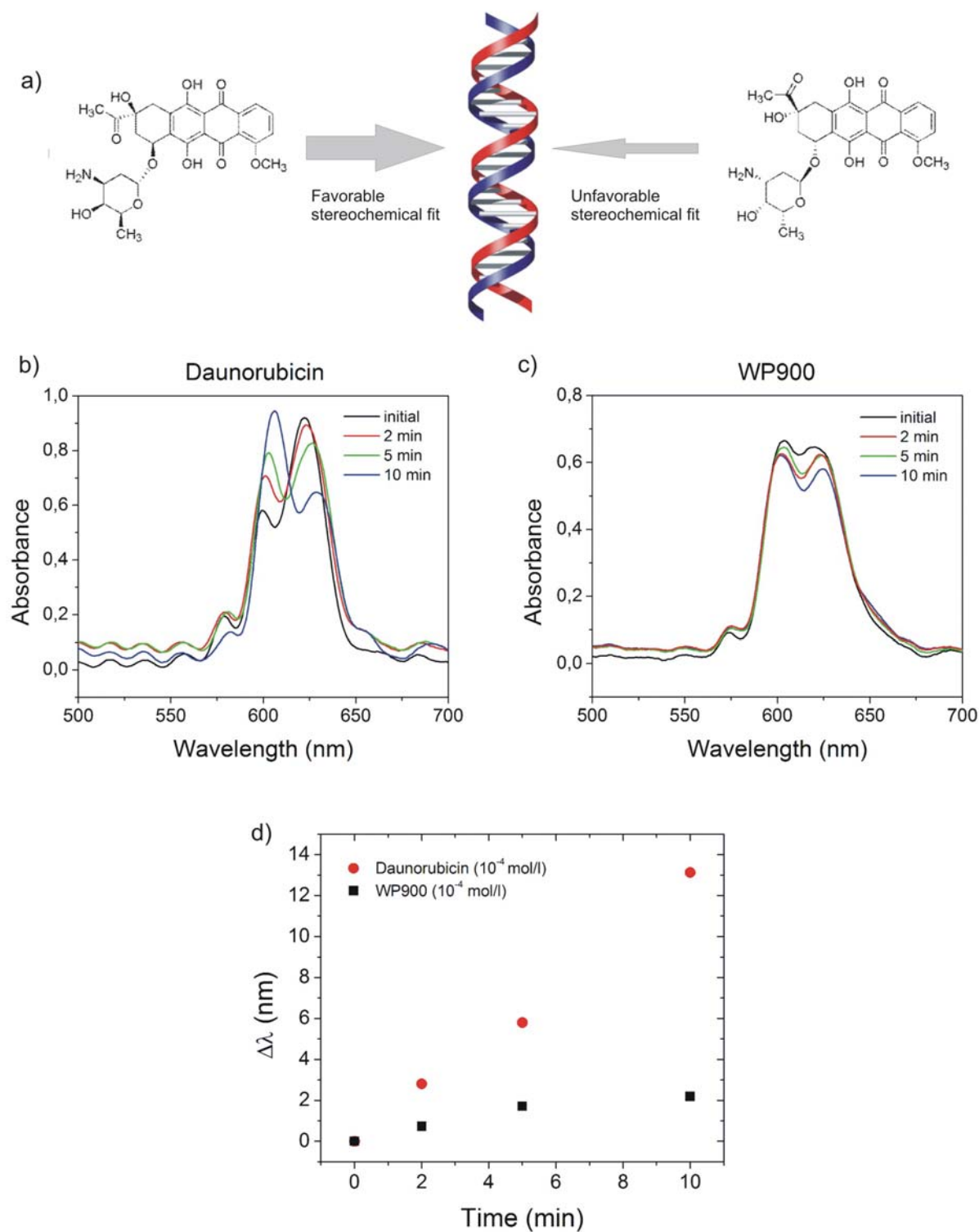


Figure 4.3: Chiral differentiation of an anti-cancer drug using DNA CPC defects. a) Due to the right-handed helical structure of calf-thymus DNA, the chiral anti-cancer drug daunorubicin shows a preferred binding affinity to the DNA double helix compared to the inactive enantiomer WP900. b,c) Transmission spectra of calf thymus DNA defect CPCs recorded after different exposure times to daunorubicin (b) and WP900 (c) dissolved in water (10^{-4} M). d) Changes of the defect state wavelength of DNA defect CPCs depending on the exposure times to the corresponding daunorubicin and WP900 solutions.

The intercalation behavior is further supported by independently performed ellipsometric measurements and SWA-simulations of the experimental spectra (Figure 4.4). Immersing a DNA/PDAC film in a 10^{-4} M solution of the anti-cancer drug daunorubicin leads to a 25-30% increase in thickness and a 1% increase in refractive index in the wavelength region of the Bragg-peak, this being responsible for the pronounced defect wavelength red-shift of the DNA/PDAC heterostructure. However, exposing a DNA/PDAC film to a WP900 solution of the same concentration for the same time causes a thickness increase of less than 3% and no detectable change in the refractive index, entirely consistent with the small shift of the defect wavelength in the corresponding CPC heterostructure.

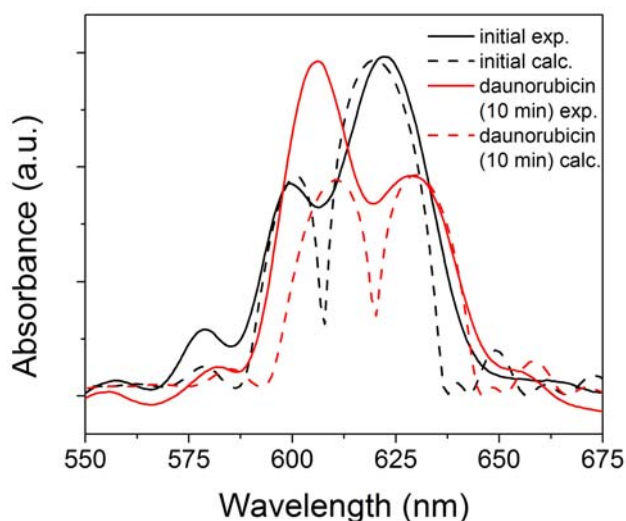


Figure 4.4: Experimental (solid lines) and calculated (dotted lines) transmission spectra (normalized) of a calf-thymus DNA defect CPC in the initial state and after 10 min immersion in a 10^{-4} M solution of the anti-cancer drug daunorubicin.

Taking into account that we can easily probe a spot size of $2\ \mu\text{m}$ in diameter by microspectroscopy and that droplets of less than 10 pL can be ejected with standard inkjet printers, less than 1 fmol of the anti-cancer drug and its enantiomer is necessary to perform the described chiral recognition experiments using DNA defect CPCs. In addition these considerations show, that the developed bio-defect CPCs are highly suitable for array-based analysis and biochip applications. Since CPCs can be used for chromatography,²² the presented bio-defect CPCs are also potential candidates for combining separation and biomonitoring in a single microstructured sample.

4.5 Monitoring Enzyme Reactions

Poly-L-lysine (PLL)/ poly-L-glutamic acid (PLGA) defect CPCs were prepared and exposed to trypsin to optically monitor the enzymatic degradation of the embedded polypeptide film.

Trypsin is known as a serine protease that predominantly cleaves proteins at the C-terminal side of the amino acids lysine and arginine. Serine (Ser 195), histidine (His 57), and aspartate (Asp 102) (Figure 4.5a), are the three key residues, the so-called catalytic triad, catalysing the hydrolysis by preferential binding and by providing suitable reactive groups near the peptide bond to be cleaved. The aspartate residue in the active site of trypsin interacts with the positive charge on lysine or arginine and is thus responsible for the specificity of the enzyme. With assistance from histidine (proton transfer), the side chain oxygen of serine cleaves the amide bond by a nucleophilic attack on the carbonyl carbon. A further nucleophilic attack of water on the acyl-enzyme intermediate follows and the enzyme is released in the initial form (Figure 4.5b).²³

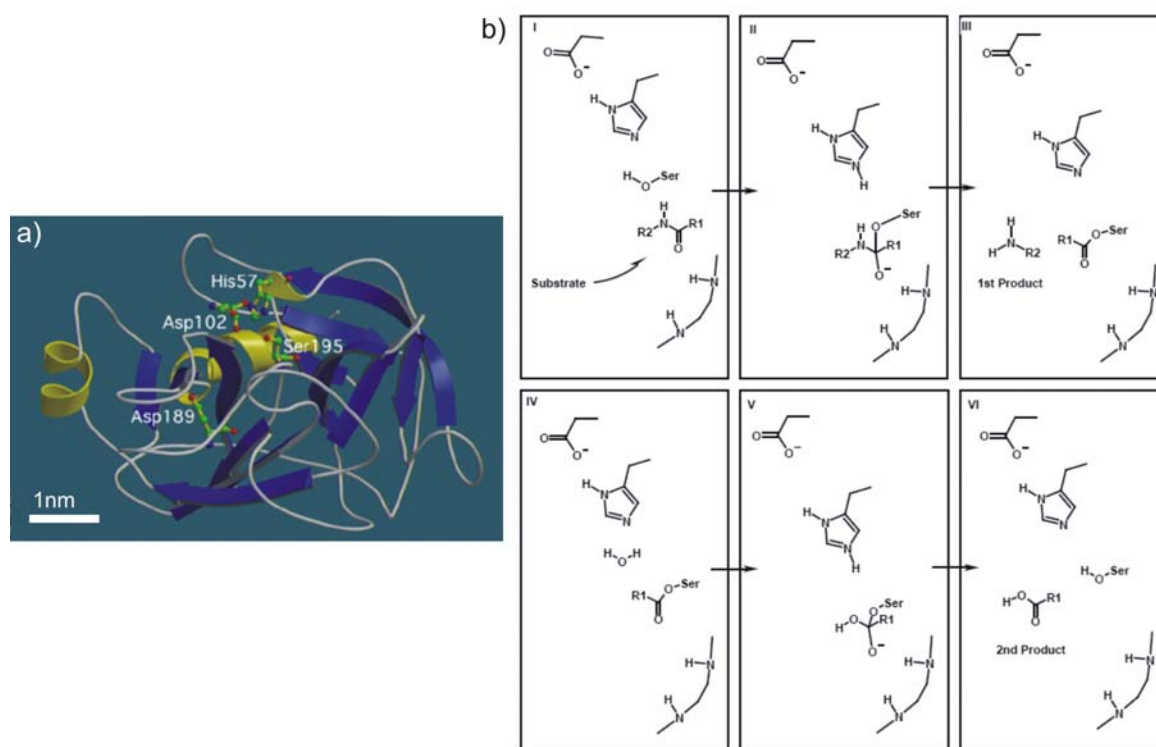


Figure 4.5: a) Molecular model of bovine trypsin showing the key residues in the active site.²⁴ b) Mechanism of the trypsin catalyzed peptide cleavage.²⁵

Trypsin in Ammoniumbicarbonate

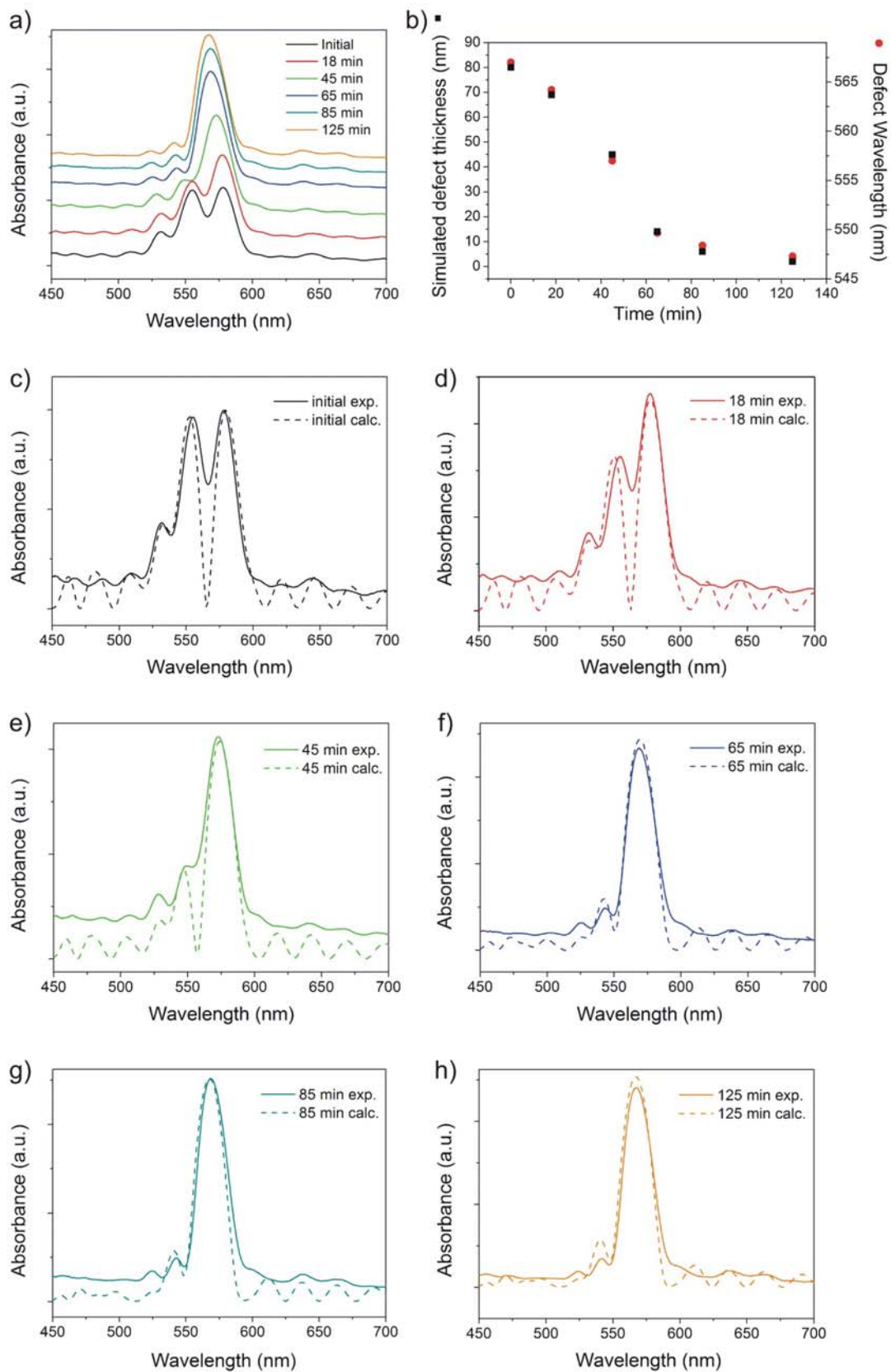


Figure 4.6: PLL/ PLGA defect CPC exposed to trypsin (680 BAEE units/mg) in ammonium bicarbonate solution (10mM). a) Transmission spectra (staggered) of a PLL/ PLGA defect CPC recorded after different exposure times. b) Defect state wavelength and simulated defect thickness depending on the exposure time. c)-h) Simulated transmission spectra (dotted lines) along with the corresponding experimental spectra (solid lines) plotted in a).

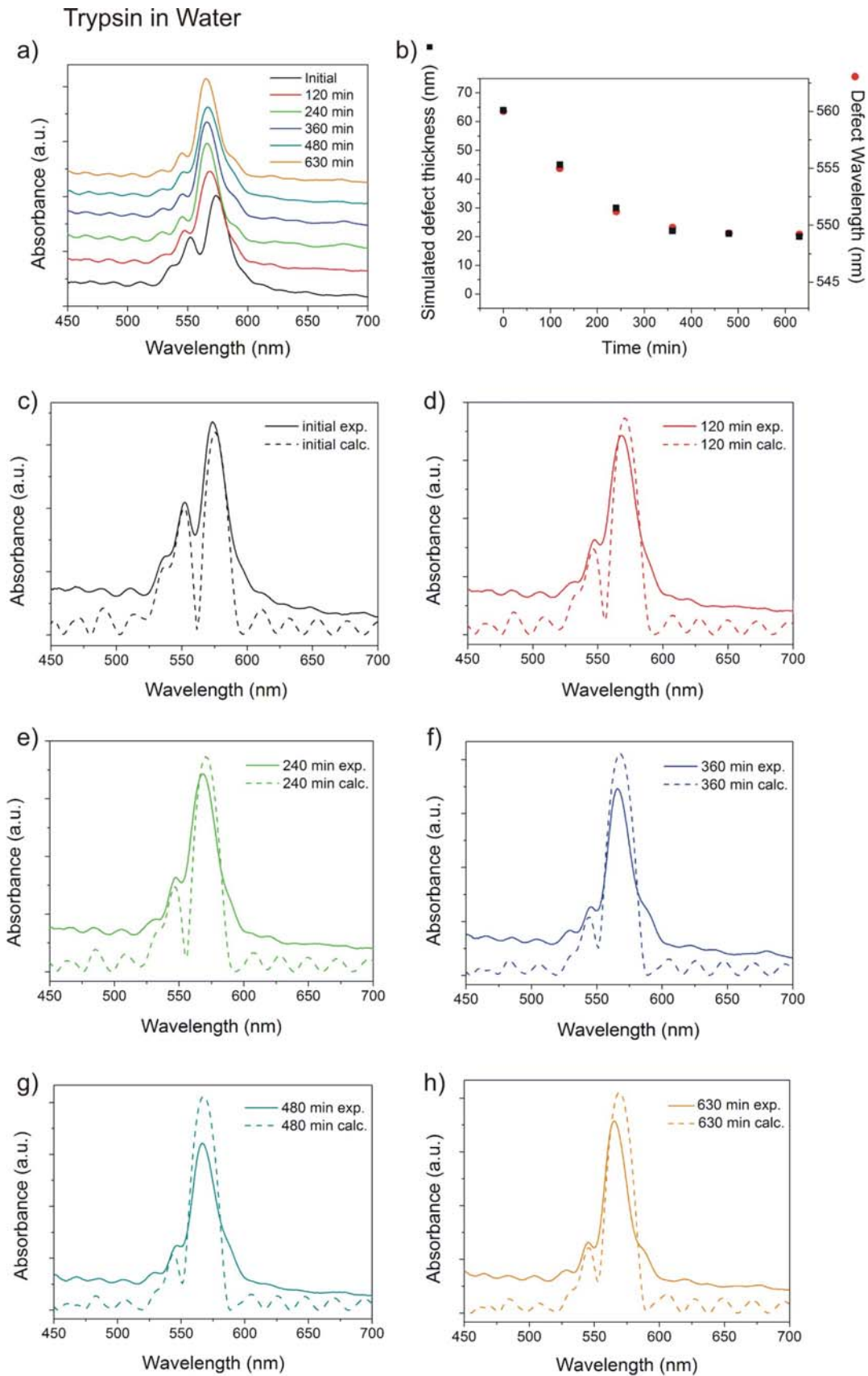


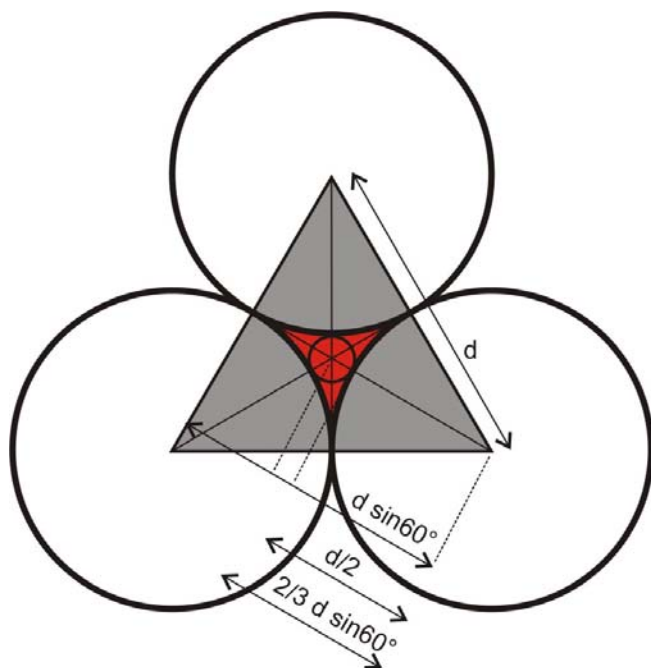
Figure 4.7: PLL/ PLGA defect CPC exposed to trypsin (680 BAEE units/mg) in deionized water. a) Transmission spectra (staggered) of a PLL/ PLGA defect CPC recorded after different exposure times. b) Defect state wavelength and simulated defect thickness depending on the exposure time. c)-h) Simulated transmission spectra (dotted lines) along with the corresponding experimental spectra (solid lines) plotted in a).

PLL/ PLGA defect CPCs were immersed in solutions of trypsin (680 BAEE units/mg)²⁶ in ammonium bicarbonate (10 mM) and in deionized water, respectively. The ammonium bicarbonate solution with pH 8.2 provides optimal cleaving conditions, whereas trypsin in water is expected to be less reactive.²⁷ The samples are kept at 37°C ambient temperature while exposed to the enzyme solutions and are spectroscopically investigated in the dried state at certain time intervals.

The optical spectra are shown in Figures 4.6a and 4.7a. The change of defect wavelength as well as the calculated defect thickness dependent on the exposure time is plotted in Figures 4.6b and 4.7b. The calculated defect layer thickness results from SWA-simulations of the experimental spectra (Figures 4.6c-h and 4.7c-h). For this purpose, an ellipsometrically determined PLL/ PLGA multilayer refractive index of 1.55 (in the stop gap frequency range), that remains constant during the erosion process, was used as input. In case of trypsin in ammonium bicarbonate solution, the initial defect state undergoes a rapid blue shift and disappears after 2 hours. The defect shift is in agreement with a degradation of the polypeptide film of more than 95%. Regarding trypsin in water, the defect state blue shift is decelerated and a stationary state is reached after 6 hours. This corresponds to only a 68% decrease in thickness of the embedded PLL/ PLGA film. The stop band edges remain constant, implying that the CPC cladding layers are not influenced by the trypsin catalysed polypeptide hydrolysis. The different degradation rates are consistent with the pH dependent trypsin activities reported in literature.²⁷ Also, we are confronted with the autolysis of trypsin during longer reaction times. This changes trypsin activities additionally and explains the stopped hydrolysis of the polypeptide defect after exposure to trypsin in water for 6 hours at 37°C.

Despite the predominant cleavage of PLL catalyzed by trypsin, the results show that the entire PLL/ PLGA multilayer is affected by the enzymatic degradation: oligo-lysine fragments or single lysine units are formed and rinsed out of the multilayer. The remaining negatively charged PLGA chains are not electrostatically attracted and the multilayer stack collapses. In addition, the experiments demonstrate that the defect layer is not only accessible by small molecules like iodine or the anti-cancer drug daunorubicin (see sections 3.4 and 4.4), but also globular molecules like enzymes can enter the porous CPC if their size does not exceed the area of the CPC voids. In this case, the CPC cladding layers consist of colloids with a diameter of 255 nm and the CPC interstitial area is calculated with $2.6 \cdot 10^3 \text{ nm}^2$. The largest spherically shaped object that can pass through this area possesses a diameter of about 40 nm (Figure 4.8). If we assume the shape of

trypsin as a "hard sphere" with a diameter of about 5 nm (Figure 4.1a), we understand that the enzyme can readily pass the CPC entrance windows and diffuse throughout the crystal structure.



interstitial sphere radius: $2/3 d \sin 60^\circ - d/2$

interstitial area: $1/2 d^2 \sin 60^\circ - 3 (\pi (d/2)^2/6)$

Figure 4.8: Schematic representation of a cross-section cut through the centers of the spheres in a [111] triangular stacking. Simple euclidian geometry allows for calculation of the interstitial area (red shaded) as well as for determination of the maximum radius of a spherically shaped object that can pass through a CPC void.

4.6 Conclusion

In summary, CPCs with integrated biologically active defect structures have been prepared for the first time. Calf-thymus DNA defect CPCs enabled optical monitoring of conformation changes at the DNA denaturation and hybridization point and were used for unambiguous chiral recognition of enantiomer pairs. Trypsin catalyzed pH dependent digestion of polypeptides thin films has been monitored with PLL/ PLGA defect CPCs. This newfound capability for optically monitoring biochemistry with defect CPCs, bodes well for the development of a new generation of simple on-the-spot readout biosensors and biochips for monitoring a wide range of bio-events from DNA mutation, testing the potential activity and toxicity of drugs to elucidating enzyme mechanisms.

4.7 References

- (1) Drummond, T. G.; Hill, M. G.; Barton, J. K. *Nat. Biotechnol.* **2003**, *21*, 1192.
- (2) Fortina, P.; Kricka, L. J.; Surrey, S.; Grodzinski, P. *Trends Biotechnol.* **2005**, *23*, 168.
- (3) Rosi, N. L.; Mirkin, C. A. *Chem. Rev.* **2005**, *105*, 1547.
- (4) Epstein, J. R.; Brian, I.; Walt, D. R. *Anal. Chim. Acta* **2002**, *469*, 3.
- (5) McDonnell, J. M. *Curr. Opin. Chem. Biol.* **5**, 572.
- (6) Storhoff, J. J.; Elghanian, R.; Mucic, R. C.; Mirkin, C. A.; Letsinger, R. I. *J. Am. Chem. Soc.* **1998**, *120*, 1959.
- (7) Palecek, E. *Nature* **1960**, *188*, 656.
- (8) Palecek, E. *Anal. Biochem.* **1988**, *170*, 421.
- (9) Yang, I. V.; Thorp, H. H. *Anal. Chem.* **2001**, *73*, 5316.
- (10) Palacek, E.; Fojta, M.; Jelen, F. *Bioelectrochemistry* **2002**, *56*, 85.
- (11) Boon, E. M.; Barton, J. K. *Curr. Opin. Struct. Biol.* **2002**, *12*, 320.
- (12) Ozsoz, M.; Erdem, A.; Kara, P.; Kerman, K.; Ozkan, D. *Electroanalysis* **2003**, *15*, 613.
- (13) Wang, J.; Jiang, M.; Palecek, E. *Bioelectrochem. Bioenergetics* **1999**, *4*, 477.
- (14) Patolsky, F.; Lichtenstein, A.; Willner, I. *J. Am. Soc.* **2001**, *123*, 5194.
- (15) Fritz, J.; Baller, M. K.; Lang, H. P.; Rothuizen, H.; Vettiger, P.; Meyer, E.; Güntherodt, H. J.; Gerber, C.; Gimzewski, J. K. *Science* **2000**, *288*, 316.
- (16) Alexeev, V.; Goponenko, A.; Sharma, A.; Lednev, L. K.; Wilcox, C.; Finegold, D.; Asher, S. A. *J. Am. Chem. Soc.* **2003**, *125*, 3322.
- (17) Lee, K.; Asher, S. A. *J. Am. Chem. Soc.* **2000**, *122*, 9534.
- (18) Asher, S. A.; Sharma, A. C.; Goponenko, A. V.; Ward, M. M. *Anal. Chem.* **2003**, *75*, 1676.
- (19) Long, E. C.; Varian ApprUV Notes, "Aspects of Thermal Analysis (Tm) of DNA on the Varian Cary 219".
- (20) Freifelder, D. *Molecular Biology*, Jones and Bartlett, Publishers Inc., Boston, 1986.
- (21) Qu, X.; Trent, J. O.; Fokt, I.; Priebe, W.; Chaires, J. B. *PNAS* **2000**, *97*, 12032.
- (22) Kamp, U.; Kitaev, V.; v. Freymann, G.; Ozin, G. A.; Mabury, S. A. *Adv. Mater.* **2005**, *17*, 438.
- (23) Campbell, N.; Reece, J.; Simon, E. *Essential biology with physiology*, Pearson Cummings, San Francisco, 2006.

- (24) <http://delphi.phys.univ-tours.fr/Prolysis/images.html>.
- (25) <http://www.andrew.cmu.edu/user/rule/bc/Lec/Lec16/lec16.PDF>.
- (26) One BAEE unit is defined as the amount of trypsin required to catalyze a change in absorbance of 153 nm light of a N α -benzoyl-L-arginine ethyl ester (BAEE) substrate by 0.001 per minute at 25°C, pH 7.6 in a reaction volume of 3.2 ml (Sigma-Aldrich product information).
- (27) Miller, W. G. *J. Am. Chem. Soc.* **1964**, 86, 3918.

Chapter 5

5. Light Emitters in Defect Colloidal Photonic Crystals

5.1 Preamble

In the previous two chapters, I demonstrated switching and monitoring with functional defect CPCs. Here, I incorporate light emitters, such as fluorescent dyes and quantum dots, into defect CPC structures and investigate the influence of photonic stop band and (tunable) defect state on the photoluminescence.

5.2 Introduction

Fluorophores (dyes, semiconductor quantum dots, rare earth ions) have been integrated into various types of plain CPCs and inverted CPCs. Suppression of emission at wavelengths of the photonic band gap or stop band and in some cases enhancement at the band edges (due to the high DOS) has been observed.¹⁻²³ In this chapter, I present the preparation of designed defect CPCs and tunable defect CPCs with embedded light emitters for the first time. Different fluorescent dyes and semiconductor quantum dots emitting in the visible and NIR frequency range are incorporated either into the entire defect CPC structure or exclusively into the defect layer. The materials are chosen such that photoluminescence (PL) spectrum and photonic Bragg-peak including defect transmission state overlap. The modifying influence of stop band and intragap transmission state on the PL spectra is analyzed.

5.3 Luminescent Defect Colloidal Photonic Crystals

Defect CPCs with fluorophores distributed among the entire architecture were prepared by infiltrating fluorescent dyes or quantum dots from solution/dispersion into the corresponding non-luminescent defect CPC structures.

5.3.1 Rhodamine 6G Doped Defect CPC

In experiment 1, a PAZO/PDAC defect silica CPC (sphere diameter: 280 nm, defect thickness: 100 nm) doped with the fluorescent dye Rhodamine 6G (R6G) was prepared. For this purpose, the sample is immersed in a saturated aqueous solution of R6G followed by subsequent drying. Electrostatic interactions between the positively charged dye and the negative surface charge of the silica colloids as well as the charged polyelectrolyte multilayer are assumed to support the adsorption of the dye.

Optical characterization was performed with an optical bench setup (University of Freiburg, Prof. G. Strobl's group) that allows for successive reflection/ transmission and photoluminescence measurements at the same sample spot (Figure 5.1). As in previous studies of this work, spectra were taken at normal incidence along the CPC's [111]-axis.

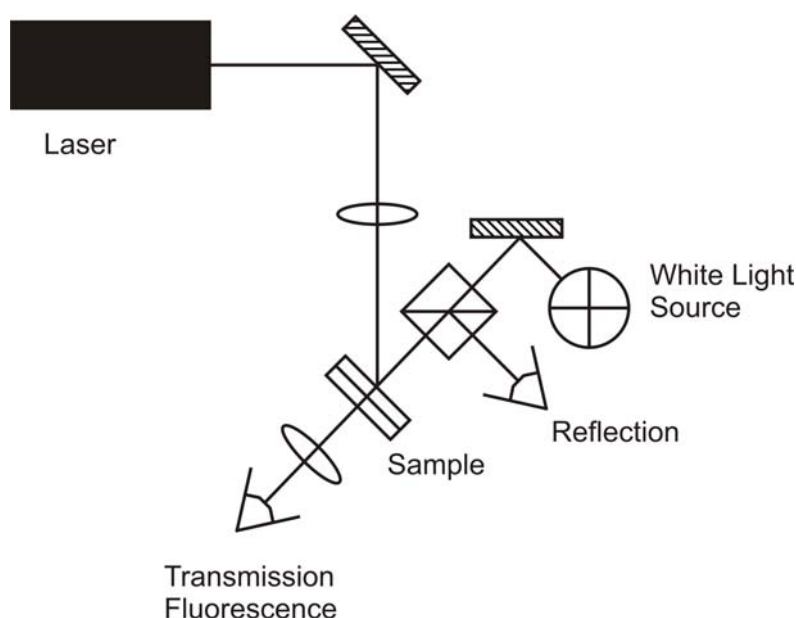


Figure 5.1: Sketch of the optical setup allowing for probing reflection/ transmission and photoluminescence at the same sample spot.

The reflection spectrum of the defect CPC as well as the PL spectra of R6G on amorphous silica and of R6G infiltrated in the defect CPC are plotted in Figure 5.2. The PL spectrum of R6G on amorphous silica is used as reference: The emission is not affected by a photonic band structure, and the substrate material the dye is adsorbed on is comparable to that of a silica CPC. Excitation is performed at 532 nm with a frequency-doubled cw Nd:YAG laser (spot-diameter of the focused beam $\sim 20 \mu\text{m}$) and PL is detected in transmission with a fiber optics spectrometer operating in the visible. If we compare the emission of R6G in the defect CPC (Figure 5.2c) to the reference (Figure 5.2a), we

observe a clear PL modification caused by the photonic bandstructure. Comparing Figure 5.2b and 5.2c, we can obviously notice the "fingerprint" of Bragg peak and intragap defect state imposed on the PL spectrum of the embedded dye. However, exact quantitative comparisons of the modified PL spectrum and the reference were difficult to perform due to inhomogeneities in the dye distributions within the samples and detection of scattered excitation light. Normalization and approximate fitting of the two spectra at wavelengths out of the Bragg-peak region result in a maximum suppression of ~55% by the photonic stop band and unaffected emission at the position of the defect wavelength.

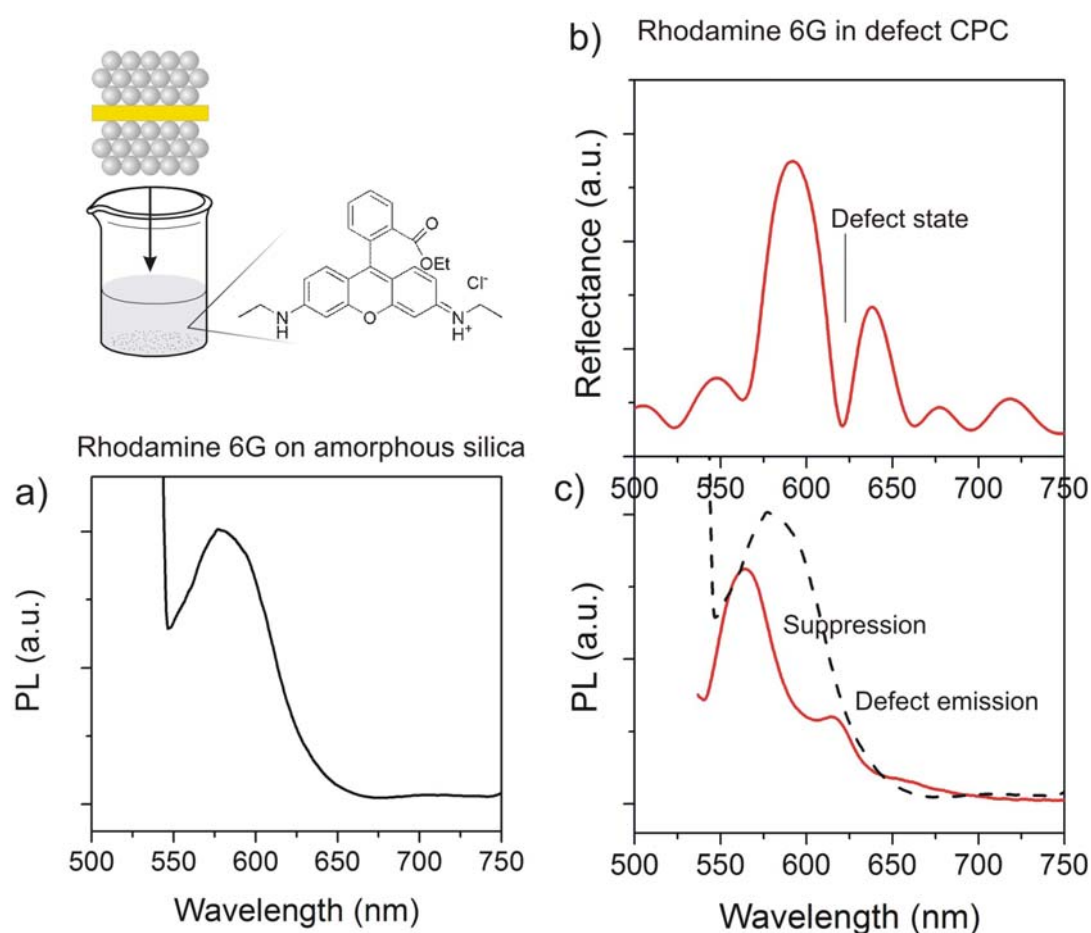


Figure 5.2: Defect CPC doped with R6G. a) PL spectrum of R6G on amorphous non-photonic silica (reference). Excitation wavelength: 532 nm. b) Defect CPC spectrum in reflection. c) PL spectrum of R6G incorporated in defect CPC (red solid line) and PL spectrum of normalized reference (black dashed line). Excitation wavelength: 532 nm.

5.3.2 PbS Quantum Dot Doped Defect CPC and Thermal Switching

In experiment 2, a PAZO/PDAC defect CPC was infiltrated with PbS quantum dots (QDs) from the corresponding hexane dispersion.

The QDs were synthesized separately by a hot-injection method, with lead chloride and elemental sulfur as reagents and oleylamine as coordinating solvent.²⁴ Unlike the fluorescent dye used in the previous study, PbS QDs show fluorescence and first absorption maximum in the NIR, but can still be excited at higher absorption bands in the entire visible frequency range. The emission wavelengths are dependent on the size of the synthesized QDs (quantum size effect). The PbS QD batch used in this experiment was generously provided by L. Cademartiri (University of Toronto) and shows a PL maximum at around 1400 nm (Figure 5.4a).

In order to achieve overlapping of PL spectrum and photonic Bragg-peak plus defect state, the QD doped defect CPC consists of 625 nm silica spheres and possesses a first order multilayer defect of 180 nm. An elegant and time saving method for the preparation of thick polyelectrolyte multilayer defects is repeated microcontact transfer printing of several thinner LbL self-assembled multilayer stacks on PDMS that can be previously cut from a single larger area sample prepared in one step (see section 2.4.1). In this case, I transfer print twice 20 bilayers of PAZO/PDAC on a "necked" silica CPC. The corresponding NIR spectra at different preparation steps are shown in Figure 5.3 and are nicely consistent with previous observations in the visible range discussed in section 2.6: Mechanical stabilization of the bottom-CPC by silica CVD-necking leads to a slight red shift and decreased intensity of the Bragg diffraction peak. The 20 bilayer surface defect causes a further decrease and red shift accompanied by the formation of a shoulder on the longer wavelength side. Transferring another 20 bilayers shows the beginning of the "periodic cycling" theoretically simulated and described in 2.6 as well. A blue shift of the peak is observed, the intensity is growing and a shoulder on the shorter wavelength side appears. Crystallization of the top-CPC finally leads to the expected intragap transmission state in the Bragg-peak (Figure 5.4b).

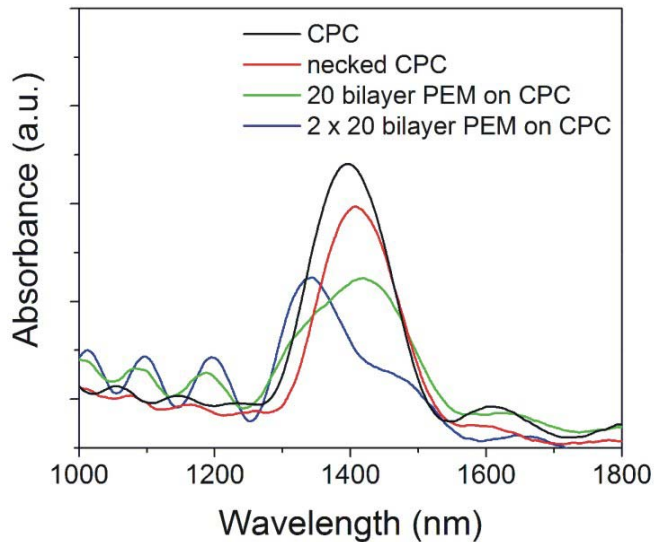


Figure 5.3: Optical transmission spectra of a CPC with 40 bilayer polyelectrolyte multilayer (PEM) surface defect at different preparation steps .

Optical characterization of the PbS QD doped defect CPC was performed with a setup at the University of Toronto similar to that described in 5.3.1. In this case, excitation was carried out with a cw Ar-ion laser at 514 nm and a detector operating in the NIR frequency range was available. In addition, the setup allowed for integration of a heating and cooling stage and a combination of modified PL and temperature switching (see section 3.3) was possible.

Figure 5.4b shows the optical reflection spectra of the QD doped defect CPC at 10°C and 90°C. The PL spectra of PbS QDs on amorphous silica (reference) and integrated within the defect CPC structure are plotted in Figures 5.4a and 5.4c. The modifying influence of the photonic band structure with defect state on the QD PL spectrum is clearly visible: Suppression of PL (~10-55%) at wavelengths of the Bragg-peak and (presumably) unaffected emission at the defect wavelength can be observed. Exact quantitative comparisons of modified PL spectra and reference underly the same challenges already discussed in 5.3.1.

In addition, the position of defect mode and Bragg peak of the QD doped defect CPC could be reversibly switched by temperature. Hence, the QD luminescence spectrum modified by the photonic bandstructure undergoes reversible shifts as well. The sample was kept in a closed box on a thermoelectric Peltier element, and thermally cycled between 10 and 90°C at a rate of 10°C/min. Analogously to our previously performed studies (section 3.3), heating the sample leads to a blue shift of defect wavelength and stopband edges and cooling induces a reversible blue shift. After some "conditioning"

cycles, completely reversible switching of the defect wavelength can be observed (Figure 5.4d).

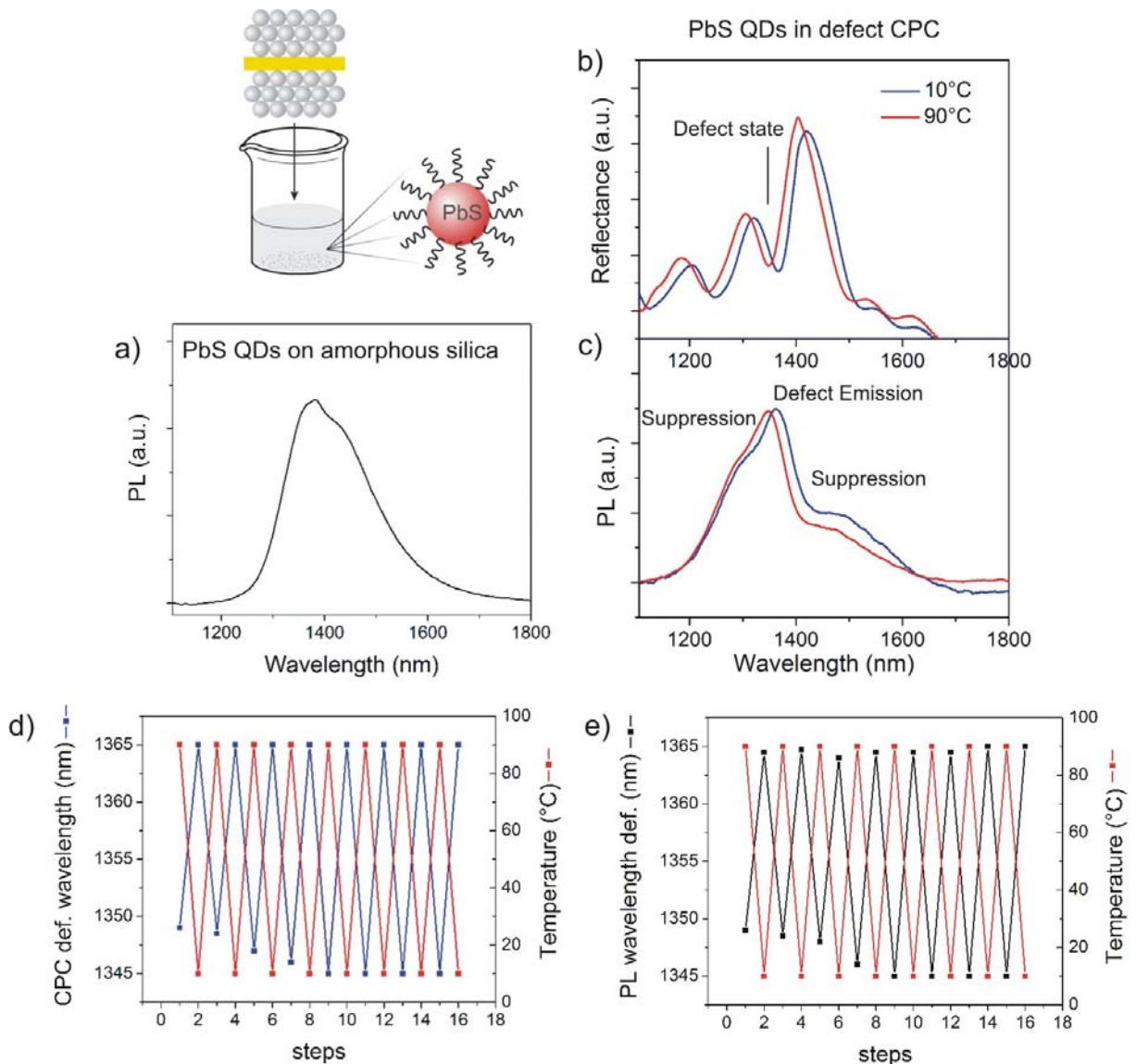


Figure 5.4: Defect CPC doped with PbS QDs. a) PL spectrum of PbS QDs on amorphous silica (reference). Excitation wavelength: 514 nm. b) Defect CPC spectra in reflection at 10 and 90°C. c) PL spectrum of PbS QDs incorporated in defect CPC at 10 and 90°C. Excitation wavelength: 514 nm. d) Dependence of defect state wavelength on temperature during heating and cooling cycles. e) Dependence of defect emission wavelength on temperature during the applied heating and cooling steps.

In agreement with previous assumptions, the temperature induced shift can be simulated taking into account a 10 and 20 vol% water loading in the CPC voids and defect state, respectively, at 10°C, and a near-zero humidity level at 90°C (Figure 5.5) The tuning of defect transmission window and Bragg peak is exactly reflected by the PL spectrum of the PbS QDs embedded in the defect CPC. Raising the temperature from 10 to 90°C blueshifts the defect emission as well as the regions in the PL spectrum affected by the

Bragg-peak (Figure 5.4c). When cooling the QD doped defect CPC down to 10°C, the initial PL spectrum is detected again. During further temperature cycles, the PL maximum at the defect transmission window undergoes precisely the same shift that we observed for the position of the defect state when probing the sample with white light (Figure 5.4e). The PL spectrum of PbS QDs on amorphous silica is unaffected by the performed temperature changes. Consequently, shifts in the modified PL spectrum of PbS QDs embedded in the defect CPC are exclusively due to changes in the photonic bandstructure.

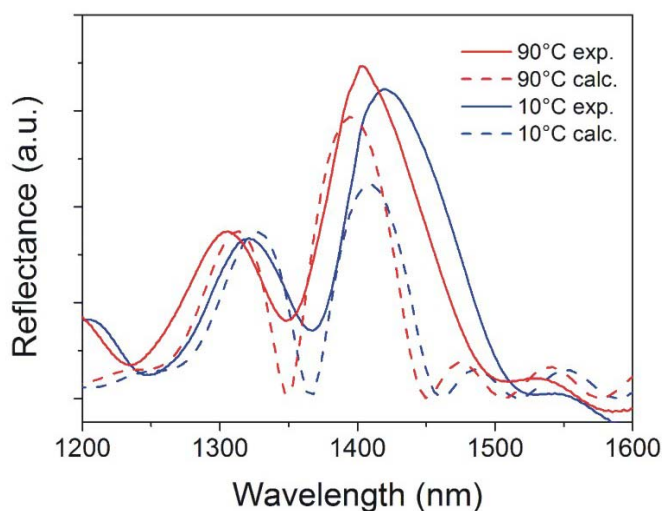


Figure 5.5: Experimental (solid lines) and simulated (dotted lines) transmission spectra of a PAZO/PDAC defect CPC at 10°C and 90°C.

5.4 Colloidal Photonic Crystals with Exclusively Luminescent Defect Layer

Using the spin-coating defect preparation method (section 2.4.2), it was possible to synthesize doped polymer defect CPCs, with a fluorescent dye located exclusively in the defect layer. I used PMMA as defect material, 4-(dicyanomethylene)-2-methyl-6-(p-dimethyl-aminostyryl)-4H-pyran (DCM) as hydrophobic fluorescent dye and toluene as suitable spin-coating solvent for PMMA.²⁵ In contrast, the LbL transfer printing method cannot localize charged fluorescent dyes such as rhodamine within the defect layer, since the dye molecules, just bearing a single electrostatically adhesive charge, are washed out of the LbL film during the LbL-rinsing steps or during evaporation induced self-assembly of the top-CPC.

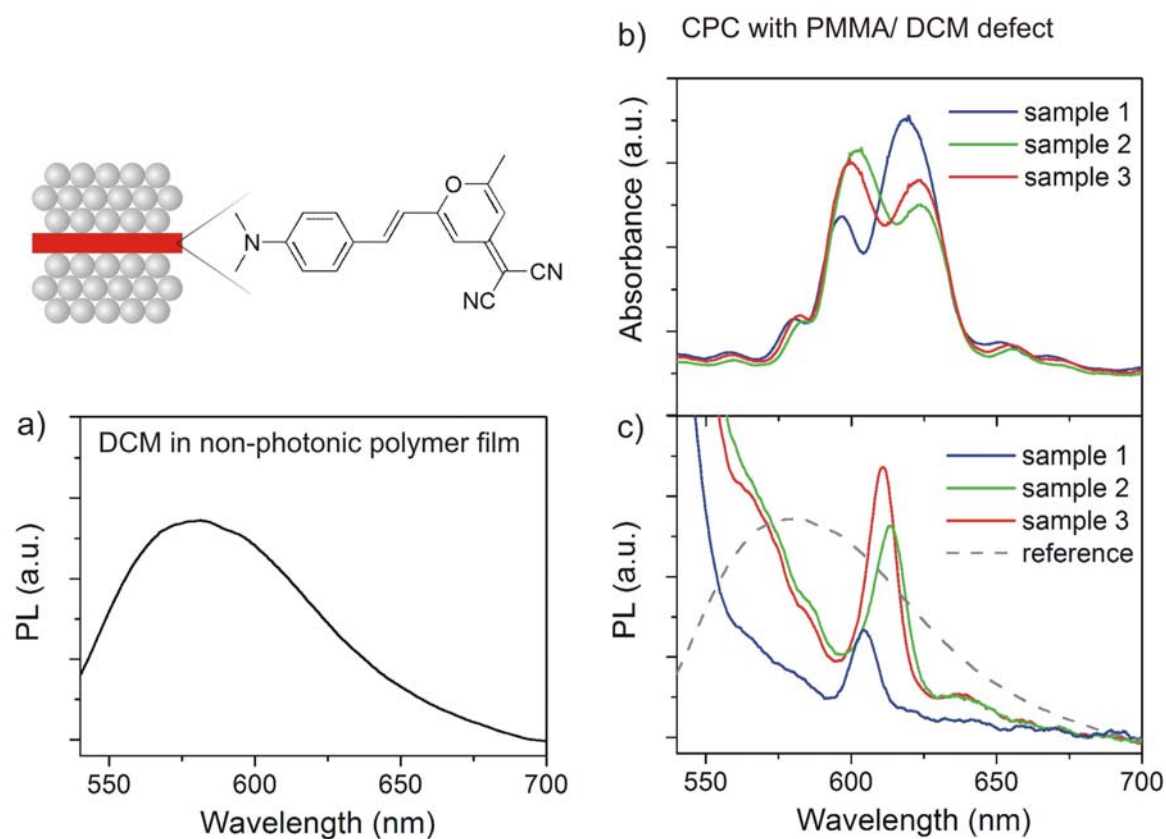


Figure 5.6: Defect CPC with DCM doped PMMA defect layer. a) PL spectrum of DCM in a non-photonic organic polymer film (reference). Excitation wavelength: 532 nm. b) Transmission spectra of DCM doped PMMA defect layer CPCs with defect states at 604 nm, 611 nm and 615 nm, respectively (samples 1-3). c) PL spectra of DCM embedded in the defect layer of samples 1-3. Excitation wavelength: 532 nm.

I prepared CPCs with DCM-doped PMMA defect layers showing defect transmission dips at 604 nm, 611 nm and 615 nm, respectively (Figure 5.6b). Optical characterization in the visible was performed with the setup described in 5.3.1. The PL spectra of the samples as well as the PL reference spectrum of DCM in a non-photonic organic polymer film are shown in Figures 5.6c and 5.6a. The emission of DCM in the defect layer of a CPC is strongly modified compared to the reference. Strong suppression (~70-95%) of spontaneous emission at wavelengths of the photonic stopband is observed, and narrow luminescence peaks emerge at exactly the wavelengths of the defect transmission states. Exact intensity normalizations of modified PL spectra and reference were difficult for the same reasons discussed in 5.3. However, we can realize that the modifying influence of the photonic bandstructure is far more pronounced for all analyzed samples if the fluorophore is exclusively located within the defect layer and not distributed among the entire defect CPC structure. The most important reason for this observation is that light emitters located at or close to the detector-facing CPC surface of a defect CPC with

random fluorophore distribution (examples in 5.3) are not exposed to the photonic bandstructure in detection-direction. Hence, an average PL signal of modified and non-modified emission spectra is recorded.

The optical quality and the Bragg reflection intensities are comparable among the analyzed samples. Consequently, it can be assumed that the different degrees in PL modification are due to different locations of the fluorophores and not caused by defect CPC quality fluctuations.

5.5 Conclusion

Different fluorescent dyes and semiconductor QDs emitting in the visible and NIR at wavelengths of the photonic band gap have been infiltrated into the entire structure of defect CPCs or were exclusively embedded into the defect layer. The PL spectra were clearly modified according to the photonic band structure. PL modification induced by the photonic band gap with defect state was far more pronounced when the fluorophore was exclusively located in the defect layer. In addition, switchable PL modifications were detected by performing thermally induced defect state and Bragg-peak tuning of a QD doped defect CPC.

5.6 References

- (1) Petrov, E. P.; Bogomolov, V. N.; Kalosho, I. I.; Gaponenko, V. A. *Phys. Rev. Lett.* **1998**, *81*, 80.
- (2) Romanov, S. G.; Maka, T.; Sotomayor Torres, C. M.; Müller, M.; Zentel, R. *Appl. Phys. Lett.* **1999**, *75*, 1057.
- (3) Maka, T.; Romanov, S. G.; Müller, M.; Zentel, R.; Sotomayor Torres, C. M. *Phys. Stat. Sol. A* **1999**, *215*, 307.
- (4) Lopez, C.; Blanco, A.; Miguez, H.; Meseguer, F. *Opt. Mater.* **1999**, *13*, 187.
- (5) Megens, M.; Wijnhoven, J. E. G. J.; Lagendijk, A.; Vos, W. L. *J. Opt. Soc. Am. B* **1999**, *16*, 1403.
- (6) Bechger, L.; Lodahl, P.; Vos, W. L. *J. Phys. Chem. B* **2005**, *109*, 9980.
- (7) Kim, K.; Webster, S.; Levi, N.; Carroll, D. L.; Pinto, M. R.; Schanze, K. S. *Langmuir* **2005**, *21*, 5207.
- (8) Shkunov, M. N.; Vardeny, Z. V.; DeLong, M. C.; Polson, R. C.; Zakhidov, A. A.; Baughman, R. H. *Adv. Funct. Mater.* **2002**, *12*, 22.
- (9) Romanov, S. G.; Maka, T.; Sotomayor Torres, C. M.; Müller, M.; Zentel, R. *Appl. Phys. Lett.* **2001**, *79*, 731.
- (10) Schriemer, H. P.; v. Driel, H. M.; Koenderink, A. F.; Vos, W. L. *Phys. Rev. A* **2000**, *63*, 011801.
- (11) Yoshino, K.; Lee, S. B.; Tatsuhara, S.; Kawagishi, Y.; Ozaki, M.; Zakhidov, A. A. *Appl. Phys. Lett.* **1998**, *73*, 3506.
- (12) Romanov, S. G.; Fokin, A. V.; Alperovich, V. I.; Johnson, N. P.; de la Rue, R. M. *Phys. Stat. Sol. A* **1997**, *164*, 169.
- (13) Lodahl, P.; v. Driel, A. F.; Nikolaev, I. S.; Irman, A.; Overgaag, K.; Vanmaekelbergh, D.; Vos, W. L. *Nature* **2004**, *430*, 656.
- (14) Romanov, S. G.; Chigrin, D. N.; Sotomayor Torres, C. M.; Gaponik, N.; Eychmüller, A.; Rogach, A. L. *Phys. Rev. E* **2004**, *69*, 046606.
- (15) Solovyev, V. G.; Romanov, S. G.; Sotomayor Torres, C. M.; Müller, M.; Zentel, R.; Gaponik, N.; Eychmüller, A.; Rogach, A. L. *J. Appl. Phys.* **2003**, *94*, 1205.
- (16) Valenta, J.; Linnros, J.; Juhasz, R.; Rehspringer, J. L.; Huber, F.; Hirlimann, C.; Cheylan, S.; Elliman, R. G. *J. Appl. Phys.* **2003**, *93*, 4471.
- (17) Wang, D.; Rogach, A. L.; Caruso, F. *Chem. Mater.* **2003**, *15*, 2724
- (18) Lin, Y.; Zhang, J.; Sargent, E. H.; Kumacheva, E. *Appl. Phys. Lett.* **2002**, *81*, 3134.

-
- (19) Blanco, A.; Lopez, C.; Mayoral, R.; Miguez, H.; Meseguer, F.; Mifsud, A.; Herrero, J. *Appl. Phys. Lett.* **1998**, *73*, 1781.
- (20) Fleischhaker, F.; Zentel, R. *Chem. Mater.* **2005**, *17*, 1346.
- (21) Romanov, S. G.; Chigrin, D. N.; Solovyev, V. G.; Maka, T.; Gaponik, N.; Eychmüller, A.; Rogach, A. L. Sotomayor Torres, C. M. *Phys. Stat. Sol. A* **2003**, *197*, 662.
- (22) Romanov, S. G.; Fokin, A. V.; de la Rue, R. M. *Appl. Phys. Lett.* **2000**, *76*, 1656.
- (23) Gaponenko, S. V.; Bogomolov, V. N.; Petrov, E. P.; Kapitonov, A. M.; Yarotsky, D. A.; Kalosha, I. I.; Eychmüller, A. A.; Rogach, A. L.; McGilp, J.; Woggon, U.; Gindele, F. *J. Lightwave Technol.* **1999**, *17*, 2128.
- (24) Cademartiri, L.; Bertolotti, J.; Sapienza, R.; Wiersma, D. S.; v. Freymann, G.; Ozin, G. A. *J. Phys. Chem. B Lett.* **2006**, *110*, 671.
- (25) Hall, D. B.; Underhill, P.; Torkelson, J. M. *Polym. Eng. Sci.* **1998**, *38*, 2039.

Chapter 6

6. Future Work and First Results

6.1 Preamble

In this chapter, I will outline some ideas and concepts about future projects that represent a natural and significant extension of the work described in this thesis.

Certainly, we can think of various addressable materials that allow for incorporation as active defect layers into CPCs. We can choose materials being responsive to external stimuli different from the ones investigated in this work. Potential candidates are magnetic particles or liquid crystals that are addressable by magnetic or electric fields, respectively. Also, we can tune parameters like switching-time and -profile or investigate the possibility of monitoring further bio-events, such as DNA mutations, using defect CPCs. In addition, microcontact transfer printing opens the door to the preparation of designed patterned defects by simple use of the corresponding patterned PDMS stamps as printing tool.

Here, I will extend the concept of CPCs with a single active defect layer to CPCs with multiple defect layers of different functionality. In this new generation of "big mac"-type CPCs, the defect layers are vertically stacked and separated by CPC spacer units.

The goal is to combine the functionalities of several single defect CPCs in one multifunctional "big mac"-CPC.

6.2 Multiple Defect Colloidal Photonic Crystals –

Photonic "Big Macs"

To get an idea of the optical properties of multiple defect CPCs, SWA-calculations of the structures were performed. First preliminary results of the simulated transmission spectra show that a certain number N of defect layers vertically stacked in a CPC leads to the same number N of defect states in the Bragg diffraction peak. In more detail, each defect layer of a certain optical thickness induces a corresponding defect state in the Bragg peak (Figure 6.1). Equal thickness of the CPC spacer blocks does not seem to be required. The thickness of the CPC spacer blocks obviously affects the overall shape of the spectra but

does not influence the number of defect states. If the optical thickness of a defect layer matches the periodic CPC modulation, we are basically not confronted with a defect along the [111]-probing direction and consequently no defect state is induced by this defect layer. These results are straightforward to the discussion of the optical spectra of single defect CPCs in section 2.6.

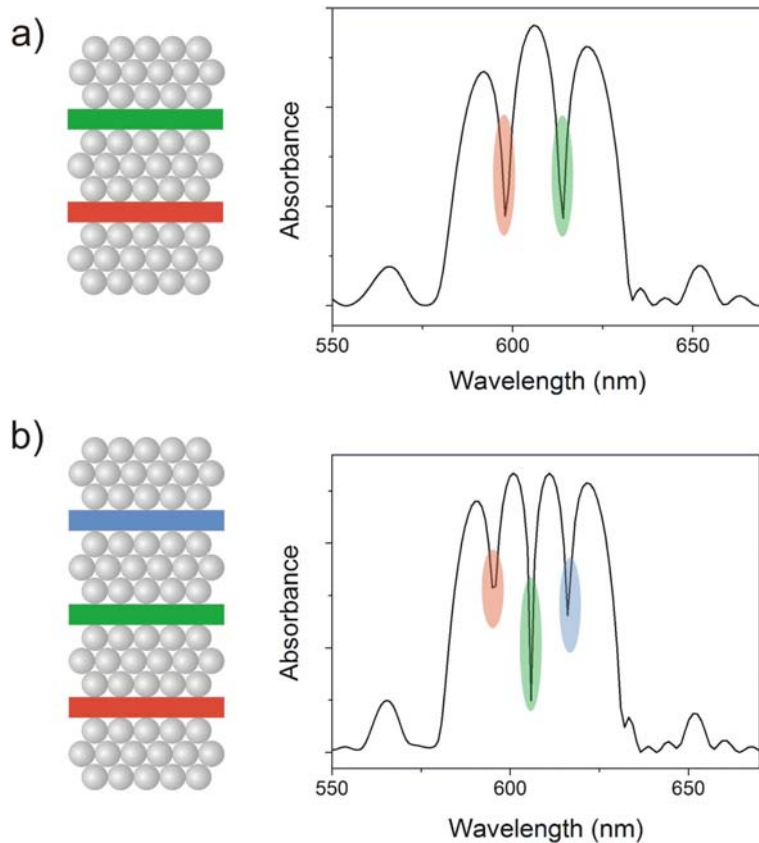


Figure 6.1: Calculated transmission spectra of silica CPCs with multiple vertically stacked defect layers. The CPC spacer units consist of 280 nm spheres and 22 sphere layers each. The refractive index of the defect layers is 1.5 a) CPC with two defect layers of 60 and 120 nm thickness. b) CPC with three defect layers of 50, 90 and 130 nm thickness.

In addition, SWA-simulation show that the described multiple defect wavelengths can be independently tuned. In other words, varying the optical thickness of a specific defect layer by an external stimulus and leaving the optical properties of the remaining defects constant, is expected to solely shift that specific defect wavelength in the optical spectrum. This aspect is exemplified in Figure 6.2: The black lined graph represents the calculated transmission spectrum of a defect CPC (silica spheres, diameter: 280 nm) with defect layers of 50, 100 and 150 nm thickness, respectively, and a refractive index of 1.5. Increasing the thickness of the 50 nm defect layer from 50 to 70 nm and leaving the

remaining parameters constant, solely leads to a red-shift of the first defect wavelength (red lined spectrum). The positions of the 100 and 150 nm defect states are unchanged according to the simulations.

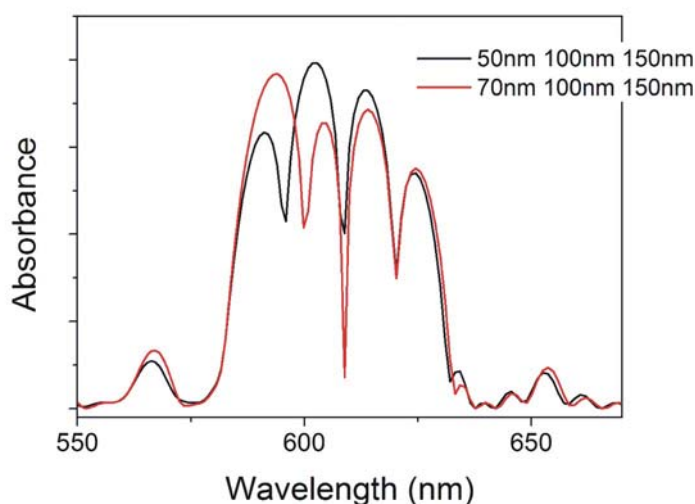


Figure 6.2: Independent defect wavelengths switching. Calculated transmission spectra of a silica CPC (sphere diameter: 280 nm) with vertically stacked defect layers of 50, 100, 150 nm thickness (black line) and 70, 100, 150 nm thickness (red line), respectively. The refractive index of the defect layers is 1.5 and the CPC spacer units consist of 22 sphere layers each.

This property seems to be ideal for combining the functionalities of several single defect CPCs in one multiple defect CPC structure. We can either try to make independent use of the different functionalities fused in one structure or we can for example check the influence of an external stimulus, such as an analyte, on several different defect materials simultaneously! Thinking in terms of biomonitoring, we would not only be able to build horizontally arranged bioarrays based on single defect CPCs, but also additional vertical arrangements, requiring no change in probing spot and only a single dose of analyte, would be an option.

A first experimental realization of a "big mac"-defect CPC containing two vertically stacked planar defects is demonstrated in Figure 6.3. The defects consist of PAZO/PDAC polyelectrolyte multilayers prepared by microcontact transfer printing (see section 2.4.1). The thickness of the defect multilayers is 80 and 160 nm, respectively. Silica spheres of 280 nm in diameter are used.

The preparation is performed in extended analogy to a single defect CPC: I transfer print a first defect layer on a mechanically stabilized (see 2.3.3) bottom-CPC, crystallize a

middle-CPC on top of the first defect layer, mechanically stabilize the middle-CPC, transfer print a second defect layer and crystallize a top-CPC.

A cross-sectional SEM image of the prepared "big mac"-CPC is shown in Figure 6.3a. We can clearly recognize two vertically stacked defect layers of different thickness as well as bottom-, middle- and top CPC. Also, "necking" of bottom- and middle-CPC can be observed due to the appearance of "holes" and "knobs" at the position of the former "necks" (see section 2.5). Slight distortions in the arrangement of the spheres are caused by the required cleaving of the sample. The corresponding experimental transmission spectrum is in good agreement with theoretical predictions (Figure 6.3b): As expected, the two PAZO/PDAC defect layers induce two defect transmission dips in the Bragg peak. The position of the defect wavelengths corresponds to the optical thickness of the defect layers.

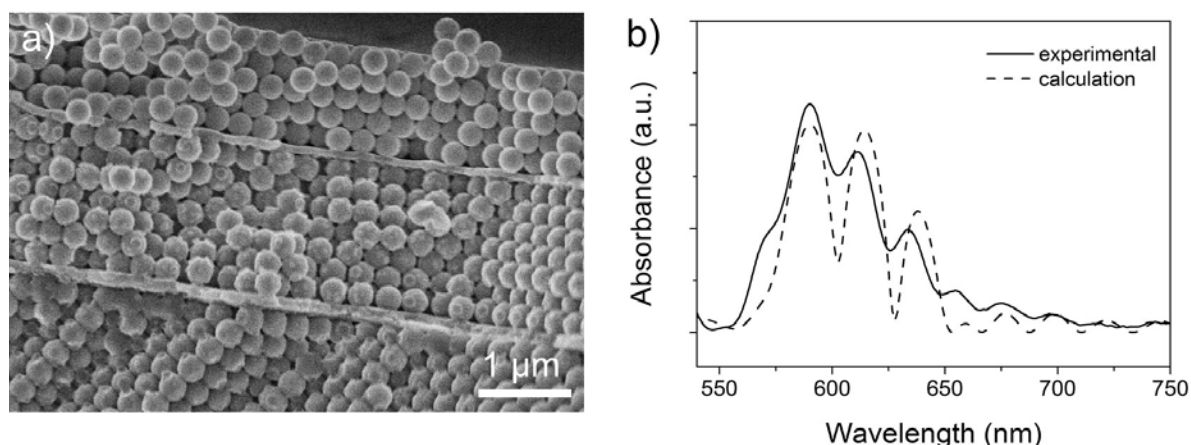


Figure 6.3: a) Cross-sectional SEM image of a silica CPC with two vertically stacked PAZO/PDAC defect layers. b) Corresponding experimental (solid line) and calculated (dotted line) transmission spectrum.

In a next step, we can try to switch the defect states of multiple defect CPCs. Additionally, we can investigate the theoretically proposed possibility of independent defect state switching and monitoring if CPCs with defect materials addressable by different external stimuli are prepared.

The latter could be realized by incorporating several of the functional defect materials presented in Chapters 3 and 4 into one "big mac"-type CPC.

Chapter 7

7. Experimental Part

All chemicals were purchased from Aldrich unless otherwise stated.

7.1 Colloidal Photonic Crystal Synthesis

7.1.1 Sphere Synthesis

7.1.1.1 Silica Spheres

Tetraethyl orthosilicate (TEOS) (98 %), ammonium hydroxide (Caledon Laboratories Ltd, 28-30 wt%, trace metal grade), water (Millipore) and anhydrous ethanol were used as received. Monodisperse silica spheres with sizes ranging from 180 nm - 1.5 μm are synthesized using a modified Stöber/ Giesche procedure^{1,2} involving regrowth described by Giesche³. To produce silica spheres with low polydispersity ($\sim 2\%$), the starting seed size used for regrowth is chosen to be four times smaller than the final sphere size aimed for. The silica spheres produced (seeds and final particles) are cleaned by consecutive centrifuging, decanting and redispersing, first in water (three times) and then in ethanol (three times). If necessary, doublets and smaller spheres (secondary seeds) can be removed by fractioning using sedimentation in a column and removing the upper and lower fractions several times.

7.1.1.1.1 Seeds

Water/ammonia/ethanol and TEOS/ethanol mixtures are prepared at concentrations depending on the seed diameter aimed for (see Ref. 1 and 2). The water/ammonia mixture is put in a round-bottom flask, equipped with paddle stirrer and condenser and placed in a constant temperature bath (60°C). The TEOS/ethanol mixture is added under vigorous stirring (1000 rpm). Depending on the H₂O, NH₃, TEOS concentrations used, the particle growth is completed within a period of a few minutes to several hours (see Ref. 2).

7.1.1.1.2 Re-Growth

A cleaned silica seed dispersion with a concentration of about 0.5 mol Si/L is placed in a round-bottom flask, equipped with paddle stirrer and condenser and surrounded by a constant temperature bath. The seed dispersion is gently stirred (100-200 rpm) at a bath

temperature of 40°C. In separate containers, ammonia/water and TEOS/ethanol mixtures are prepared and continuously added to the seed dispersion using peristaltic pumps. The following amounts are employed:

$$m(\text{TEOS}) = ((d(\text{final})/d(\text{seed})^3 - 1) \cdot m(\text{TEOS, present}))$$

$$m(\text{NH}_3) = M(\text{NH}_3) \cdot 0.8 \text{ mol/L} \cdot V(\text{added})$$

$$m(\text{H}_2\text{O}) = M(\text{H}_2\text{O}) \cdot 8 \text{ mol/L} \cdot V(\text{added})$$

$$V(\text{Ethanol}) = V(\text{added}) - V(\text{NH}_3) - V(\text{H}_2\text{O})$$

with the total added volume $V(\text{added}) = 3 \cdot V(\text{present})$ and $d(\text{final})/d(\text{seed})$ the ratio of final particle diameter to seed diameter.

The addition rate (mol(TEOS)/h) of the TEOS/ethanol mixture is $1/(8 \cdot d(\text{seed}))$ of moles Si present in the initial seed dispersion per hour. The addition rate of the ammonia/water mixture is adjusted correspondingly.

7.1.1.2 Polymer Spheres (PMMA/PGlyMA core-shell spheres)^{4,5*}

Methylmethacrylate (MMA) (99 %), glycidylmethacrylate (GlyMA) (97 %), water (Millipore) and potassium peroxydisulfate (99,99 %) were used as received.

A round-bottom flask, equipped with paddle stirrer, condenser and nitrogen inlet is filled with 150 mL water and heated to 90°C. Having flooded with nitrogen for 45 min, MMA is added. The diameter of the PMMA core-spheres ($d(\text{core})/\text{nm}$) is dependent on the MMA/water concentration ($c(\text{MMA})/\text{mol/L}$). The amount of injected MMA is determined according to the following approximate equation:

$$\lg d(\text{core}) \approx 1/3 \cdot \lg c(\text{MMA}) + 2.5.^4$$

To start the polymerisation, 5 mL of an aqueous potassium peroxydisulfate solution (10 wt%) (previously heated to 90°C under nitrogen flow) are injected and the reaction mixture is stirred at 400 rpm.

After complete conversion of MMA (~ 2h), GlyMA is added to the reaction mixture. The amount of injected GlyMA is dependent on the final diameter $d(\text{core-shell})$ of the PMMA/PGlyMA core-shell spheres aimed for ($\lg d(\text{core-shell}) \approx 1/3 \lg c(\text{MMA} + \text{GlyMA}) + 2.5$). Good mechanical stabilization of PMMA/PGlyMA CPCs is achieved for $V(\text{MMA})/V(\text{GlyMA}) = 9/1$.

When the final sphere size is reached, the polymerization is quenched with air and the spheres are purified from large agglomerations by filtration. Minor agglomerations and low molecular impurities are removed by consecutive centrifuging, decanting and redispersing in water (three to five times). Sphere diameters between 150 and 600 nm can

be prepared by this method. The preparation of larger spheres requires additional ionic stabilization to prevent coagulation.⁴

* synthesis was carried out by Birger Lange (University of Mainz)

7.1.2 Crystallization

Glass microscope slides (Corning) are cleaved in two pieces lengthwise, cleaned in freshly prepared Piranha solution ($\text{H}_2\text{SO}_4/30\% \text{H}_2\text{O}_2$, 3:1) and rinsed first with water and then with ethanol.

7.1.2.1 Silica Sphere Crystallization

Silica spheres dispersed in ethanol (6-10 mL) are placed in cylindrical glass vials (Fisher). The particle volume fraction (ϕ) of the dispersions allows for an approximate prediction of the final number of sphere layers (k) according to

$$k = L \cdot \phi / (0.605 \cdot d \cdot (1 - \phi))$$

where d is the sphere diameter and L the meniscus height (310 μm for ethanol).⁶

To deposit a colloidal crystal film, the cleaned glass slides are carefully centered in a vial with the dispersion using two small paper clips. In case of sphere diameters $< 450 \text{ nm}$ crystallization is performed on a vibration free table at normal pressure and 40°C ambient temperature. The vial is covered with a crystallizing dish in such a way that evaporated ethanol can escape but deposited films are subjected to minimal air current fluctuations. For sphere diameters $> 450 \text{ nm}$, crystallization is performed at reduced pressure and room temperature. The vial is placed in a desiccator and dynamic vacuum (45 Torr) is applied.

7.1.2.2 Polymer Sphere Crystallization

PMMA/PGlyMA spheres are crystallized by slowly drawing a vertically placed glass slide out of the corresponding aqueous dispersion (3-6 vol %).⁷ For this purpose the upper end of a glass slide is connected to a small electric motor operating at a rate of $\sim 100 \text{ nm/s}$. The vial containing the polymer dispersion and the immersed glass slide is placed on a vibration free table. The entire system is protected from air fluctuations by a large glass box. Crystallization is performed at normal pressure and room temperature.

7.1.3 Mechanical Stabilization

7.1.3.1 Silica CPCs

Silicon tetrachloride (99 %) and water (millipore) are placed in two parallelly connected bubble counters through which a nitrogen stream is flowed. This flow transports either of the reactants to the reactor chamber where the silica CPC crystallized on a glass substrate is located. A porous glass septum placed between the bubble counters and the reactor favors the homogeneity of the reactive gas in the sample compartment. The CPC is subsequently exposed to water and SiCl₄ vapors with a nitrogen drying sequence in between. The following exposure times were used: 7 min water vapor, 5 min nitrogen, 5 min SiCl_{4(g)}, 5 min nitrogen.

7.1.3.2 PMMA/PGlyMA CPCs

PMMA/PGlyMA core-shell CPCs are heated at about 90°C for about 1h until the desired mechanical stability is reached.

7.2 Defect Formation

7.2.1 Method 1

(LbL self-assembly/ Microcontact transfer printing)

A piece of flat sheet of poly(dimethylsiloxane) (PDMS) is prepared by casting a PDMS pre-polymer (Sylgard 184, Dow Chemical) against a silicon wafer cleaned in piranha solution (H₂SO₄/ 30 % H₂O₂, 3:1) and hydrophobized with 1,1,2,2-tetrahydroperfluorooctyltrichlorosilane. The prepolymer is cured at 60°C for 2 hours then carefully peeled off the wafer.

The LbL self-assembled multilayer on PDMS is prepared by alternately dipping a PDMS stamp into the corresponding solutions of anionic and cationic macromolecules for 15 min and rinsing twice in water for 5 min before switching, until a desired layer thickness is achieved. The following aqueous solutions were used:

- Poly(allylamine hydrochloride) (PAH, MW = 70 000): 10 mM PAH (repeat unit basis), 0.1 M NaCl
- Poly(diallyldimethylammonium chloride) (PDAC, MW = 100 000-200 000, 20 wt % in water): 10 mM PDAC (repeat unit basis), 0.1 M NaCl

- Poly[1-[4-(3-carboxy-4-hydroxyphenyl-azo)benzenesulfonamido]-1,2-ethandiyl, sodium salt] (PAZO): 10 mM PAZO (repeat unit basis), 0.1 M NaCl
- DNA sodium salt, Type I, "Highly Polymerized" from calf thymus: 0.02 wt% DNA, 10 mM phosphate buffered saline
- Anionic polyferrocenylsilane (PFS(-), MW ~ 100 000, see section 3.4): 10 mM (repeat unit basis), 0.1 M NaCl
- Cationic polyferrocenylsilane (PFS(+), MW ~ 100 000, see section 3.4): 10 mM (repeat unit basis), 0.1 M NaCl
- Poly-L-lysine hydrochloride (PLL, MW > 30 000): 0.05 wt% PLL, 0.5 M NaCl
- Poly-L-glutamic acid sodium salt (PLGA, MW 15 000-50 000): 0.05 wt% PLGA, 0.5 M NaCl

PAH is always used as base-layer in the LbL self-assembly process on a PDMS sheet.

Transfer printing of the PDMS-supported LbL self-assembled multilayer is performed by putting a drop of water on the colloidal crystal, applying the PDMS under pressure, and drying the sample. The PDMS is then carefully peeled off leaving the multilayer on the crystal. A second colloidal crystal of identical diameter spheres is then grown on top of the transfer printed defect layer.

7.2.2 Method 2

(Sacrificial ribose infiltration/ Spin-coating)

The surface of a mechanically stabilized silica CPC is covered with a thin layer of D-Ribose (99 %) and the sample is heated to 100°C on a hot plate. To avoid the formation of a ribose overlayer on the CPC, a flat PDMS slab is pressed onto the surface of the (melted) ribose-CPC composite and the sample is heated at 180°C under house-vacuum overnight, allowing any excess sugar to flow out the sides of the sample. After cooling to solidify the ribose, the PDMS is carefully peeled off. Spin-coating of the corresponding defect layer is performed on top of the ribose infiltrated CPC. The sacrificial ribose filling is dissolved in water (waterbath, overnight) and a top-CPC of identical diameter spheres is grown over the spin-coated defect.

The following spin-coating parameters were used for the preparation of Kraton G[®] (365 ± 10 nm) and PMMA (275 ± 10 nm) defect layers: 4 wt% polymer dissolved in toluene, 2 s acceleration time, 60 s spinning time, 1000 rpm.

7.3 PbS Quantum Dot Synthesis*

1 g PbCl₂ (98%) and 1.93 g oleylamine (OLA, technical grade) are magnetically stirred under N₂ flow in a round-bottom flask. The mixture is heated to 100°C, the reaction flask sealed with a rubber septum, and vacuum applied for 5 min. The flask is reopened, the N₂ flow restored, and the temperature increased to 120°C, where it is left for 30 min, always under vigorous stirring. During that time, the PbCl₂-OLA mixture turns into a highly viscous, homogeneous gel. The sulfur precursor solution is prepared in the meantime by adding 0.0115 g of elemental sulfur to 0.2 g of OLA. Dissolution of the elemental sulfur can be completed by ultrasonication and gentle heating at 80°C in an oven with frequent shaking. The sulfur solution is then injected at room temperature into the stirring PbCl₂-OLA gel, and nucleation proceeds almost instantaneously. The temperature is stabilized to 100°C for the subsequent growth. Once the desired size is achieved the reaction is quenched by pouring the product into cold hexane. The mixture is centrifuged for 15 min at 3000 rpm to precipitate the excess PbCl₂ precursor. A minimum amount of ethanol is added to the supernatant to induce precipitation of the nanocrystals. The solutions are centrifuged, the supernatant is discarded, and the precipitate is redispersed in hexane. To further purify the nanocrystals, 200 vol% of oleic acid are added to the hexane dispersions of PbS nanocrystals, and the samples are shaken for 5 min and centrifuged. The supernatant is discarded, and the nanocrystals are redispersed in hexane. The nanocrystals are further precipitated twice with ethanol and redispersed in hexane to remove any further trace of ligands.

*synthesis was performed by Ludovico Cademartiri (University of Toronto)

7.4 PFS-Polyelectrolyte Synthesis

The anionic PFS-polyelectrolyte is prepared according to Ref. 8. The cationic PFS-polyelectrolyte is prepared according to Ref. 9. The synthesis was performed by Dr. Zhuo Wang (University of Toronto).

7.5 Instruments

7.5.1 Transmission/Reflection Spectroscopy

Transmission spectra in the visible were recorded using an Ocean Optics SD 2000 fiber-optics spectrometer interfaced to an Olympus BX-2000 optical microscope (Figure 7.1). A spot size of 2 μm in diameter can be probed with this setup and real time measurements are possible.

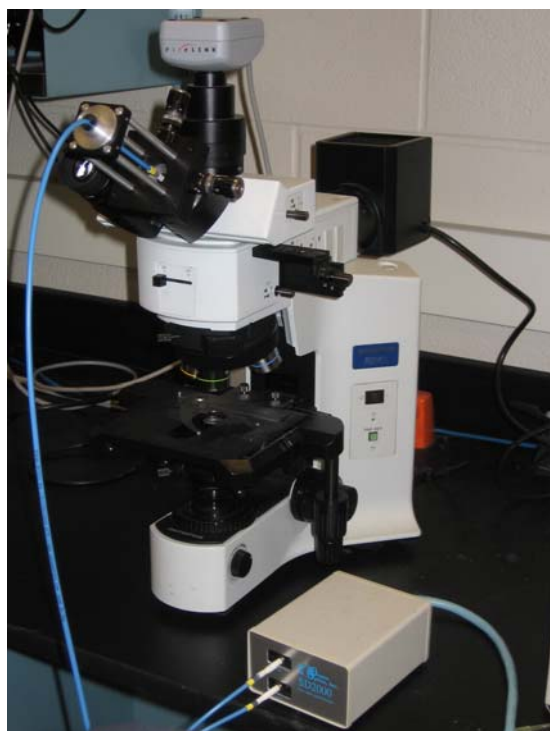


Figure 7.1: Fiber-optics spectrometer attached to an optical microscope (photograph).

Transmission spectra in the NIR were recorded with a UV/VIS/NIR spectrometer Lambda 900 from Perkin Elmer.

Transmission and reflection spectra of fluorescent defect CPCs were taken with optical bench setups (described in section 5.3) that allow for successive reflection/ transmission and photoluminescence measurements at the same sample spot.

7.5.2 Photoluminescence (PL) Spectroscopy

PL measurements were performed in the visible and NIR with optical bench setups described in section 5.3.

7.5.3 Ellipsometry

Ellipsometry measurements were performed with a SOPRA GES-5 variable angle spectroscopic ellipsometer. Measurements were taken in a wavelengths range between 200 and 1600 nm and it was operated at two angles of incidence (70° and 75°) to increase the accuracy of the obtained data. A silicon wafer was used as substrate and a 1 nm silica surface layer was taken into account in the corresponding fits (Ellipsometric data analysis software V.A.S.E., J.A. Wollam Co. Inc.).

7.5.4 Scanning Electron Microscopy (SEM)

Cross-sectional SEM images were obtained using a Hitachi S-5200 field emission scanning electron microscope, first coating the samples with a ~ 5 nm carbon film by arc-discharge (Emitech K950X).

7.5.5 Photography

Photographs were taken with a Canon PowerShot A520 digital camera.

7.5.6 Thermal Gravimetric Analysis (TGA)

TGA measurements were performed with a TGA Q500 from TA Instruments, Inc..

7.5.7 Heating and Cooling Stage

Temperature switching experiments were performed with a thermoelectric Peltier element based heating and cooling stage LTS 120 from Linkam Scientific Instruments Ltd..

7.5.8 LbL Self-assembly

The LbL dipping assembly was carried out using a modified Microm DS 50 programmable slide stainer from Richard-Allan Scientific, Co. to automate the process.

7.5.9 Spin-coating

Spin-coating of thin films was performed with a WS-400B-6NPP/LITE spin-coater from Laurel technologies corporation.

7.5.10 SWA-Simulations

SWA-theory based software (see section 1.2.4) for simulations of defect CPC absorption

and reflection spectra was provided by Dr. Georg v. Freymann. For all single defect CPC simulations, the following standard input parameters were used:

- 20 bottom silica CPC sphere layers
- 20 top silica CPC sphere layers
- 10 vol% SiO₂ contents in bottom-CPC voids (necking)
- 8 vol% water contents in top and bottom CPC voids at room temperature
- silica substrate

The remaining variable input parameters (sphere size, defect layer thickness and refractive index etc.) are mentioned and discussed in the corresponding sections of this thesis.

7.6 References

- (1) Stöber, W.; Fink, A.; Bohn E. J. *J. Colloid Interface Sci.* **1968**, *26*, 62.
- (2) Giesche, H. *J. Eur. Ceram. Soc.* **1994**, *14*, 189.
- (3) Giesche, H. *J. Eur. Ceram. Soc.* **1994**, *14*, 205.
- (4) Egen, M., Thesis, 2003.
- (5) Lange, B.; Zentel, R.; Ober, C. K. *Polymer Preprints* **2006**, *47*, 517.
- (6) Jiang, P.; Bertone, J. F.; Hwang, K. S.; Colvin, V. L. *Chem. Mater.* **1999**, *11*, 2132.
- (7) Egen, M.; Voss, R.; Griesebock, B.; Zentel, R. *Chem. Mater.* **2003**, *15*, 3786.
- (8) Wang, Z.; Lough, A.; Manners, I. *Macromol.* **2002**, *35*, 7669.
- (9) Jäkle, F.; Wang, Z.; Manners, I. *Macromol. Rapid Commun.* **2000**, *21*, 1291.

List of Abbreviations

AFM	atomic force microscopy
CPC	colloidal photonic crystal
CVD	chemical vapor deposition
cw	continuous wave
DCM	4-(dicyanomethylene)-2-methyl-6-(p-dimethyl-aminostyryl)-4H-pyran
DOS	density of states
GlyMA	glycidylmethacrylate
LB	Langmuir-Blodgett
LbL	layer-by-layer
MMA	methylmethacrylate
NIR	near infrared
OLA	oleylamin
PAH	poly(allylamine hydrochloride)
PAZO	poly[1-[4-(3-carboxy-4-hydroxyphenyl-azo)benzenesulfonamido]-1,2-ethandiyl, sodium salt]
PDAC	poly(diallyldimethylammonium chloride)
PDMS	poly(dimethylsiloxane)
PFS	poly(ferrocenylsilane)
PGlyMA	poly(glycidylmethacrylate)
PL	photoluminescence
PLGA	poly-L-glutamic acid
PLL	poly-L-lysine
PMMA	poly(methylmethacrylate)
PVD	physical vapor deposition
PWM	planar wave method
QD	quantum dot
R6G	Rhodamine 6G
ROP	ring-opening polymerization
rpm	rotations per minutes
SAM	self-assembled monolayer
SEM	scanning electron microscopy

SPR	surface plasmon resonance
SWA	scalar wave approximation
TEM	transmission electron microscopy
TEOS	tetraethyl orthosilicate
TGA	thermal gravimetric analysis
THF	tetrahydrofuran

List of Figures

- Figure 1.1:** Photonic bandstructure diagram (a) and corresponding DOS diagram (b) of a fcc-lattice of air spheres in a dielectric matrix ($\epsilon = 11,9$).
- Figure 1.2:** Schematic illustration of one, two and three dimensional periodicity in a medium.
- Figure 1.3:** Electron microscopy images of different photonic crystal types with 1D, 2D and 3D periodicity. a) GaAs-AlAs Bragg stack. b) Air cylinders in silicon. c) Silicon woodpile structure.
- Figure 1.4:** 1D, 2D and 3D photonic crystals in nature. Left: a) Abalone shell inside, b) sea mouse *Aphrodita*, c) butterfly *Morpho didus* (photographs). Right: a) Nacre at the inside of an abalone shell, b) sea mouse spine, c) butterfly wing of *Callophrys rubi* (electron microscopy images in cross-section).
- Figure 1.5:** a) SEM image (left) and photographs (right) of natural opals. b) SEM image of a synthetic polymer opal (left). Photographs of synthetic opals with stop bands at wavelength between 400 nm and 650 nm (right).
- Figure 1.6:** a) Surface of a high-quality silica CPC, b) cross-section of a silicon inverted CPC (SEM images).
- Figure 1.7:** Path of light hitting the surface of a CPC.
- Figure 1.8:** Examples of air and dielectric defects and the defect states appearing in the photonic band gap. The defect is caused by a differently sized rod in a two-dimensional photonic crystal consisting of dielectric rods in air.
- Figure 1.9:** a) E-beam lithographically introduced point air defect in a self-assembled CPC. b) GaAs woodpile structure with line air defect prepared by laser lithography and wafer fusion. c) Inverted silica CPC with planar silica defect prepared in a complete bottom-up approach. (Electron microscopy images)
- Figure 1.10:** a) Schematic illustration of the LbL self-assembly process. Steps 1 and 3 represent the adsorption of polyanion and polycation, respectively, and steps 2 and 4 are rinsing steps. The four steps are the basic buildup sequence for the simplest film architecture $(A/B)_n$. The construction of more complex film architectures requires only additional polyelectrolyte and rinsing solutions and a different deposition sequence. b) Simplified

molecular picture of the first two adsorption steps when starting from a positively charged substrate.

Figure 1.11: Ellipsometry schematically illustrated. The change in polarization of light upon reflection on the surface of a sample on a substrate is measured.

Figure 2.1: Schematic representation of evaporation induced self-assembly on a flat, vertical substrate.

Figure 2.2: Mechanical stabilization of CPCs from a) silica spheres and b) PMMA/PGlyMA core-shell spheres. (Schematical illustration)

Figure 2.3: Schematic illustration of method 1: a) Growth of a LbL multilayer onto a flat PDMS stamp. b) Transfer printing of the multilayer stack onto the mechanically stabilized bottom CPC. c) Crystallization of the top CPC.

Figure 2.4: Preparation of a CPC with spin-coated defect layer (method 2). a) A sacrificial sugar filling is melted into the voids of a mechanically stabilized silica CPC. Top compression with a PDMS sheet prevents the formation of an overlayer. b) The PDMS sheet is carefully peeled off after complete infiltration and solidification of the sugar. c) Spin-coating of various materials from hydrophobic solvents can be performed on top of the infiltrated CPC. d) The sacrificial sugar filling is dissolved in water. e) A second silica CPC is grown to complete the defect structure.

Figure 2.5: Representative cross-sectional SEM micrographs of silica CPCs with LbL self-assembled defect layer prepared according to method 1.

Figure 2.6: Representative cross-sectional SEM images at different preparation steps of method 2. a) Ribose infiltrated silica CPC. b) CPC with spin-coated dye doped PMMA defect layer.

Figure 2.7: Optical spectra of a silica CPC (a) and a silica CPC with embedded polyelectrolyte defect layer (b). The samples are probed in transmission along the [111]-axis of the colloidal crystal.

Figure 2.8: Optical transmission spectra at normal incidence of a silica CPC before and after mechanical stabilization.

Figure 2.9: a) PDMS sheet with PAZO/PDAC polyelectrolyte multilayer (photograph). b) CPC with transfer printed PAZO/PDAC polyelectrolyte multilayer (photograph). c) Optical transmission spectra at normal incidence of a CPC with PAZO/PDAC polyelectrolyte multilayer surface defects of different thickness.

- Figure 2.10:** Optical transmission spectra at normal incidence of defect CPCs with PAZO/PDAC multilayers of different thickness.
- Figure 2.11:** Optical spectra of a silica CPC with spin-coated PMMA/DCM defect layer at different preparation steps: (1) mechanically stabilized bottom-CPC; (2) sugar infiltrated bottom-CPC with spin-coated PMMA/DCM layer; (3) final structure. The spectra are taken in transmission along the CPC-[111]-axis.
- Figure 2.12:** Calculated transmission spectra at normal incidence of a CPC (a) and a defect CPC (b). Spatial distribution of the square magnitude of the electric field for the wavelengths λ_1 (c) and λ_2 (d). e) Calculated position of defect state versus defect thickness. Input parameters: CPC spheres of $d = 280$ nm and $n = 1.43$, CPC thickness of 40 sphere layers, planar defect of $n = 1.5$ and thickness 100 nm between 20th and 21st sphere layer.
- Figure 3.1:** Schematic illustration of tunable defect CPCs.
- Figure 3.2:** UV-induced trans-to-cis isomerization and partial thermal backisomerization of the azo-group in a PAZO polyelectrolyte molecule.
- Figure 3.3:** Top: Transmission spectra of a PAZO/ PDAC defect CPC at different a) UV-irradiation and b) backisomerization times. The insets show a magnification of the defect state positions. Bottom: Dependence of defect state wavelength on c) UV-irradiation and d) backisomerization time. Exponential and logarithmic fits are applied.
- Figure 3.4:** Experimental (solid lines) and calculated (dotted lines) transmission spectra (normalized) of a PAZO defect CPC in the initial and photoisomerized form.
- Figure 3.5:** a) Transmission spectra of a PAZO/PDAC defect CPC at temperatures between 10°C and 80°C (staggered). b) Dependence of defect state wavelength on temperature during heating and cooling cycles ("conditioning" cycles are not shown). c) Changes in defect state and blue band edge wavelength during the applied heating and cooling steps.
- Figure 3.6:** Experimental (solid lines) and calculated (dotted lines) transmission spectra (normalized) of a PAZO/PDAC defect CPC at 10°C and 80°C .
- Figure 3.7:** Molecular structures of the anionic and cationic PFS polyelectrolytes.

- Figure 3.8:** a) Transmission spectra of a PFS defect CPC in the reduced state and after different oxidation times (staggered). b) Changes of the wavelength position of the defect state during multiple redox cycles.
- Figure 3.9:** Experimental (solid lines) and calculated (dotted lines) transmission spectra (normalized) of a PFS defect CPC in the reduced, semi-oxidized and fully oxidized form.
- Figure 3.10:** Schematic illustration of the physically crosslinked elastomer Kraton G[®] as mechanically tunable CPC defect layer.
- Figure 3.11:** a) Transmission spectra of a CPC with spin-coated elastomeric Kraton G[®] defect layer. Initial spectrum and spectra when applying mechanical pressure ($P_1 < P_2$) perpendicular to the sample surface. b)-d) Experimental (solid lines) and calculated (dotted lines) transmission spectra (normalized) of a Kraton G[®] defect CPC in the initial state and when applying pressure.
- Figure 4.1:** Optical detection of DNA melting and annealing. a) Scheme illustrating denaturation and hybridization effects of DNA double strands embedded as a planar defect in a CPC. b,c) Transmission spectra of a calf-thymus DNA defect CPC at temperatures between 40°C and 98 °C upon heating (b) and cooling (c). The insets show a magnification of the defect state position. d) Changes in defect state wavelength and blue band edge during the applied heating and cooling steps.
- Figure 4.2:** Experimental (solid lines) and calculated (dotted lines) transmission spectra (normalized) of a calf-thymus DNA defect CPC below (70°C) and above (90°C) the DNA denaturation temperature.
- Figure 4.3:** Chiral differentiation of an anti-cancer drug using DNA CPC defects. a) Due to the right-handed helical structure of calf-thymus DNA, the chiral anti-cancer drug daunorubicin shows a preferred binding affinity to the DNA double helix compared to the inactive enantiomer WP900. b,c) Transmission spectra of calf thymus DNA defect CPCs recorded after different exposure times to daunorubicin (b) and WP900 (c) dissolved in water (10^{-4} M). d) Changes of the defect state wavelength of DNA defect CPCs depending on the exposure times to the corresponding daunorubicin and WP900 solutions.
- Figure 4.4:** Experimental (solid lines) and calculated (dotted lines) transmission spectra (normalized) of a calf-thymus DNA defect CPC in the initial state and after

10 min immersion in a 10^{-4} M solution of the anti-cancer drug daunorubicin.

Figure 4.5: a) Molecular model of bovine trypsin showing the key residues in the active site. b) Mechanism of the trypsin catalyzed peptide cleavage.

Figure 4.6: PLL/ PLGA defect CPC exposed to trypsin (680 BAEE units/mg) in ammonium bicarbonate solution (10mM). a) Transmission spectra (staggered) of a PLL/ PLGA defect CPC recorded after different exposure times. b) Defect state wavelength and simulated defect thickness depending on the exposure time. c)-h) Simulated transmission spectra (dotted lines) along with the corresponding experimental spectra (solid lines) plotted in a).

Figure 4.7: PLL/ PLGA defect CPC exposed to trypsin (680 BAEE units/mg) in deionized water. a) Transmission spectra (staggered) of a PLL/ PLGA defect CPC recorded after different exposure times. b) Defect state wavelength and simulated defect thickness depending on the exposure time. c)-h) Simulated transmission spectra (dotted lines) along with the corresponding experimental spectra (solid lines) plotted in a).

Figure 4.8: Schematic representation of a cross-section cut through the centers of the spheres in a [111] triangular stacking. Simple euclidian geometry allows for calculation of the interstitial area (red shaded) as well as for determination of the maximum radius of a spherically shaped object that can pass through a CPC void.

Figure 5.1: Sketch of the optical setup allowing for probing reflection/ transmission and photoluminescence at the same sample spot.

Figure 5.2: Defect CPC doped with R6G. a) PL spectrum of R6G on amorphous non-photonics silica (reference). Excitation wavelength: 532 nm. b) Defect CPC spectrum in reflection. c) PL spectrum of R6G incorporated in defect CPC (red solid line) and PL spectrum of normalized reference (black dashed line). Excitation wavelength: 532 nm.

Figure 5.3: Optical transmission spectra of a CPC with 40 bilayer polyelectrolyte multilayer (PEM) surface defect at different preparation steps .

Figure 5.4: Defect CPC doped with PbS QDs. a) PL spectrum of PbS QDs on amorphous silica (reference). Excitation wavelength: 514 nm. b) Defect CPC spectra in reflection at 10 and 90°C. c) PL spectrum of PbS QDs

incorporated in defect CPC at 10 and 90°C. Excitation wavelength: 514 nm. d) Dependence of defect state wavelength on temperature during heating and cooling cycles. e) Dependence of defect emission wavelength on temperature during the applied heating and cooling steps.

Figure 5.5: Experimental (solid lines) and simulated (dotted lines) transmission spectra of a PAZO/PDAC defect CPC at 10°C and 90°C.

Figure 5.6: Defect CPC with DCM doped PMMA defect layer. a) PL spectrum of DCM in a non-photonic organic polymer film (reference). Excitation wavelength: 532 nm. b) Transmission spectra of DCM doped PMMA defect layer CPCs with defect states at 604 nm, 611 nm and 615 nm, respectively (samples 1-3). c) PL spectra of DCM embedded in the defect layer of samples 1-3. Excitation wavelength: 532 nm.

Figure 6.1: Calculated transmission spectra of silica CPCs with multiple vertically stacked defect layers. The CPC spacer units consist of 280 nm spheres and 22 sphere layers each. The refractive index of the defect layers is 1.5 a) CPC with two defect layers of 60 and 120 nm thickness. b) CPC with three defect layers of 50, 90 and 130 nm thickness.

Figure 6.2: Independent defect wavelengths switching. Calculated transmission spectra of a silica CPC (sphere diameter: 280 nm) with vertically stacked defect layers of 50, 100, 150 nm thickness (black line) and 70, 100, 150 nm thickness (red line), respectively. The refractive index of the defect layers is 1.5 and the CPC spacer units consist of 22 sphere layers each.

Figure 6.3: a) Cross-sectional SEM image of a silica CPC with two vertically stacked PAZO/PDAC defect layers. b) Corresponding experimental (solid line) and calculated (dotted line) transmission spectrum.

Figure 7.1: Fiber-optics spectrometer attached to an optical microscope (photograph).

List of Tables

Table 2.1: Monodisperse sphere dispersions of different sphere diameters and materials.

Table 2.2: Functional defect layer materials and preparation method.

Curriculum Vitae

Personal information

Name: Friederike Yasmin Fleischhaker
Date of Birth: 03.11.1980
Nationality: German

Education

08/1986-08/1990 Theitalschule (elementary school), Niedernhausen

08/1990-08/1999 Gymnasium am Mosbacher Berg (high school), Wiesbaden

06/1999 Abitur (University entrance qualification equivalent) at
Gymnasium am Mosbacher Berg, Wiesbaden
Result: "very good" (1.0)

10/1999-09/2004 Studies of Chemistry at the Johannes Gutenberg-University,
Mainz

10/2001 Diplomvorprfung (intermediate diploma) in Chemistry
Result: "very good" (1.0)

08/2002-03/2003 Exchange semester at the University of Toronto (Canada)

03/2004-09/2004 Research for Diploma Thesis (Macromolecular and Physical
Chemistry)
Research supervisor: Prof. R. Zentel (University of Mainz)
Research project: Synthesis and Characterization of Colloidal
Photonic Crystals from Polymer Core-Shell Spheres with
Embedded CdSe Quantum Dots

09/2004 Diploma Degree in Chemistry
Result: "very good" (1.0)

10/2004-05/2007 Joint Ph.D. research at the University of Toronto (01/2005-
04/2006) and the Johannes Gutenberg-University, Mainz
(10/2004-12/2004 and 04/2006-05/2007) under supervision of
Prof. R. Zentel and Prof. G.A. Ozin
Research project: Designed Functional Defects in Colloidal
Photonic Crystals: Switching, Biomonitoring and Modified
Photoluminescence

Awards and Scholarships

1998	"Deutsche Schülerakademie" (summer school for highly gifted students)
2002-2004	Scholarship from the "Studienstiftung des deutschen Volkes"
2002-2003	DAAD (German academic exchange service) research scholarship for exchange term at the University of Toronto, Canada
2005-2007	Graduate Scholarship from the "Fonds der chemischen Industrie"
2005	Outstanding Poster Award (MRS Fall Meeting 2005, Boston)
2006	Procter&Gamble Award for outstanding diploma examination
2006-2007	Fellow of POLYMAT (Polymers in Advanced Technologies) Graduate Class of Excellence and Max-Planck Research School, Mainz
2006	Materials Research Society Graduate Student Silver Award (MRS Fall Meeting 2006, Boston)
2006-2007	Junior fellow of "Gutenberg-Akademie", Mainz

Presentations

Poster Presentation. Lange, B.; Fleischhaker, F.; Ye, J.; Zentel, R. Functional 3D Photonic Films from Polymer Beads. *DFG-Meeting*, Berlin, Germany, 2004

Poster Presentation. Fleischhaker, F.; Lange, B., Zentel, R. Functional 3D Photonic Films from Polymer Beads. *MWFZ-Meeting*, Mainz, Germany, 2005

Poster Presentation. Fleischhaker, F.; Arsenault, A. C.; Tetreault, N.; Wang, Z.; Kitaev, V.; Peiris, F. C.; Mihi, A.; Miguez, H.; v. Freymann, G.; Manners, I.; Zentel, R.; Ozin, G. A. "Smart" Defects in Colloidal Photonic Crystals. *MRS Fall Meeting*, Boston, USA, 2005, **Outstanding poster award**

Oral Presentation. Fleischhaker, F.; Arsenault, A. C.; Tetreault, N.; Wang, Z.; Kitaev, V.; Peiris, F. C.; Mihi, A.; Miguez, H.; v. Freymann, G.; Manners, I.; Zentel, R.; Ozin, G. A. Tunable Defects in Colloidal Photonic Crystals. *SPIE Conference*, Strasbourg, France, 2006

Oral Presentation. Fleischhaker, F.; Arsenault, A. C.; Wang, Z.; Kitaev, V.; Peiris, F. C.; Manners, I.; Zentel, R.; Ozin, G. A. *PHAT-Meeting*, Helsinki, Finland, 2006

Oral Presentation (invited): Fleischhaker, F. "Smart" Defects in Colloidal Photonic Crystals, *MIT*, Dept. of Chemical Engineering, Cambridge, USA, 2006

Oral Presentation. Fleischhaker, F.; Arsenault, A. C.; Wang, Z.; Kitaev, V.; Peiris, F. C.; Manners, I.; Zentel, R.; Ozin, G. A. Colloidal Photonic Crystals with Designed Functional Polyelectrolyte Multilayer Defects. *ACS Fall Meeting*, San Francisco, USA, 2006

Oral Presentation. Fleischhaker, F.; Arsenault, A. C.; Wang, Z.; Kitaev, V.; Peiris, F. C.; Manners, I.; Zentel, R.; Ozin, G. A. Switching and Monitoring with Functional Defects in Colloidal Photonic Crystals. *MRS Fall Meeting*, Boston, USA, 2006

Oral Presentation. Fleischhaker, F.; Arsenault, A. C.; Wang, Z.; Kitaev, V.; Peiris, F. C.; Manners, I.; Zentel, R.; Ozin, G. A. Switching and Monitoring with Functional Defects in Colloidal Photonic Crystals. *MRS Fall Meeting, Graduate Student Award Talk*, Boston, USA, 2006

Publications

1. Fleischhaker, F.; Zentel, R. "Photonic Crystals from Core-Shell Colloids with Incorporated Highly Fluorescent Quantum Dots" *Chem. Mater.* **17**, 1346 (2005)
2. Fleischhaker, F.; Arsenault, A. C.; Kitaev, V.; Peiris, F. C.; v. Freymann, G., Manners, I.; Zentel, R.; Ozin, G. A. "Photochemically and Thermally Tunable Planar Defects in Colloidal Photonic Crystal". *J. Am. Chem. Soc.* **127**, 9318 (2005)
3. Fleischhaker, F.; Arsenault, A. C.; Wang, Z.; Kitaev, V.; Peiris, F. C.; v. Freymann, G., Manners, I.; Zentel, R.; Ozin, G. A. "Redox Tunable Defects in Colloidal Photonic Crystals" *Adv. Mater.* **17**, 2455 (2005), **front cover, featured by "Materials Today"**
4. Fleischhaker, F.; Arsenault, A. C.; Tetreault, N.; Wang, Z.; Kitaev, V.; Peiris, F. C.; Mihi, A.; Miguez, H.; v. Freymann, G.; Manners, I.; Zentel, R.; Ozin, G. A. "Smart Defects in Colloidal Photonic Crystals" *Mater. Res. Soc. Symp. Proc.*, 901E (2005)
5. Allard, D.; Lange, B; Fleischhaker, F.; Zentel, R.; Wulf, M. "Opaline effect pigments by spray induced self-assembly on porous substrates" *Soft Mater.* **3**, 121 (2005)
6. Fleischhaker, F.; Arsenault, A. C.; Tetreault, N.; Wang, Z.; Kitaev, V.; Peiris, F. C.; Mihi, A.; Miguez, H.; v. Freymann, G.; Manners, I.; Zentel, R.; Ozin, G. A. "Tunable Defects in Colloidal Photonic Crystals" *Proceedings of the SPIE-The International Society for Optical Engineering*, 6182, 61820L (2006)
7. Fleischhaker, F.; Arsenault, A. C.; Kitaev, V.; Peiris, F. C.; Manners, I.; Zentel, R.; Ozin, G. A. "DNA Designer Defects in Photonic Crystals: Optically Monitored Biochemistry" *Adv. Mater.* **18**, 2387 (2006)
8. Fleischhaker, F.; Arsenault, A. C.; Wang, Z.; Kitaev, V.; Peiris, F. C.; v. Freymann, G., Manners, I.; Zentel, R.; Ozin, G. A. "Colloidal Photonic Crystals with Designed Functional Polyelectrolyte Multilayer Defects" *Polymer Preprints (ACS)*, **47**, 370 (2006)
9. Fleischhaker, F.; Zentel, R. "Opale – von edlen Schmucksteinen zum Wellenleiter und Biosensor" *Chemie in unserer Zeit* **41**, 32 (2006), (invited paper)
10. Arsenault, A.; Fleischhaker, F.; v. Freymann, G.; Kitaev, V.; Miguez, H.; Mihi, A.; Tetreault, N.; Vekris, E.; Manners, I.; Aitchison, S.; Perovic D.; Ozin, G. A. "Perfecting Imperfection – Designer Defects in Colloidal Photonic Crystals" *Adv. Mater.* **18**, 2779 (2006), (research news)
11. Fleischhaker, F.; Arsenault, A. C.; Schmidtke, J.; Ozin, G. A ; Zentel, R. "Spin-Coating of Designed Functional Planar Defects in Opal Film – Generalized Synthesis", *Chem. Mater.* **18**, 5640 (2006)

12. Lange, B.; Fleischhaker, F.; Zentel, R. "Chemical Approach to Functional Artificial Opals" *Macromol. Rapid Comm.* (2007), accepted, (review article)

Patent

Fleischhaker, F.; Arsenault, A. C.; Ozin, G. A., "Photonic Crystal Sensor with Active Defect", filed, 2006